

THE UNIVERSITY OF NOTTINGHAM
SIR PETER MANSFIELD IMAGING CENTRE
SCHOOL OF PHYSICS AND ASTRONOMY

Developing Techniques for Quantitative Renal Magnetic Resonance Imaging

Author:
Alexander James DANIEL MSci

Supervisor:
Prof. Susan FRANCIS

12th January, 2021



Thesis submitted to the University of Nottingham for the degree of Doctor of Philosophy

Abstract

Science will happen, but this bit can be read by muggles on ‘tinterweb.

Contents

Abstract	i
Acknowledgments	vi
Abbreviations	vii
Introduction	1
Clinical Motivation	1
Thesis Overview	1
References	3
1 Principles of Nuclear Magnetic Resonance Imaging	4
1.1 Source of the NMR Signal	5
1.1.1 Nuclear Spin	5
1.1.2 Application of an External Magnetic Field	6
1.1.3 Precession	7
1.1.4 Resonance	7
1.2 Relaxation and Contrast Mechanisms	9
1.2.1 Longitudinal Relaxation (T_1)	9
1.2.2 Transverse Relaxation (T_2 and T_2^*)	10
1.2.3 Diffusion Imaging	14
1.2.4 Optimisation of Tissue Contrast	15
1.3 Forming an Image	16
1.3.1 Signal Localisation	16
1.3.2 Image Acquisition Acceleration	22
1.3.3 Image Acquisition Schemes	24
1.4 Conclusion	29
1.5 References	30

2 Assessment of Renal T_2 Mapping Methods	31
2.1 Introduction	32
2.1.1 Theory	32
2.2 Methods	32
2.2.1 Acquisition Schemes	32
2.2.2 Post Processing	36
2.3 Results	38
2.3.1 Sequence Accuracy	38
2.3.2 Image Quality	42
2.3.3 In-Vivo	42
2.4 Discussion	46
2.5 Conclusion	46
2.6 Acknowledgements	46
2.7 References	47
3 Applying T_2 Relaxation Under Spin Tagging (TRUST) To Assess Renal Oxygenation	48
3.1 Introduction	49
3.2 Methods	52
3.2.1 Susceptibility-Based Oximetry	52
3.2.2 T_2 Relaxation Under Spin Tagging	53
3.2.3 Inducing Changes in Oxygenation of Blood in the Renal Vein	59
3.3 Results and Discussion	61
3.3.1 Susceptibility-Based Oximetry	61
3.3.2 T_2 Relaxation Under Spin Tagging	62
3.4 Conclusions and Future Work	70
3.5 Acknowledgements	70
3.6 References	71
4 Automated Segmentation of Kidneys using Machine Learning	76
4.1 Introduction	77
4.2 Methods	79
4.2.1 Data Acquisition	79
4.2.2 Data Pre-Processing	79
4.2.3 Network Architecture	80

4.3	Results and Discussion	82
4.4	Conclusions and Future Work	88
4.5	Acknowledgements	89
4.6	References	90
5	Ex-Vivo Renal MRI	92
5.1	Introduction	93
5.2	Methods	95
5.2.1	Sample Acquisition and Fixation	95
5.2.2	T_1 Mapping	95
5.2.3	T_2 Mapping	97
5.2.4	T_2^* Mapping	97
5.2.5	Apparent Diffusion Coefficient	98
5.2.6	Diffusion Tensor Imaging	98
5.2.7	Layer Based Analysis	100
5.3	Results and Discussion	103
5.3.1	Fixation and Protocol Development	103
5.3.2	Monitoring Changes in MR Parameters Post Fixation	105
5.3.3	Comparing MR and Histological Measures in Aged Kidneys	110
5.4	Conclusions and Future Work	111
5.4.1	Protocol Validation on a Single Sample	112
5.4.2	Ex-Vivo Sample Coil	112
5.4.3	Human Organs	112
5.5	Acknowledgements	113
5.6	References	114
6	Conclusion	117

Todo list

- | | | |
|---|--|---|
| █ | Add a little bit about renal anatomy, CKD and maybe transplants. | 1 |
| | Make sure these are in the correct order | 1 |

Acknowledgements

Finally thank you to covid-19 for removing enough distractions to motivate me to write this thesis.

Abbreviations

ADC Apparent Diffusion Coefficient

AKI Acute Kidney Injury

AM Additive Manufacturing

ASL Arterial Spin Labelling

BOLD Blood Oxygen Level Dependent

CBF Cerebral Blood Flow

CFD Computational Fluid Dynamics

CKD Chronic Kidney Disease

CMRO₂ Cerebral Metabolic Rate of Oxygen

CNN Convolutional Neural Network

CPMG Carr-Purcell-Meiboom-Gill

DTI Diffusion Tensor Imaging

DWI Diffusion Weighted Imaging

EPI Echo Planar Imaging

eTE Effective Echo Time

ETL Echo Train Length

FA Flip Angle

FAIR Flow-sensitive Alternating Inversion Recovery

FFE Fast Field Echo

FID Free Induction Decay

FOV Field Of View

FSE Fast Spin Echo

FSL fMRI Software Library

GE Gradient Echo

GFR Glomerular Filtration Rate

GPU Graphical Processing Unit

GraSE Gradient Spin Echo

GUI Graphical User Interface

H and E Haematoxylin and Eosin

HASTE Half-Fourier Single-shot Turbo spin Echo

ISMRM International Society of Magnetic Resonance in Medicine

LSTM Long Short-Term Memory

ME-TSE Multi-Echo Turbo Spin Echo

MRI Magnetic Resonance Imaging

NBF Neutral Buffered Formalin

NIST National Institute of Standards and Technology

NMR Nuclear Magnetic Resonance

PBS Phosphate-buffered Saline

PC Phase Contrast

PLD Post Label Delay

PSD Pulse Sequence Diagram

PSF Point Spread Function

PRELUDE Phase Region Expanding Labeller for Unwrapping Discrete Estimates

RARE Rapid Acquisition with Relaxation Enhancement

RBF Renal Blood Flow

RNN Recursive Neural Network

ReLU Rectified Linear Unit

RF Radio Frequency

RMRO₂ Renal Metabolic Rate of Oxygen

ROI Region Of Interest

SAR Specific Absorption Rate

SBO Susceptibility Based Oximetry

SE Spin Echo

SENSE Sensitivity Encoding

SNR Signal to Noise Ratio

SPMIC Sir Peter Mansfield Imaging Centre

TE Echo Time

TFE Turbo Field Echo

TFEPI Turbo Field Echo Planar Imaging

TI Inversion Time

TILT Transfer Insensitive Labelling Technique

TKV Total Kidney Volume

TLCO Twelve Layer Concentric Objects

TR Repetition Time

True-FISP True Fast Imaging with Steady Precession

TRUST T_2 Relaxation Under Spin Tagging

TSE Turbo Spin Echo

UKKW United Kingdom Kidney Week

vNavs Volume Navigators

WET Water suppression Enhanced through T_1 effects

Introduction

Science will happen

What MRI is and why we want to use it in the body? Whats quantitative MRI?

Clinical Motivation

Kidneys, wot do?

Thesis Overview

Chapter 1 provides the theoretical framework of Nuclear Magnetic Resonance (NMR) and Magnetic Resonance Imaging (MRI). A detailed description if given of the origin of the measured signal, processes that give rise to contrast between tissues and the methods of image formation.

Chapter 2 explores T_2 mapping within the kidneys. There is little consensus as to which method should be used within the kidneys [1], thus leading to inconsistent values quoted between studies [2]. Here multiple methods from the literature are compared assessing their quantitative accuracy, sensitivity to flow and image quality in phantoms before five subjects are scanned to assess the methods in-vivo.

Chapter 3 aims to translate methods for measuring blood oxygenation from vessels in the brain to use within the kidneys. Focusing on Susceptibility Based Oximetry (SBO) [3] and T_2 Relaxation Under Spin Tagging (TRUST) [4] this chapter optimises the methods for use in the abdomen, verifying the modifications in the brain, then carries out an oxygen challenge in-vivo to measure changes in oxygen saturation within the renal vein.

Add a
little bit
about
renal
ana-
tomy,
CKD
and
maybe
trans-
plants.

Make
sure
these are
in the
correct
order

Chapter 4 describes the development of a fully automated method to segment the kidneys from MRI data. Defining renal masks is an important, yet time consuming, aspect of many studies. The masks can be used to calculate Total Kidney Volume (TKV) or to inform downstream processing. Here a Convolutional Neural Network (CNN) is developed to segment the kidneys from T_2 weighted Half-Fourier Single-shot Turbo spin Echo (HASTE) images. Software is developed to provide an executable that allows anyone to segment the kidneys in a few seconds on regular office hardware.

Chapter 5 develops methods for scanning kidneys ex-vivo. The clinical gold standard for diagnosis of renal pathologies is biopsy followed by histological analysis. Comparison between this gold standard and recently developed quantitative MRI techniques is vital for clinical translation. Here a pipeline for multi-parametric imaging of the same kidney in-vivo, ex-vivo followed by histology is developed.

Chapter 6 concludes the thesis, highlighting key results and their current applications. It also provides an overview as to future research directions and how the methods developed could be applied to new paradigms or expanded upon.

References

1. Dekkers, I. A. *et al.* Consensus-Based Technical Recommendations for Clinical Translation of Renal T1 and T2 Mapping MRI. *Magnetic Resonance Materials in Physics, Biology and Medicine*. ISSN: 1352-8661 (22nd Nov. 2019).
2. Wolf, M. *et al.* Magnetic Resonance Imaging T1- and T2-Mapping to Assess Renal Structure and Function: A Systematic Review and Statement Paper. *Nephrology Dialysis Transplantation* **33**, ii41–ii50. ISSN: 0931-0509 (suppl_2 1st Sept. 2018).
3. Jain, V., Langham, M. C. & Wehrli, F. W. MRI Estimation of Global Brain Oxygen Consumption Rate. *Journal of Cerebral Blood Flow & Metabolism* **30**, 1598–1607. ISSN: 0271-678X (1st Sept. 2010).
4. Lu, H. & Ge, Y. Quantitative Evaluation of Oxygenation in Venous Vessels Using T2-Relaxation-Under-Spin-Tagging MRI. *Magnetic Resonance in Medicine* **60**, 357–363. ISSN: 1522-2594 (1st Aug. 2008).

Chapter 1

Principles of Nuclear Magnetic Resonance Imaging

Abstract

This chapter outlines the theoretical framework behind Nuclear Magnetic Resonance (NMR) and Magnetic Resonance Imaging (MRI). Beginning with an overview of nuclear spin and resonance the origin of the signal measured in Nuclear Magnetic Resonance (NMR) is explained. The processes responsible for variations within signals such as relaxation mechanisms is then outlined in addition to techniques used to measure these different signals. Finally an overview of the process by which the signals can be used to form images is given. Covering concepts such as spacial localisation, image acquisition schemes and acceleration methods.

1.1 Source of the NMR Signal

1.1.1 Nuclear Spin

The NMR signal arises from the interaction between the atomic nucleus and an external magnetic field. These atomic nuclei possess intrinsic properties, mass (m), charge (q) and spin (I). Spin is a quantum mechanical property and as such, can only take values of half integers or integers. Nuclear spin is dictated by the sum of the constituent particles of the nucleus, protons and neutrons, each of which possesses their own spin of either $1/2$ or $-1/2$. The additive nature of nuclear spin means that pairs of nucleons can cancel out leaving the nucleus with zero net spin, this happens when the nucleus contains an even number of protons and neutrons. If the nucleus contains an odd number of both protons and neutrons, it will have a positive integer nuclear spin whereas if the nucleus has an odd number of protons or neutrons, it will have a half integer spin.

The spin angular momentum, \mathbf{J} of a nucleus of spin I is given by

$$|\mathbf{J}| = \hbar\sqrt{I(I+1)} \quad (1.1)$$

where \hbar is the reduced Plank's constant, $h/2\pi$. As the nucleus is charged and rotating, it gives rise to a current and therefore a magnetic moment μ ,

$$\mu = \gamma\mathbf{J} \quad (1.2)$$

where γ is the gyromagnetic ratio for the nucleus, a constant which depends on the charge and mass of the nucleus. Table 1.1 shows the gyromagnetic ratio (γ) and nuclear spin (I) of common NMR sensitive isotopes [1–3]. Due to its relatively high gyromagnetic ratio, compared to other nuclei used for NMR, and relative abundance in the body, ^1H , a single proton, is most commonly used for Magnetic Resonance Imaging (MRI).

Isotope	Spin	γ (MHzT $^{-1}$)	Sensitivity Relative to ^1H
^1H	$1/2$	42.58	1
^2H	1	6.54	0.0097
^{13}C	$1/2$	10.71	0.016
^{19}F	$1/2$	40.05	0.83
^{23}Na	$3/2$	11.27	0.093
^{31}P	$1/2$	17.25	0.066

Table 1.1: Common NMR isotopes, their nuclear spin, gyromagnetic ratio and sensitivity, relative to ^1H .

1.1.2 Application of an External Magnetic Field

If we consider the hydrogen nuclei in a sample of tissue, the number of possible eigenstates for a nucleus of nuclear spin I is $(2I + 1)$. This means that for the ${}^1\text{H}$ nuclei in our sample, where $I = 1/2$, we can observe two possible eigenstates, $|+1/2\rangle$ and $|{-1/2}\rangle$ often written as $|\uparrow\rangle$ and $|\downarrow\rangle$. In the absence of an external magnetic field, these states are degenerate as they have the same energy, however, if we move our sample into a static external magnetic field along the z -axis, B_0 , the energy levels separate.

The z -component of the magnetic moment is defined by,

$$\mu_z = \gamma\hbar\mu_I \quad (1.3)$$

where m_I are the possible spin quantum numbers of the nucleus. For our proton system with spin $1/2$, μ_z is given by

$$\mu_z = \pm \frac{1}{2}\gamma\hbar. \quad (1.4)$$

The spins can either be aligned parallel to the external magnetic field in the lower energy of the two eigenstates, also known as spin up, or anti-parallel to the magnetic field in the higher energy eigenstate, spin down. The energy difference between these two eigenstates is given by,

$$\Delta E = \gamma\hbar B_0. \quad (1.5)$$

For an ensemble of spins in an external magnetic field, there will be an imbalance between the populations of each state with more spins occupying the lower of the two energy states. The net magnetisation of the sample is simply the sum of the constituent spins and as such, the application of an external magnetic field leads to the sample gaining a net magnetisation vector aligned with B_0 . This effect is very small, the magnitude of the imbalance between eigenstates can be derived from Boltzmann statistics and is given by,

$$\frac{N_\uparrow}{N_\downarrow} = \exp\left(\frac{\Delta E}{k_B T}\right), \quad (1.6)$$

where N_\downarrow and N_\uparrow are the the number of spins aligned with and against B_0 respectively, k_B is Boltzmann's constant and T is the temperature of the system. This means that for a sample of biological tissue at body temperature in a 3T magnetic field, the population difference is very small at approximately three parts per million. Although this measurable proportion is very small, it can be detected due to the high density of protons in the tissue. The signal can also be increased by the application of a stronger B_0 .

1.1.3 Precession

Classically, if a magnetic moment, M , is placed into an external magnetic field, B , it will experience a torque, τ , proportional to change in angular momentum and thus induce a rotation.

$$\mathbf{M} \times \mathbf{B} = \frac{d\mathbf{J}}{dt} = \boldsymbol{\tau} \quad (1.7)$$

From (1.2) the quantum equivalent of (1.7) is the standard form of the Bloch equation[4],

$$\frac{d\mu}{dt} = \gamma \mu \times \mathbf{B} \quad (1.8)$$

This equation states that if the magnetic moment, μ is not aligned with the external magnetic field, \mathbf{B} , it will precess about \mathbf{B} . The frequency of this precession, ω_0 is known as the Larmor frequency and is given by substituting Bohr's frequency condition of the Planck relation ($\Delta E = \hbar\omega$) into (1.5),

$$\omega_0 = \gamma B_0, \quad (1.9)$$

Nuclei with a positive gyromagnetic ratio precess clockwise, whereas nuclei (and the electron) with a negative gyromagnetic ratio precess anti-clockwise. For a proton in a 3T magnetic field, the Larmor frequency is 128 MHz.

1.1.4 Resonance

Resonance is the process of energy transfer into a system by the application of energy at the natural frequency of the system. In the case of NMR this is the application of an Radio Frequency (RF) pulse near the Larmor frequency. Before the RF pulse is applied, the spins are at equilibrium, aligned with B_0 . Upon the application of a B_1 field close to the Larmor frequency of the target nucleus and perpendicular to B_0 , the spins aligned with B_0 will be displaced from equilibrium and thus precession is induced. The longer the B_1 field is applied, the more the net magnetisation vector is displaced, or tipped, away from B_0 , this allows arbitrary flip angles, α , to be achieved, (1.10).

$$\alpha = \int_0^T \gamma B_1(t) dt \quad (1.10)$$

In addition to displacing the spins, the B_1 field also induces phase coherence within the ensemble making up the net magnetisation vector. When considering the effects of RF pulses, it can often be simpler to imagine the system from a reference frame rotating about the z-axis at the Larmor frequency. This has the effect of making B_1 stationary along the

1.1. Source of the NMR Signal

x-axis. Figure 1.1 shows the evolution of a spin in both the laboratory and rotating frame after the application of a 90° RF pulse. In both figures the spin is tipped into the transverse plane, M_{xy} .

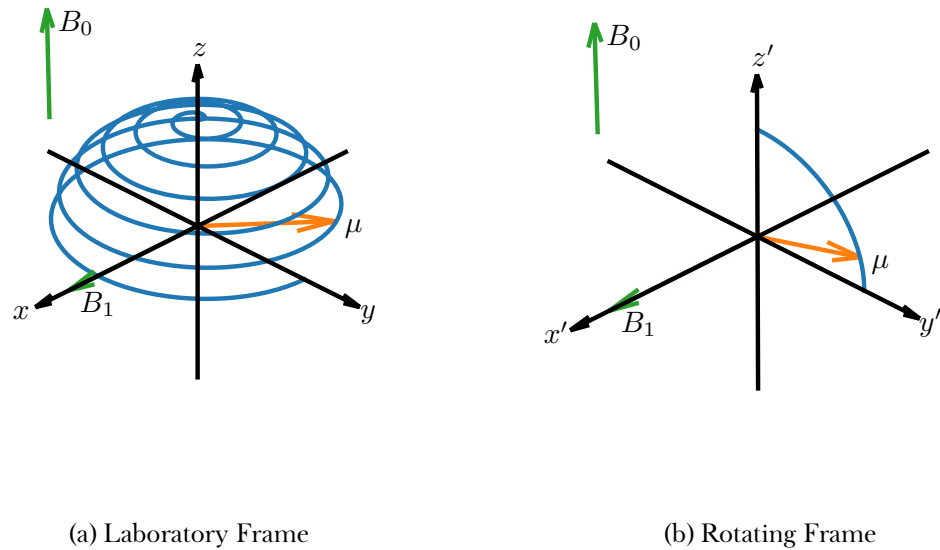


Figure 1.1: The laboratory frame of reference shows the procession of the spin about B_0 while in the rotating frame, the spin simply rotates about the x' -axis

1.2 Relaxation and Contrast Mechanisms

If disturbed from equilibrium by an RF pulse, the net magnetisation vector will not remain in this new state ad infinitum, instead, once the RF pulse has finished, it will transition back to its equilibrium state in a process known as relaxation. The time constants characterising the relaxation process vary depending on the environment the spins are in and as such, can vary between different biological tissues. These relaxation constants are the principle source of contrast in MRI. Mathematically, this relaxation is described by the full form of the Bloch equation, (1.11).

$$\frac{d\mathbf{M}}{dt} = \gamma(\mathbf{M} \times \mathbf{B}) - \frac{(M_z - M_0)}{T_1}\hat{\mathbf{z}} - \frac{M_x\hat{\mathbf{x}} + M_y\hat{\mathbf{y}}}{T_2} \quad (1.11)$$

1.2.1 Longitudinal Relaxation (T_1)

Upon excitation, energy is exchanged between the spin system and the surrounding environment. The result of this energy exchange is that the energy of the spin system decreases and the longitudinal magnetisation exponentially decays to its equilibrium position. The time constant of this exponential decay returning to equilibrium, M_0 is known as the longitudinal relaxation time or T_1 and is dictated by the efficiency of energy transfer between the spin system and the surrounding lattice, hence its historical name, spin-lattice relaxation.

The efficiency of this energy transfer is primarily dictated by the motion of the surrounding lattice. As nearby molecules undergo rotation and translation they cause variations in the local magnetic field. If these fluctuations are at a similar frequency to the Larmor frequency then energy transfer via dipole-dipole interactions will be relatively efficient. The rate of energy transfer can also be increased if the molecules are more closely coupled for example, tissues with a lower molecular mobility tend to have a shorter T_1 than those with a high molecular mobility.

Measuring T_1

The longitudinal component of the Bloch equation, (1.11), is given by (1.12).

$$\frac{dM_z}{dt} = -\frac{(M_z - M_0)}{T_1} \quad (1.12)$$

Solving this equation for M_z gives,

$$M_z = M_0 \left[1 - \exp\left(-\frac{t}{T_1}\right) \right] + M_z(0) \exp\left(-\frac{t}{T_1}\right) \quad (1.13)$$

The gold standard method for quantification of T_1 is the inversion recovery pulse sequence in which a 180° pulse is used to fully invert the magnetisation, such that $M_z(0) = -M_0$ and as such (1.13) reduces to,

$$M_z = M_0 \left[1 - 2 \exp\left(-\frac{t}{T_1}\right) \right]. \quad (1.14)$$

To measure T_1 , the experiment is repeated multiple times, with measurements of M_z taken at different times after the 180° inversion pulse, Inversion Time (TI). The magnetisation must have fully recovered to M_0 between each inversion pulse, as such the minimum time between inversions, Repetition Time (TR) is five times T_1 . Curve fitting can then be used to estimate M_0 and T_1 , Figure 1.2. This method is expanded upon when it is used in Chapter 5.

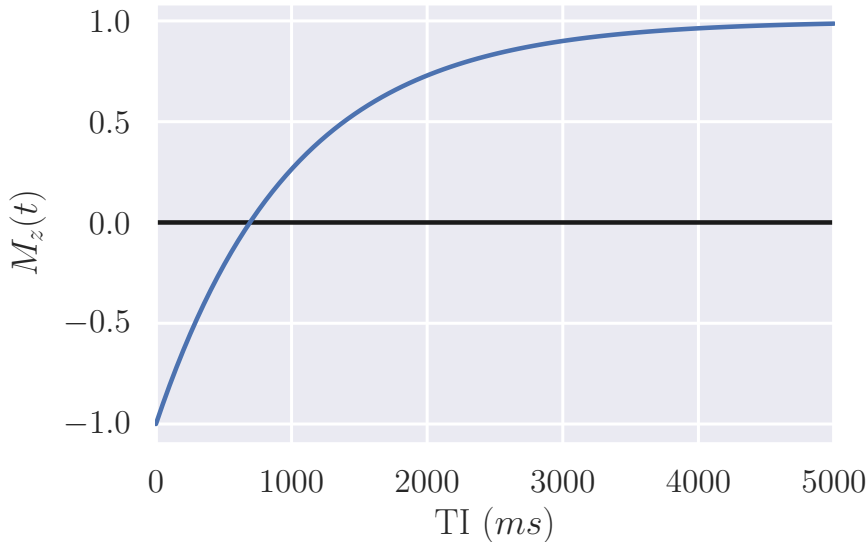


Figure 1.2: The longitudinal magnetisation for a sample of $T_1 = 1000$ ms in an inversion recovery experiment.

1.2.2 Transverse Relaxation (T_2 and T_2^*)

Upon the application of a 90° RF pulse, the net magnetisation vector has tipped in the y' direction resulting in phase coherence and creating transverse magnetisation, $M_{x'y'}$. The spins then precess about the z -axis at their Larmor frequency, dictated by the magnetic field they are in. This magnetic field is not perfectly homogenous over the whole ensemble though, random dipole-dipole interaction with neighbouring spins produce short-

lived fluctuations in the local magnetic field and thus the Larmor frequency of each spin varies. As the spins process at different frequencies, they de-phase, resulting in the transverse magnetisation decaying to zero as phase coherence is lost. This mechanism is driven by energy transfer between the spins within the system so is sometimes termed, spin-spin relaxation. The rate at which this loss of phase coherence due to spin-spin interactions occurs is characterised by the time constant T_2 .

The local magnetic field is not just influenced by spin-spin interactions. Local inhomogeneities in the static B_0 field can be caused by susceptibility differences within the sample and hardware imperfections. These B_0 inhomogeneities result in additional perturbation to the local magnetic field and therefore results in additional de-phasing of the system. The rate at which this de-phasing due to static B_0 inhomogeneities occurs is characterised by the time constant T'_2 . The measured decay in transverse magnetisation is therefore dictated by T_2^* , which is related to T_2 and T'_2 by

$$\frac{1}{T_2^*} = \frac{1}{T_2} + \frac{1}{T'_2}. \quad (1.15)$$

Measuring T_2 and T_2^*

The transverse component of the Bloch equation, (1.11), is given by (1.16).

$$\frac{dM_{xy}}{dt} = -\frac{M_{xy}}{T_2} \quad (1.16)$$

Solving the differential equation for M_{xy} with respect to t gives,

$$M_{xy}(t) = M_{xy}(0) \exp\left(-\frac{t}{T_2}\right), \quad (1.17)$$

It should be noted that (1.17) is an idealised equation and thus does not include static field inhomogeneities that contribute to T'_2 and thus the magnetisation of a real signal will decay with T_2^* .

After a 90° RF pulse the envelope of the signal will decay with T_2^* , known as an Free Induction Decay (FID). As such, by measuring the amplitude of the signal at different time points, t , the decay can be sampled and fit to estimate T_2^* .

Spin Echoes

To measure T_2 , rather than T_2^* , the effects of static B_0 inhomogeneities that lead to T_2' must be negated. Because the processes driving the de-phasing that lead to T_2' are constant over time, the refocussing effects of a Spin Echo (SE) sequence, outlined in Figure 1.3, can be utilised to reform this de-phasing component. In a SE sequence, an initial 90° excitation pulse shifts M into the transverse plane and induces phase coherence, Figure 1.4a. T_2' effects will then cause some spins to precess quickly and others more slowly and thus de-phase with T_2' , Figure 1.4b. At time, Echo Time (TE)/2, later a 180° pulse is used to flip the spin ensemble, reversing the phase shift meaning those spins that had accrued the largest positive phase shift will now have the largest negative phase shift and vice versa, Figure 1.4c. Because the B_0 inhomogeneities that lead to T_2' are static, they will still be acting to the same degree on each spin. This leads to an echo forming at $t = \text{TE}$ as those spins with the highest Larmor frequency, and largest negative phase shift, refocus or “catch up” with those spins with a lower Larmor frequency, Figure 1.4d. The processes leading to T_2 are not constant over time and as such are not refocussed by the 180° pulse, hence the echo in Figure 1.4d is not perfectly refocussed and the signal will be attenuated at a rate dictated by T_2 .

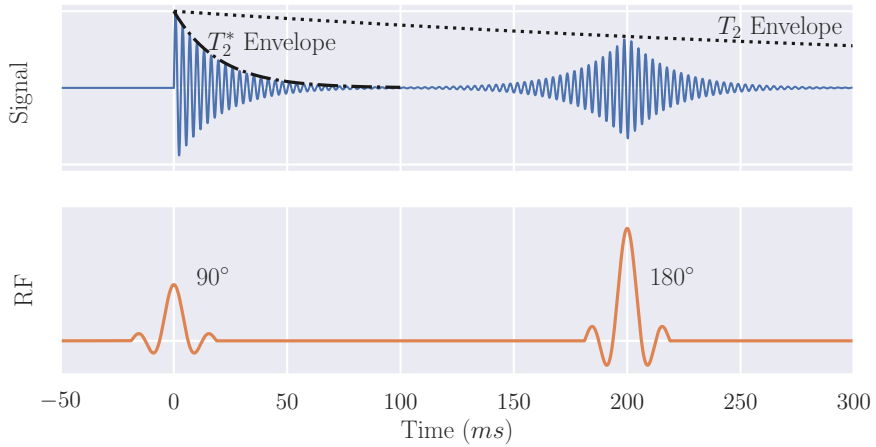


Figure 1.3: The signal produced in a spin-echo sequence used to measure T_2 .

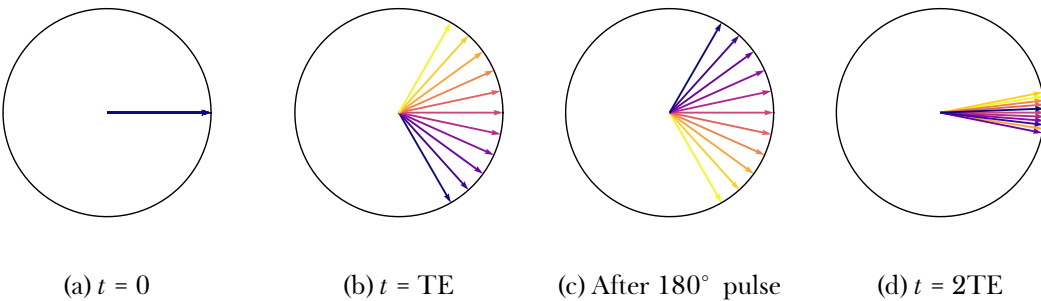


Figure 1.4: Spins evolving in a spin echo sequence showing the de-phasing, (b), refocusing pulse, (c), and subsequent refocusing, (d).

By repeating this sequence over a range of TE the T_2 curve can be samples and fit to (1.17) to estimate T_2 and M_{xy0} . The SE sequence is the most basic form of T_2 mapping, more methods are explored and compared in Chapter 2.

Gradient Echoes

Echoes can be generated via another mechanism, the Gradient Echo (GE). In addition to the homogenous B_0 field and RF fields encountered thus far, MRI scanners can produce additional fields known as gradients. These switchable fields can induce linearly varying spatially dependent magnetic fields to perturb B_0 . They are used for image formation, explained in 1.3 but can also be used to form an echo. The GE pulse sequence uses a single 90° RF excitation pulse to tip the net magnetisation vector into the transverse plane. A gradient is then applied to the sample causing areas of higher field to de-phase quickly whereas areas with a relatively lower field will de-phase slower. At time $TE/2$ the polarity of the gradient is reversed thus causing the spins to refocus and an echo to be formed at time TE . An overview of the sequence is shown in Figure 1.5.

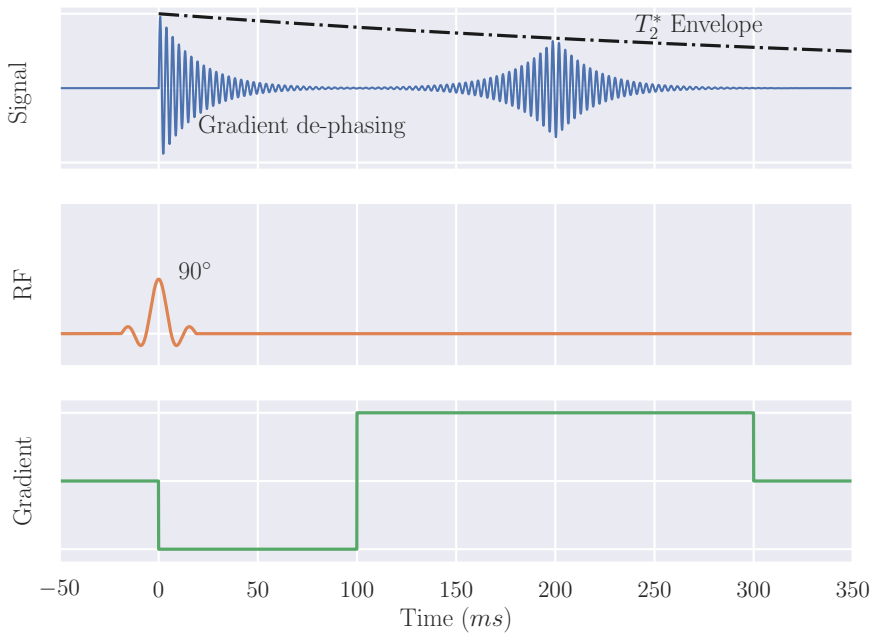


Figure 1.5: A schematic of a basic Gradient Echo (GE) sequence with TE 100 ms.

1.2.3 Diffusion Imaging

Spins have been considered stationary until now, however, in biological tissues, they are often undergoing Brownian motion leading to diffusion. The signal from a sample can be made sensitive to the degree of diffusion taking place using diffusion gradients applied between excitation and echo. If a spin undergoes a translation while the gradient is being applied, it will be in a different magnetic field and thus at a different Larmor frequency while rephasing, resulting in additional signal attenuation. The degree of signal attenuation is proportional to the rate at which diffusion is occurring i.e. how far the spin has moved while the diffusion gradient was being applied. These diffusion gradients can either be bipolar, as seen in 1.5 or monopolar if a SE sequence is used.

Not all diffusion is isotropic (occurs to the same degree in all directions), often the motion of the spins is restricted e.g. within tissue fibres. The amount of restriction is known as the fractional anisotropy where 0 represents isotropic diffusion e.g. a large vial of water, and 1 represents diffusion being constrained to a single dimension. By applying the diffusion gradients in different directions (and strengths) the preferred direction of diffusion and fractional anisotropy can be calculated. These techniques are used in Chapter 5.

1.2.4 Optimisation of Tissue Contrast

Quantitative mapping of T_1 , T_2 and T_2^* can often be a slow process due to the number of acquisitions required at different time points to sample relaxation curves. Often it is more desirable to acquire a volume at a single time with the intensity difference between tissues of interest maximised. Although the voxel intensities do not directly represent any quantitative underlying physical properties of the tissue, the contrast between tissues is sufficient for diagnosis or further analysis.

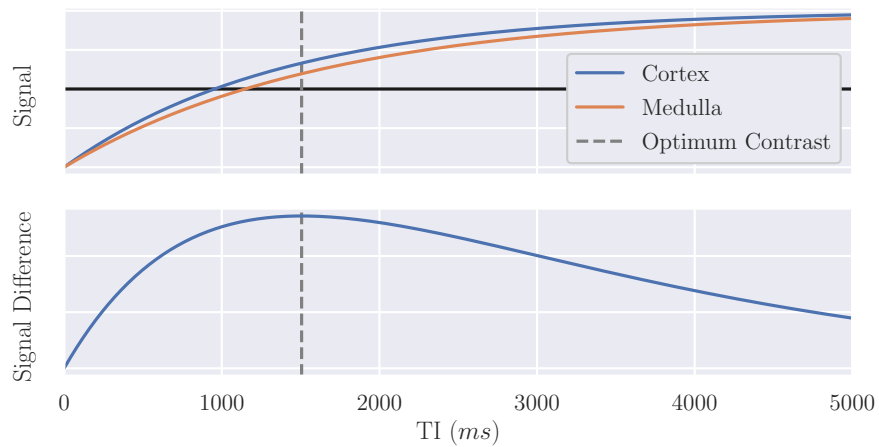


Figure 1.6: The signal generated from renal cortical and medullary tissues [5] and difference between signals. This shows that the contrast between the two tissues is optimal if the Inversion Time (TI) is 1500 ms.

1.3 Forming an Image

1.3.1 Signal Localisation

So far, NMR has been applied to measure signals from the entire sample, gaining no information about the spatial variation within it. MRI applies the techniques of NMR to spatially resolve the location of the signal.

The key concepts of MRI were developed by multiple groups in the 1970s. Lauterbur used magnetic field gradients and a back-projection reconstruction technique to generate 2D images in 1973 [6]. Simultaneously Mansfield was worked on “NMR diffraction” introducing the mathematical framework of reciprocal k -space [7] and later slice selective excitation [8]. The final key insight was provided by Ernst who published the first Fourier imaging method [9], this used non-selective excitations and linear gradients to generate 2D Fourier encoded images. These techniques are still the basis of MRI today.

The concepts of signal localisation will be introduced through the example of an axial acquisition, Figure 1.7

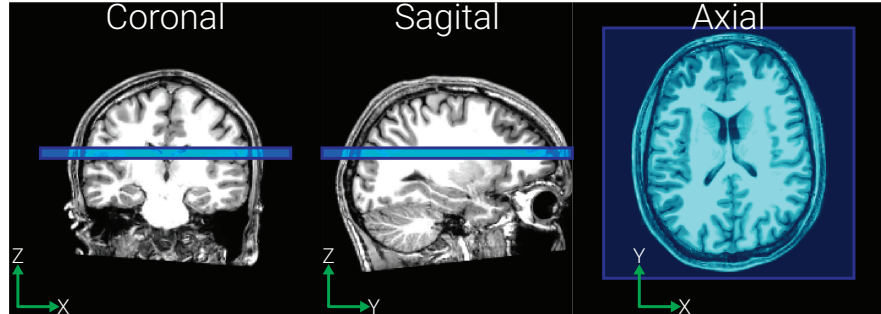


Figure 1.7: Planning used in the signal localisation example.

Gradient Fields

Signal localisation makes use of gradient fields. These produce small linear perturbations in B_0 and are applied in a combination of the x , y and z direction to enable arbitrary gradient directions and result in B_0 varying with position, \mathbf{r} ,

$$B_z(r) = (B_0 + \mathbf{G} \cdot \mathbf{r}) \hat{k}. \quad (1.18)$$

1.3. Forming an Image

As such, the resonant frequency of the spins can also be described as a function of position and, because the gradients are not static, time,

$$\omega(x, y, z, t) = \gamma(B_0 + G_x(t)x + G_y(t)y + G_z(t)z) \quad (1.19)$$

Slice Selection

The initial step in localisation is to measure the signal from a single, spatially defined, slice. If a gradient is applied along the z direction, G_z , the magnetic field experienced by the spins at position z will be

$$B(z) = B_0 + G_z z. \quad (1.20)$$

As such, from the simplification of (1.19), the Larmor frequency becomes

$$\omega(z) = \gamma(B_0 + G_z z). \quad (1.21)$$

If a frequency selective RF pulse is applied to the sample, it will only excite spins within the corresponding bandwidth and thus only a slice of desired thickness. This slice-selective thickness, Δz , can be changed by either adjusting G_z or the bandwidth of the excitation pulse, $\Delta\omega$.

$$\Delta z = \frac{\Delta\omega}{\gamma G_z} \quad (1.22)$$

The excitation profile achieved by a slice selective pulse can be approximated by a Fourier transform. Generally, a rectangular slice profile is wanted and as such, the RF pulse takes the form of a sinc function. To achieve a perfect rectangular pulse, the sinc would have to be infinite in length. Given the lack of infinite time available during an MRI examination, a truncated sinc pulse is used, generally including three or five lobes and a Gaussian filter.

The gradient applied will result in de-phasing of the spins as in a GE sequence, therefore a gradient of the opposite polarity and half the magnitude is applied after the RF pulse to re-phase the spins, Figure 1.8a.

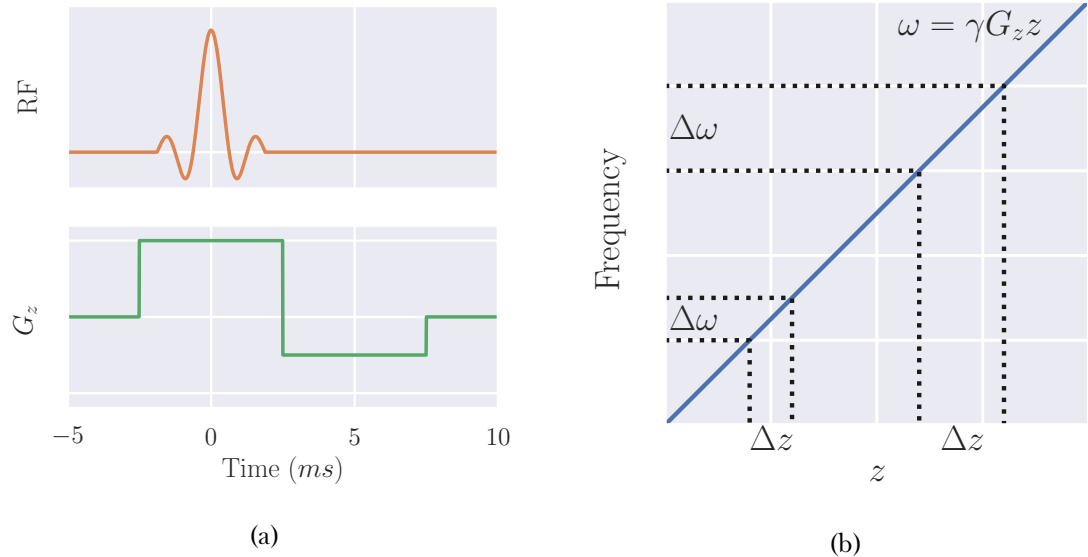


Figure 1.8: (a) A truncated sinc pulse of bandwidth $\Delta\omega$ being applied over a slice selective gradient followed by the negative re-phasing gradient lobe. Note that the area under the re-phasing gradient is half of that of the slice selective gradient. (b) Example slices of thickness Δz being excited by RF pulses of bandwidth $\Delta\omega$ showing that excitation pulses of larger bandwidth result in thicker slice profiles.

Phase Encoding

The signal has been localised from a full 3D volume to a defined 2D volumetric slice. To localise the signal in the next dimension, phase encoding is used. This technique uses a gradient in the y direction applied for time T . For the duration of G_y the spins precess with a frequency according to their position in the y direction

$$\omega(y) = \gamma(B_0 + G_y y), \quad (1.23)$$

and as such accrue a phase shift relative to if no gradient was applied, given by

$$\phi(y) = \gamma y \int_0^T G_y(t) dt. \quad (1.24)$$

Acquisitions must be repeated with different amplitudes/durations of G_y to fully sample in the y direction.

Phase aliasing occurs because the whole sample produces signal, whether it is in the Field Of View (FOV) or not. As there is a finite range of phase values (0 to 2π) tissue

1.3. Forming an Image

outside the FOV can have the same value as tissue within the FOV this results in the two signals becoming combined in a process known as wrapping. This artefact is illustrated in Figure 1.9.

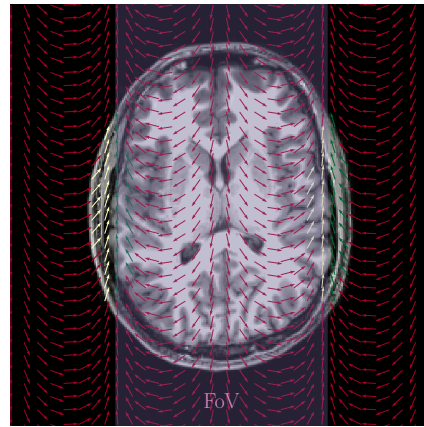


Figure 1.9: Spins outside the FOV have the same phase value as those within the FOV and thus wrapping occurs.

Frequency Encoding

Finally, the signal needs to be localised in the x direction. This is achieved using frequency encoding. Here the gradient, G_x is applied during the acquisition section of the sequence i.e. when the signal is being sampled. As the gradient is being applied during readout, those spins in the centre of the gradient (at field B_0) will be precessing at the Larmor frequency while those in a stronger field will be precessing faster. By sampling the signal generated and applying a Fourier transform to separate components of the signal at each frequency, the signal is spatially resolved in all three dimensions.

An overview of a basic signal localisation scheme is shown in Figure 1.10.

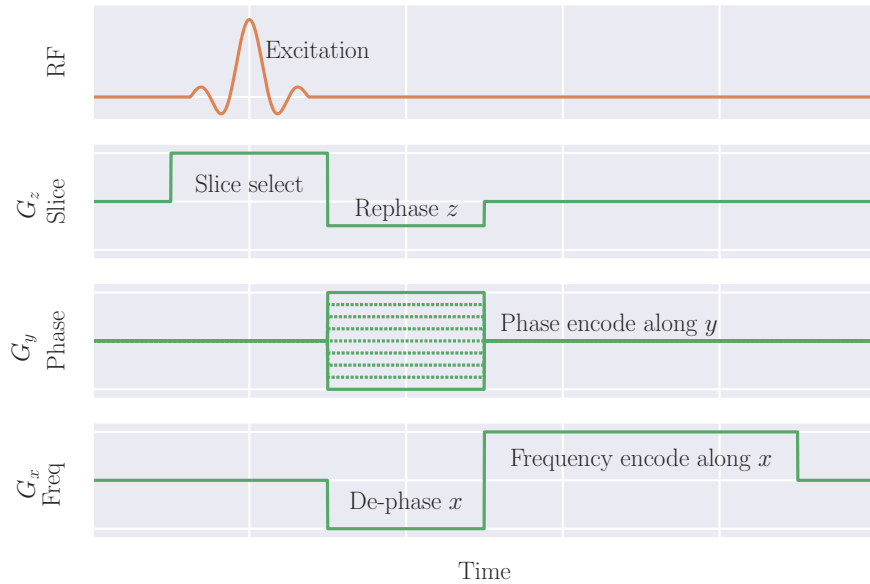


Figure 1.10

k-space

k-space, sometimes known as Fourier space, is a useful concept for interpreting MRI pulse sequences and represents the spatial frequencies of the image. Immediately after an excitation pulse and rewind gradient, the signal being sampled is at the origin of *k*-space, corresponding to low spatial frequencies, or the low resolution aspects of the image e.g. which voxels are inside or outside the body. As gradients are applied to the sample, sampling moves out from the centre of *k*-space to higher spatial frequencies corresponding to finer detail within the image. For a 2D acquisition, as above, the location in *k*-space is defined by (1.25) and (1.26) where G_x and G_y are the gradients in the frequency encode and phase encode directions respectively and t_x and t_y are the duration the gradient is applied for.

$$k_x = \gamma G_x t_x \quad (1.25)$$

$$k_y = \gamma G_y t_y \quad (1.26)$$

When recording MRI data, the continuous signal must be discretised. The higher the sampling frequency i.e. the closer together in *k*-space the samples are, Δk , the wider the FOV and the further out from the origin of *k*-space is samples, the higher resolution the image will be. Examples of *k*-space sampling patterns and their corresponding image are shown in Figure 1.11.

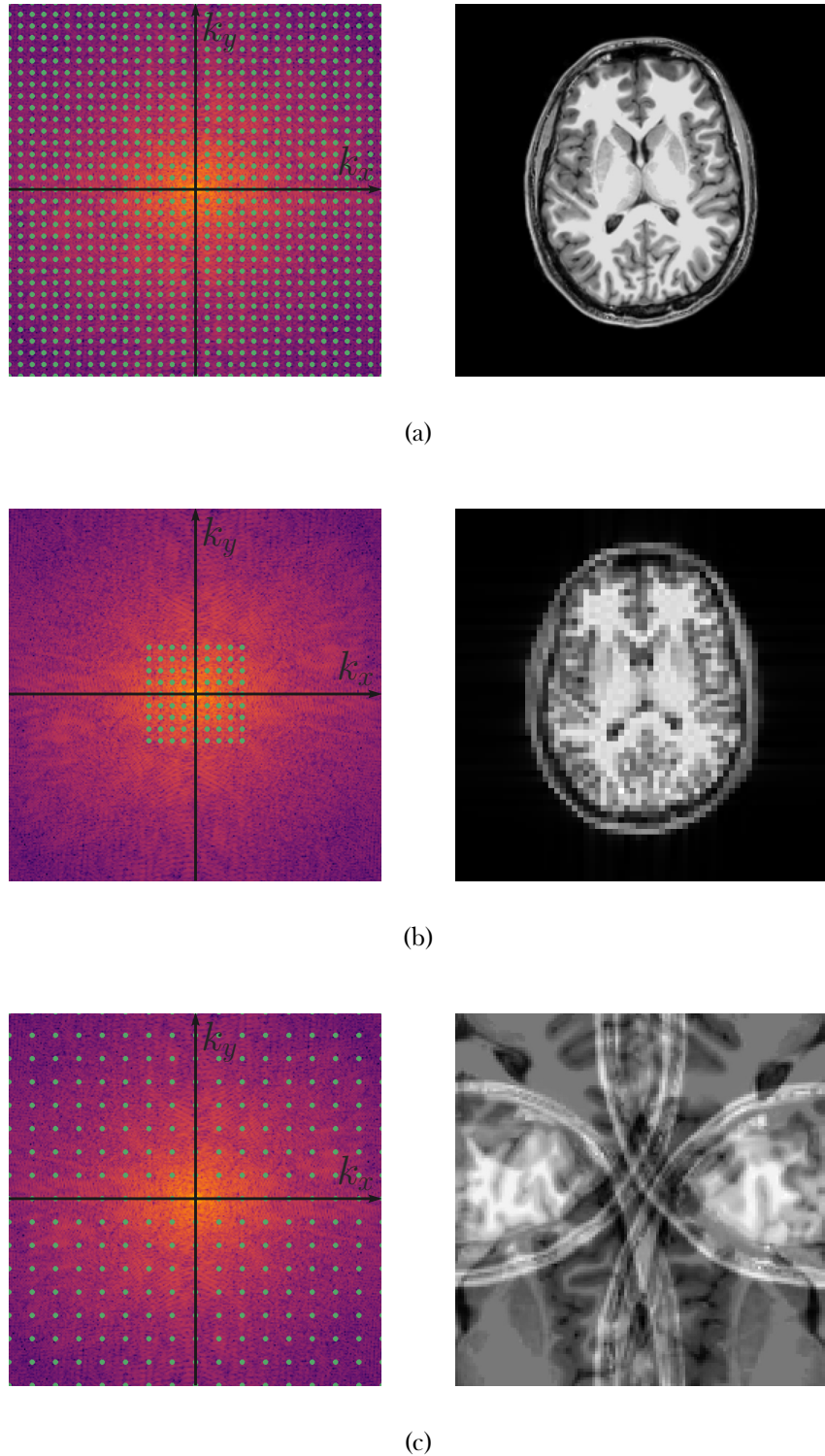


Figure 1.11: (a) Fully samples k -space and the corresponding image. (b) Centre sampling of k -space produces a lower resolution image. (c) Sampling with a larger Δk resulting in a decreased FOV and aliasing.

From k -space to Image Space

The raw data sampled in k -space can be reconstructed to an image via a Fourier transform. When the quadrature data undergoes a 2D Fourier transform, it produces a complex

1.3. Forming an Image

image composed of a real and imaginary part. These constituent parts of the image can be converted into magnitude and phase images with the magnitude representing the spin density.

Coordinate Systems

The above example was chosen so that only one gradient is used at once however if the planning of the acquisition is more complicated, the nomenclature can become more confusing, as such, for clarity multiple coordinate systems are often used.

Scanner Space This coordinate system has its origin at isocentre of the scanner and is defined in terms of x , y and z .

Imaging Space The coordinates of this system are defined by the directions used in signal localisation, M for the frequency encode direction (also called magnitude), P for the phase encode direction and S for the slice select direction.

Anatomical Space Defined in terms of the subjects orientation in the scanner, this coordinate system has the axis, Right-Left (R-L), Anterior-Posterior (A-P) and Superior-Inferior (S-I).

1.3.2 Image Acquisition Acceleration

One of the recurring limiting factors in MRI is the acquisition time. For neuroimaging applications the relatively slow acquisition of MRI limits subject throughput or the number of different measures that can be performed. In abdominal imaging, acquisition times can be even more of a hindrance given many scans are performed while the subject is holding their breath on expiration. As such, image acquisition acceleration techniques have been developed. These techniques sacrifice a small amount of Signal to Noise Ratio (SNR) for a decrease in acquisition time.

Partial Fourier

Fully sampled k -space contains inherent redundancy as it contains its own complex conjugate; the real components of the signal are symmetric while the imaginary components are anti-symmetric. This means that no contrast information is lost if a reduced area of k -space is sampled e.g. only sample 66% of k -space. This technique does impact phase information though so should not be used in acquisitions where downstream processing

1.3. Forming an Image

requires accurate phase. Known as partial Fourier or half-scan, this technique results in a decreased SNR and can introduce image artefacts as the partial Fourier factor approaches 50%, however, the acquisition time reduces by approximately the percentage of k -space sampled e.g. an acquisition that would take three minutes fully sampled will take two minutes if a partial Fourier factor of 66% is used. An example of reconstructions of full, 75% and 51% of k -space are shown in Figure 1.12

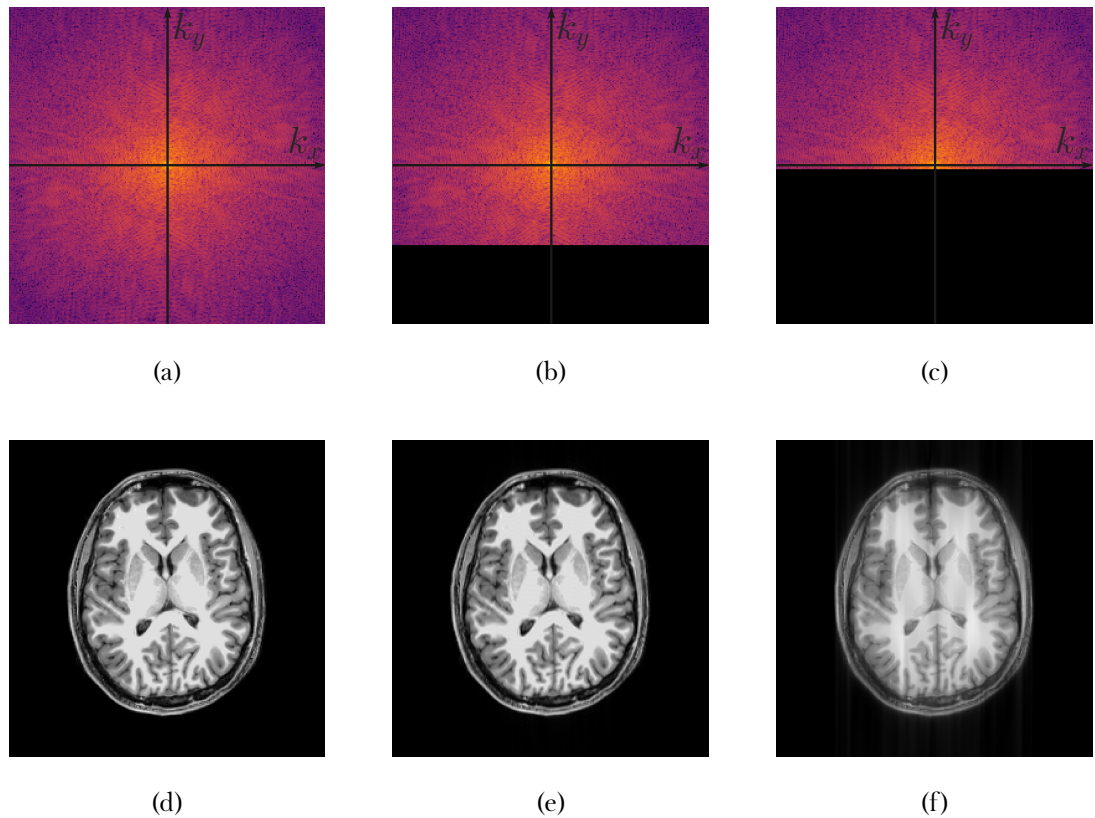


Figure 1.12: Full, (a), 75%, (b), and 51%, (c), k -space sampling and their corresponding reconstructions in image space, (d), (e) and (f) respectively.

Sensitivity Encoding (SENSE)

Most modern scanners use different coils for RF transmission, and signal receiving. The transmission coil is usually built into the bore of the magnet while the receive coil is placed as close to the source of the signal as possible. These receive coils are usually composed of multiple smaller coils to make an array, each with its own signal sampling hardware. This means that it is possible to record signal from multiple coils simultaneously with different coils supplying data for each line of k -space e.g if the array has two coils, one coil will record the odd lines of k -space and the other, the even lines, thus resulting in an increase in acquisition speed [10]. However, this parallel sampling technique reduces the lines of

1.3. Forming an Image

k -space sampled per coil and results in wrapping as seen in Figure 1.11c, albeit only in the phase direction. To combat this, the spatial sensitivity profile of each element within the array i.e. the area it can measure signal from, is measured. Using this prior knowledge of signal locations, each coil elements data can be unwrapped before all elements data being combined into a single volume.

The Sensitivity Encoding (SENSE) factor is the degree to which k -space is undersampled and is limited to the number of elements in the receive array. Applying higher SENSE factors increases acquisition speeds, however, reduces SNR.

1.3.3 Image Acquisition Schemes

Many different acquisition schemes have been developed for sampling k -space. Outlined below are some of the key sequences.

Spin Warp Imaging

The simplest uniformly sampled k -space trajectory is spin warp imaging. This technique is based on the GE scheme and samples one line of k -space per excitation, or shot, a schematic is shown in Figure 1.13. Each shot applies a different phase encode gradient to move a different amount in the k_y direction. The signal is then sampled while a gradient is applied in the frequency direction, also known as the readout gradient. The acquisition time for this sequence is very long because it only collects one line of k -space per shot and as such this technique is sensitive to subject motion.

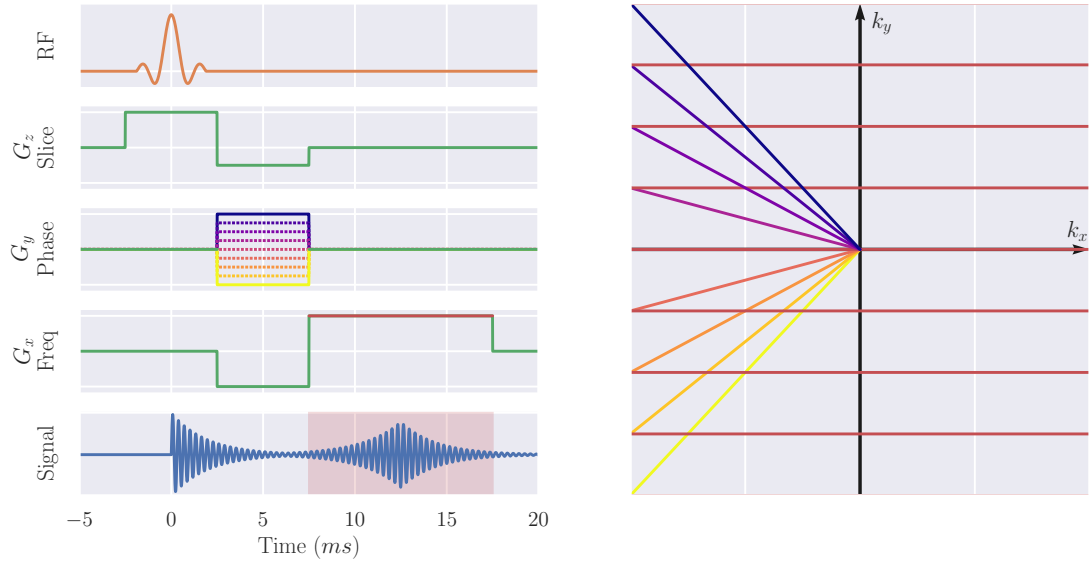


Figure 1.13: A schematic of the spin warp image sequence. The Pulse Sequence Diagram (PSD) shows the different phase encoding gradients, G_y , in colours from yellow to purple and the readout gradient, G_x , in red. These colours correlate with the colours in the k -space trajectory. The signal recorded is highlighted in red.

Echo Planar Imaging (EPI)

A much faster technique than spin warp imaging is Echo Planar Imaging (EPI) [7]. This technique samples all lines of k -space in a single excitation shot with an acquisition time typically less than 100 ms. The Pulse Sequence Diagram (PSD) and k -space trajectory for this sequence are shown in Figure 1.14. The sequence begins very similarly to the spin warp sequence with a slice selective excitation and an acquisition of the bottom line of k -space, however, instead of a spoiler followed by another excitation as in spin warp imaging, in EPI a small positive phase encode gradient ‘blip’ is applied to move up a line in k -space, followed by an inversion of the readout gradient polarity. This blip followed by reversed readout is repeated, zig-zagging up k -space until the desired k -space is sampled.

1.3. Forming an Image

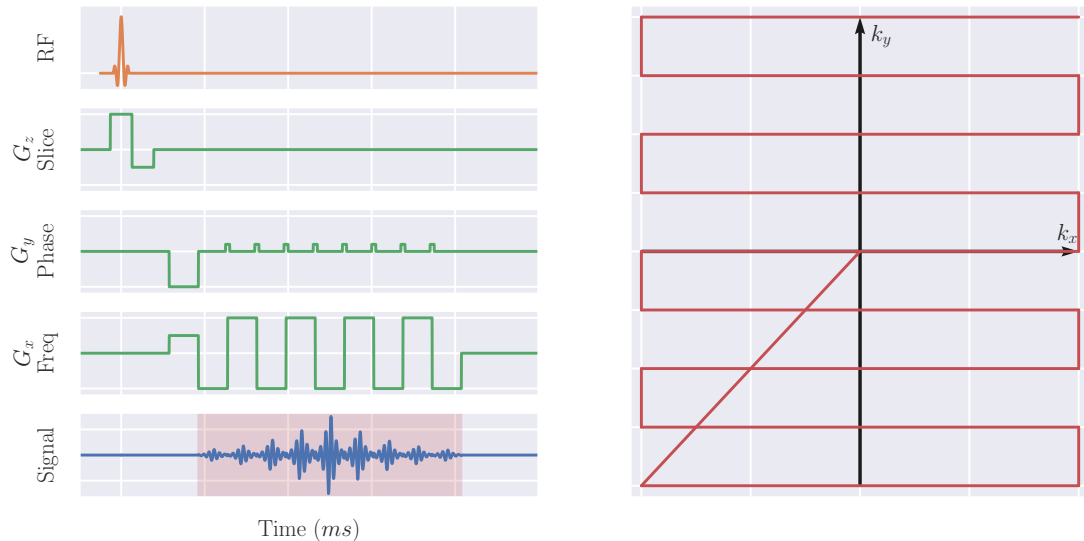


Figure 1.14: A schematic of the EPI pulse sequence and k -space trajectory. Note this diagram is not to scale.

While this sequence has a very quick acquisition time, it does have drawbacks. The long train of echoes makes EPI more sensitive to inhomogeneities in the B_0 field caused by different tissue susceptibilities or poor shimming. Eddy currents and imperfections in gradient coils cause small differences in lines collected in the positive and negative direction, leading to a Nyquist ghost artefact. Eddy currents induced by the phase encode blips also cause geometric distortions in the image, Figure 1.15, however, these can be corrected via post processing if an image with phase encode blips of opposite polarity is collected i.e. collect images sampling k -space from both bottom to top and top to bottom.

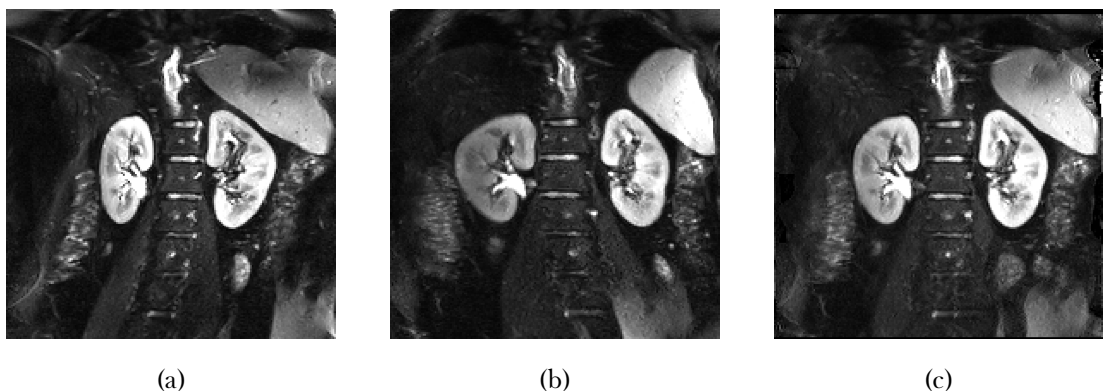


Figure 1.15: Geometric distortions in EPI when phase encode blips are (a) positive, (b) negative and (c) corrected via post processing.

Turbo Spin Echo (TSE)

The Turbo Spin Echo (TSE) sequence, also known as Fast Spin Echo (FSE) or Rapid Acquisition with Relaxation Enhancement (RARE), is an expansion on the conventional SE sequence applying evenly spaced 180° RF refocusing pulses to generate multiple echo from a single excitation, these echoes are used to record multiple lines of k -space. The number of echoes is known as the Echo Train Length (ETL), or ‘turbo factor’ and is the factor by which the scan time is reduced compared to a conventional spin echo sequence and is usually between 2 and 30 per TR; the time between echoes is known as the echo spacing and is typically 15 - 25 ms.

Each line of k -space is acquired at a different time after excitation, as such, they will have different T_2 weightings, it is therefore important to ensure the centre of k -space is acquired at the desired TE as this echo will dominate the image contrast. The time between excitation and the centre of k -space is known as the Effective Echo Time (eTE).

The decrease in acquisition time comes at the expense of RF exposure, the large number of 180° pulses leads to lots of energy in the form of heat being deposited in the tissue being imaged, this is known as Specific Absorption Rate (SAR). SAR limits are imposed when scanning to avoid damaging any tissue and as such TSE with its high RF power can easily exceed these limits. Modern TSE sequences can reduce the angle of the refocusing pulse, however this can come at the expense of quantitative accuracy.

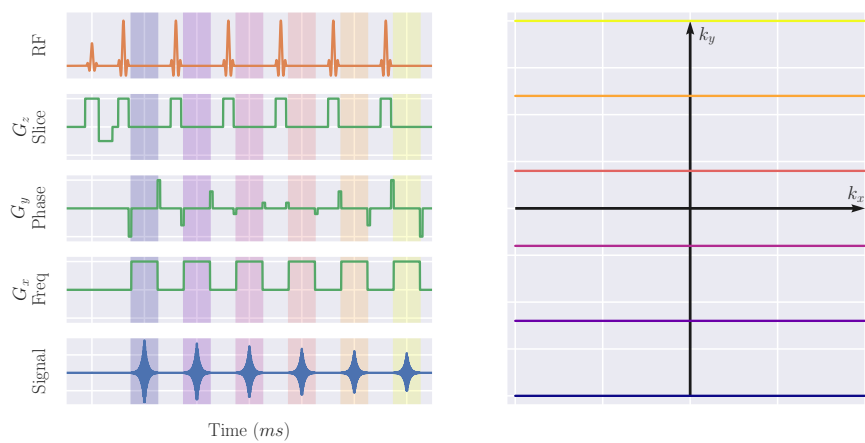


Figure 1.16: A schematic of the TSE pulse sequence and k -space trajectory. The coloured bands on the PSD correspond to the colours of the k -space trajectories. Note this diagram is not to scale.

Half-Fourier Single-shot Turbo spin Echo (HASTE)

The Half-Fourier Single-shot Turbo spin Echo (HASTE) sequence uses a combination of the techniques above. A single excitation is followed by a very long echo train with short echo spacing. This allows a large proportion of k -space to be sampled within a single TR and thus a whole slice is acquired. To minimise the number of lines of k -space acquired and thus the ETL, partial Fourier techniques are utilised. The relatively long TE required for a HASTE sequence means images are normally T_2 weighted.

The advantage of HASTE is its rapid acquisition. It can be used to minimise the effects of motion when scanning uncooperative patients, fetuses or structures the subject has no control over such as the bowel. Alternatively it can be used to capture a large FOV in a single breath hold, thus minimising the effects of inconsistent expiration level, as in Chapter 4. The very long ETL can cause significant blurring of the image, thus reducing its clinical readability.

Turbo Field Echo (TFE)

Turbo Field Echo (TFE), also known as ulatrafast GE, is designed to speed up acquisition of GE images by reducing the TR between excitations. Typical basic GE sequences have relatively long TR to allow the recovery of longitudinal magnetisation. The flip angle used in the TFE sequence is much smaller than the examples explored so far, usually approximately 10° thus leaving a large component of the magnetisation in the longitudinal direction while tipping enough magnetisation into the transverse plane to record a signal at an acceptable SNR. Between each excitation, the transverse magnetisation is spoiled to ensure the images are only T_1 weighted.

After a train of equally spaced RF pulses of Flip Angle (FA), α , and period, TR, the longitudinal magnetisation reaches a steady state, S_{TFE} , after a sufficient number of pulses. This steady state signal depends on the T_1 of the tissue and the FA and TR of the sequence. Assuming perfect transverse magnetisation spoiling between each RF pulse, this equilibrium signal is given by,

$$S_{TFE} = M_0 \frac{\sin(\alpha) [1 - \exp(-TR/T_1)]}{1 - \cos(\alpha) \exp(-TR/T_1)} \exp\left(-\frac{TE}{T_2^*}\right). \quad (1.27)$$

The angle that produces the maximum signal known as the Ernst angle, α_E , and is given

by,

$$\alpha_E = \arccos \left[\exp \left(-\frac{TR}{T_1} \right) \right]. \quad (1.28)$$

Figure 1.17 shows the ratio of the steady state signal to the fully recovered, 90° excitation signal of renal cortex (T_1 of 1376 ms) for a range of flip angles and TR. Additionally the Ernst angle is shown.

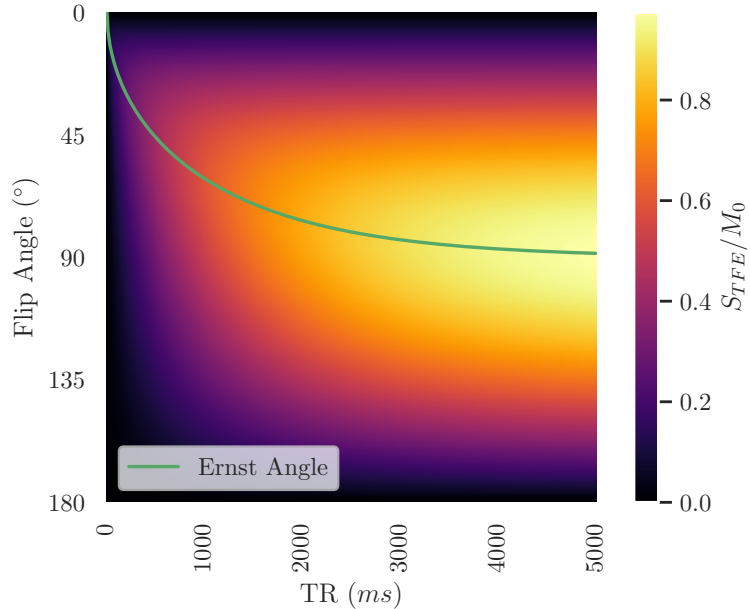


Figure 1.17: The expected steady state signal of a TFE pulse sequence and Ernst angle when imaging renal cortex.

1.4 Conclusion

This chapter has introduced the basic concepts of NMR and MRI required for interpreting this thesis. These techniques are built upon in the experimental chapters for quantification of renal properties, both in-vivo and ex-vivo.

1.5 References

1. Harris, R. K. N.m.r. and the Periodic Table. *Chemical Society Reviews* **5**, 1–22. issn: 1460-4744 (1st Jan. 1976).
2. Bernstein, M. A., King, K. F. & Zhou, X. J. *Handbook of MRI Pulse Sequences* 1041 pp. ISBN: 978-0-08-053312-4. Google Books: d6PLHcyejEIC (Elsevier, 21st Sept. 2004).
3. Westbrook, C. *MRI at a Glance* 138 pp. ISBN: 978-1-119-05354-5. Google Books: WeRbCwAAQBAJ (John Wiley & Sons, 18th Nov. 2015).
4. Bloch, F. Nuclear Induction. *Physical Review* **70**, 460–474 (1st Oct. 1946).
5. Cox, E. F. *et al.* Multiparametric Renal Magnetic Resonance Imaging: Validation, Interventions, and Alterations in Chronic Kidney Disease. *Frontiers in Physiology* **8**. issn: 1664-042X (2017).
6. Lauterbur, P. C. Image Formation by Induced Local Interactions: Examples Employing Nuclear Magnetic Resonance. *Nature* **242**, 190–191. issn: 1476-4687 (5394 Mar. 1973).
7. Mansfield, P. & Grannell, P. K. NMR "Diffraction" in Solids? *Journal of Physics C: Solid State Physics* **6**, L422–L426. issn: 0022-3719 (Nov. 1973).
8. Garroway, A. N., Grannell, P. K. & Mansfield, P. Image Formation in NMR by a Selective Irradiative Process. *Journal of Physics C: Solid State Physics* **7**, L457–L462. issn: 0022-3719 (Dec. 1974).
9. Kumar, A., Welti, D. & Ernst, R. R. NMR Fourier Zeugmatography. *Journal of Magnetic Resonance (1969)* **18**, 69–83. issn: 0022-2364 (1st Apr. 1975).
10. Pruessmann, K. P., Weiger, M., Scheidegger, M. B. & Boesiger, P. SENSE: Sensitivity Encoding for Fast MRI. *Magnetic Resonance in Medicine* **42**, 952–962. issn: 1522-2594 (1999).

Chapter 2

Assessment of Renal T_2 Mapping

Methods

Abstract

This work was presented as an aural presentation at the International Society of Magnetic Resonance in Medicine (ISMRM) 28th Annual Meeting (2020) [1].

Lorem ipsum dolor sit amet, consectetuer adipiscing elit. Ut purus elit, vestibulum ut, placerat ac, adipiscing vitae, felis. Curabitur dictum gravida mauris. Nam arcu libero, nonummy eget, consectetuer id, vulputate a, magna. Donec vehicula augue eu neque. Pellentesque habitant morbi tristique senectus et netus et malesuada fames ac turpis egestas. Mauris ut leo. Cras viverra metus rhoncus sem. Nulla et lectus vestibulum urna fringilla ultrices. Phasellus eu tellus sit amet tortor gravida placerat. Integer sapien est, iaculis in, pretium quis, viverra ac, nunc. Praesent eget sem vel leo ultrices bibendum. Aenean faucibus. Morbi dolor nulla, malesuada eu, pulvinar at, mollis ac, nulla. Curabitur auctor semper nulla. Donec varius orci eget risus. Duis nibh mi, congue eu, accumsan eleifend, sagittis quis, diam. Duis eget orci sit amet orci dignissim rutrum.

2.1 Introduction

2.1.1 Theory

2.2 Methods

2.2.1 Acquisition Schemes

There are multiple methods for acquiring T_2 maps in the kidneys, SE-EPI, Multi-Echo Turbo Spin Echo (ME-TSE), Gradient Spin Echo (GraSE) and T_2 preparation. We wish to compare each of these methods in-vivo and verify their accuracy using a calibrated phantom. A QalibreMD System Standard Model 130 [2] is used for verification. All data is collected on a Philips 3T Ingenia system.

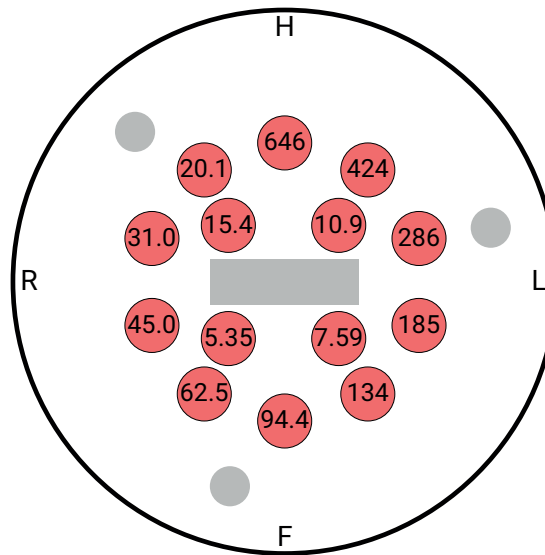


Figure 2.1: A schematic of the T_2 spheres in the QalibreMD phantom.

Spin Echo-Echo Planar Imaging

A series of volumes are collected at a range of echo times using a multi-slice spin echo acquisition with EPI readout. Acquisition parameters are $\text{FOV} = 288 \times 288 \times 25 \text{ mm}$, $\text{voxel size} = 3 \times 3 \times 5 \text{ mm}^3$, $\text{TR} = 5000 \text{ ms}$, $\text{FA} = 90^\circ$, $\text{SENSE} = 2.55$, $\text{halfscan} = 0.844$ and the sequence is respiratory triggered for in-vivo use and has an acquisition time of approximately 9 minutes depending on breathing rate. Volumes are acquired at TE between 20 ms and 70 ms in 5 ms steps with four volumes being acquired at each echo time.

2.2. Methods

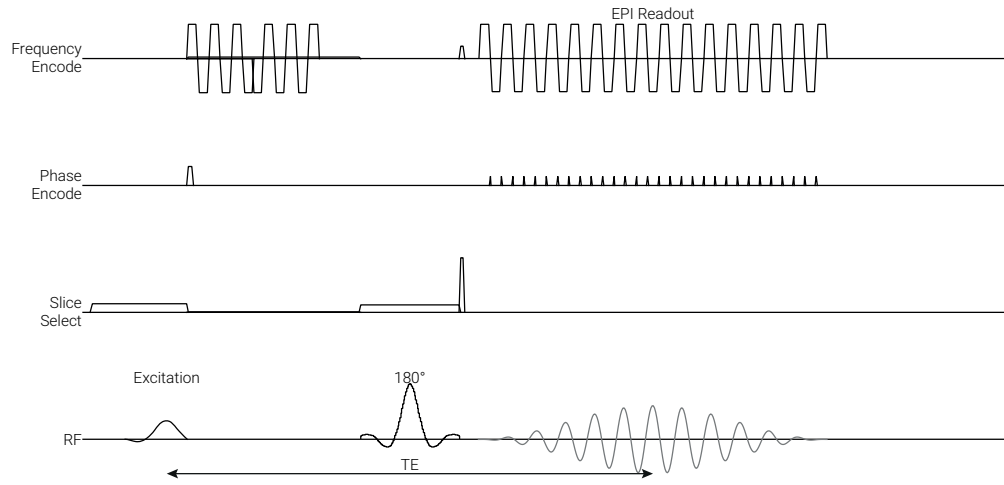


Figure 2.2: A pulse sequence diagram of the SE-EPI scheme.

Multi-Echo Turbo Spin Echo

This method also uses a multi-slice spin echo acquisition however unlike the simple spin echo method, uses a multishot TSE readout. Acquisition parameters for in-vivo scanning are $\text{FOV} = 288 \times 288 \times 25 \text{ mm}$, voxel size = $3 \times 3 \times 5 \text{ mm}^3$, $\text{TR} = 3000 \text{ ms}$, $\text{FA} = 90^\circ$, $\text{SENSE} = 2.55$ and TSE factor = 10; the sequence is respiratory triggered and has an acquisition time of approximately 4 minutes depending on breathing rate. For phantom scanning, the following parameters are modified $\text{FOV} = 250 \times 250 \times 6 \text{ mm}$, voxel size = $0.9 \times 0.9 \times 6 \text{ mm}^3$ and respiratory triggering is removed. Volumes are collected with TE between 13 ms and 130 ms in 13 ms steps.

2.2. Methods

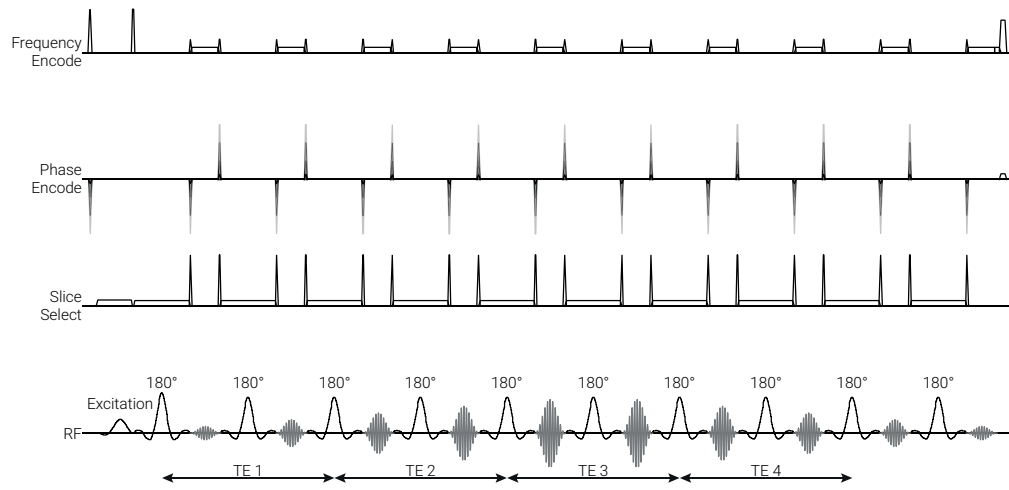


Figure 2.3: A pulse sequence diagram of the ME-TSE scheme.

Gradient Spin Echo

This method also uses a multi-slice spin echo acquisition but with a GraSE readout. Acquisition parameters for in-vivo scanning are $\text{FOV} = 288 \times 288 \times 25 \text{ mm}$, voxel size = $3 \times 3 \times 5 \text{ mm}^3$, $\text{TR} = 3000 \text{ ms}$, $\text{FA} = 90^\circ$, $\text{SENSE} = 2.55$ and TSE factor = 30, startup echoes = 1; the sequence is respiratory triggered and has an acquisition time of approximately 5 minutes depending on breathing rate. For phantom scanning, the following parameters are modified $\text{FOV} = 250 \times 250 \times 6 \text{ mm}$, voxel size = $0.9 \times 0.9 \times 6 \text{ mm}^3$ and respiratory triggering is removed. Volumes are collected with TE between 11.2 ms and 173.3 ms in 5.6 ms steps.

2.2. Methods

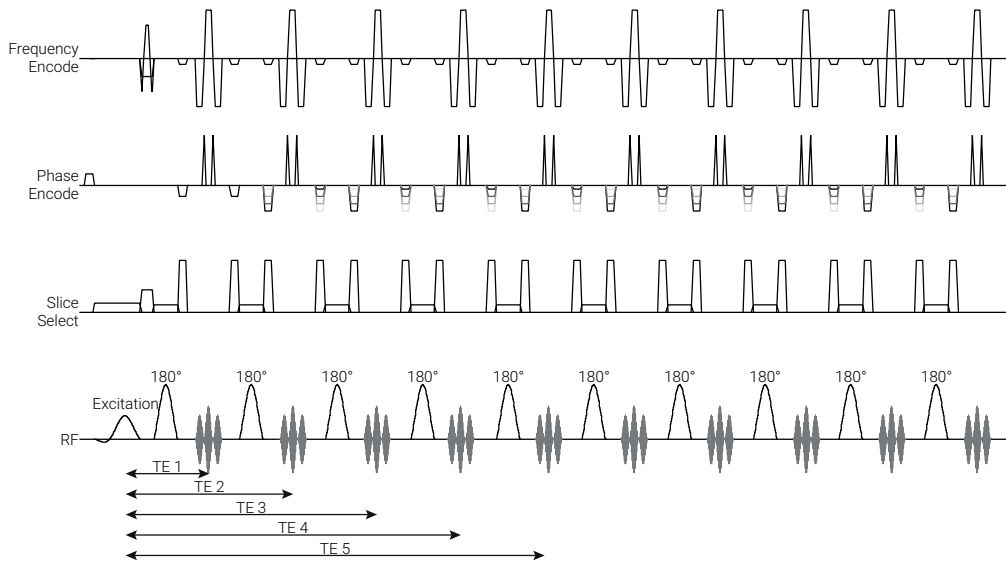


Figure 2.4: A pulse sequence diagram of the GraSE scheme.

T_2 Preparation

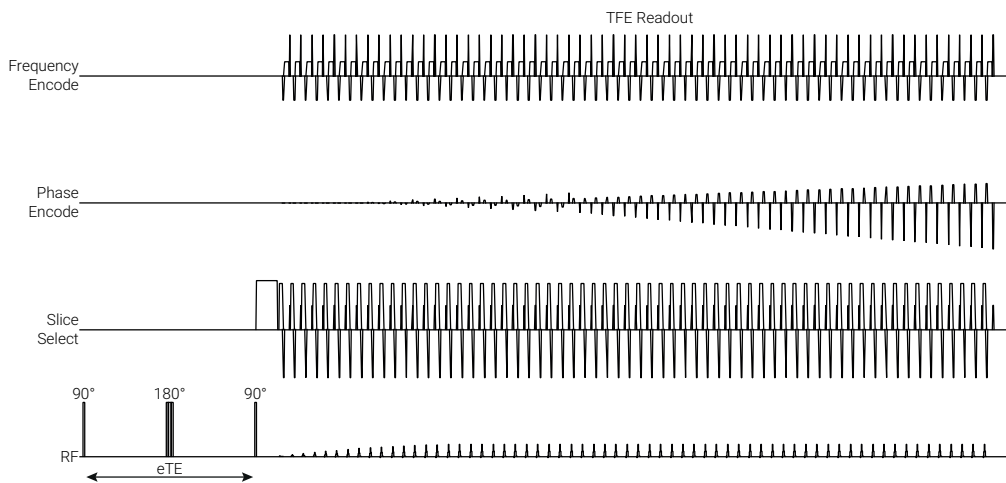


Figure 2.5: A pulse sequence diagram of the basic T_2 preparation scheme.

Basic T_2 Preparation

2.2. Methods

CPMG T_2 Preparation This technique uses a multi-slice Fast Field Echo (FFE) acquisition with a Turbo Field Echo Planar Imaging (TFEPI) readout. Varying degrees of T_2 weighting are applied as a series of 180° preparation pulses for a variable eTE, this is similar to the sequence used in Section 3.2.2. Acquisition parameters for in-vivo scanning are $\text{FOV} = 288 \times 288 \times 25 \text{ mm}$, voxel size = $3 \times 5.65 \times 5 \text{ mm}^3$ (voxel size is limited by the EPI factor), $\text{TR} = 3000 \text{ ms}$, $\text{TE} = 5.3$, $\text{FA} = 90^\circ$, EPI factor = 17, SENSE = 3 and halfscan = 0.733; the sequence is respiratory triggered and has an acquisition time of approximately 6 minutes depending on breathing rate. As the voxel size is already at its minimum, the only modifications made for scanning the phantom are to decrease the FOV to $250 \times 250 \times 6 \text{ mm}$ and remove respiratory triggering. eTEs of 0, 40, 80 and 160 ms are used with three volumes acquired at each eTE

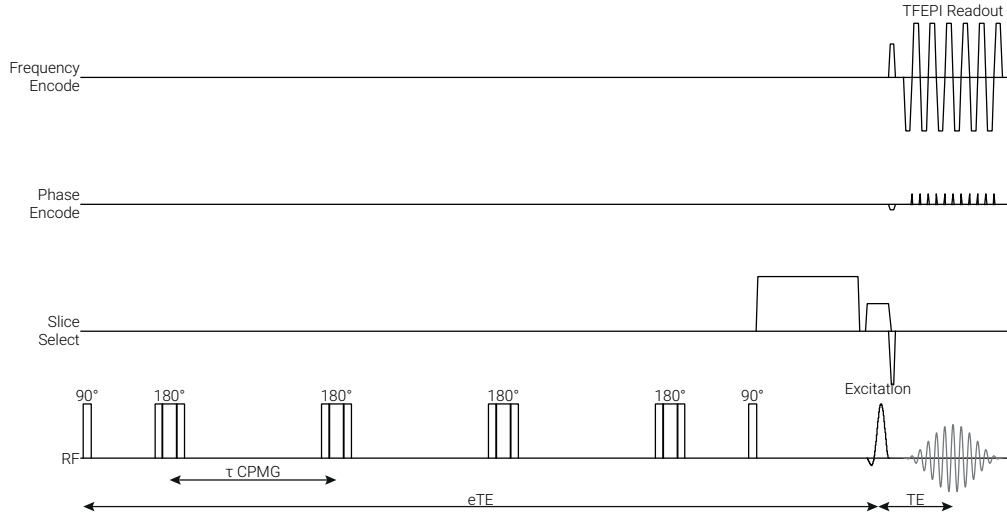


Figure 2.6: A pulse sequence diagram of the Carr-Purcell-Meiboom-Gill (CPMG) T_2 preparation scheme.

2.2.2 Post Processing

Generating T_2 Maps

The data is fit on a voxel by voxel basis using a least squares trust region reflective method to fit the data to Equation (2.1) to estimate T_2 and S_0 with an uncertainty in the fit [3]. For methods where multiple volumes are acquired at an TE, individual volumes are used for the fit e.g. four points at each TE for the SE-EPI method rather than tak-

2.2. Methods

ing mean of the volumes for each TE, this makes potential data the discarding easier. This post-processing is performed by an in-house Python package. Once the T_2 maps have been generated, Region Of Interest (ROI) can be defined for different tissue types or phantom components.

$$S(t) = S_0 \cdot e^{-t/T_2} \quad (2.1)$$

Quantifying T_2 Accuracy

To access the accuracy of each method, the sequences were performed on the calibrated phantom with spheres of known T_2 . By calculating the mean T_2 for each sphere and comparing to the known T_2 it is possible to quantify the accuracy across a range of T_2 and summarise the overall accuracy by Pearson's correlation coefficient, (2.2).

$$r = \frac{\sum_{i=1}^n (x_i - \bar{x})(y_i - \bar{y})}{\sqrt{\sum_{i=1}^n (x_i - \bar{x})^2} \sqrt{\sum_{i=1}^n (y_i - \bar{y})^2}} \quad (2.2)$$

Quantifying Image Quality

Unfortunately MRI doesn't produce perfect images, every signal is subject to a degree of blurring or spreading out into surrounding voxels. The amount of this blurring is different for each sequence and can dramatically effect the readability of an image and ultimately its clinical utility. In MRI the amount and characteristics of the blur are usually spatially invariant, that is to say, if a voxel in the centre of an image is blurred over its five neighbouring voxels in the phase encode direction in the centre of the image, a voxel at the edge of the image would have the same five voxel blur applied to it. We wish to quantify the amount of blurring produced by each of the sequences outlined in 2.2.1.

The observed image, h , can be modeled as the ideal, unblurred signal, f distorted by a filter, g , figure 2.7. This distorting filter is known as the Point Spread Function (PSF) and is the theoretical signal produced by an infinitely small point source object or, in practice, the blurring observed in the imaging system produced when an object much smaller than the system's resolving power is imaged. In a spatially invariant system such as MRI the recorded signal is simply a convolution of the true signal and the PSF i.e. $f * g = h$. By fitting a Gaussian to the PSF we can quantify the degree of blurring in the image.

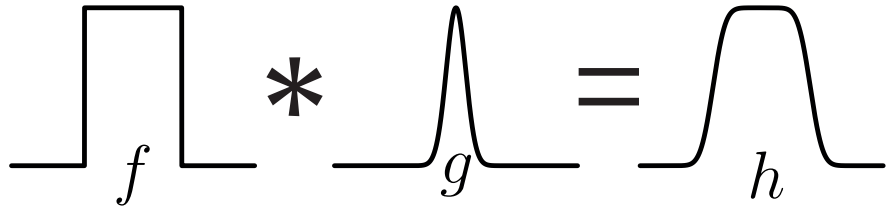


Figure 2.7: The convolution of the ideal signal, f , and the PSF, g , produces the measured signal, h .

To estimate the PSF we acquire an image of the National Institute of Standards and Technology (NIST) phantom at a much higher resolution than the standard T_2 mapping sequence to approximate the ideal signal. The phantom contains lots of clearly defined structures with high contrast edges, therefore, for the $3 \times 3 \text{ mm}^2$ in plane resolution of the sequences, the edges of the structures inside the phantom are smaller than the resolving power of the sequence

Assessment of In-Vivo Feasability

2.3 Results

2.3.1 Sequence Accuracy

We began by comparing the quantitative accuracy of each of the proposed T_2 mapping methods (spin echo EPI, multi-echo TSE, GraSE and T_2 preparation). The QalibreMD System Standard Model 130 phantom used has fourteen spheres with T_2 between 5.35 ms and 645.8 ms spanning the range of T_2 expected in the kidneys, Figure 2.8. This phantom was scanned using each of the methods outlined in 2.2 and a ROI defined for each sphere.

2.3. Results

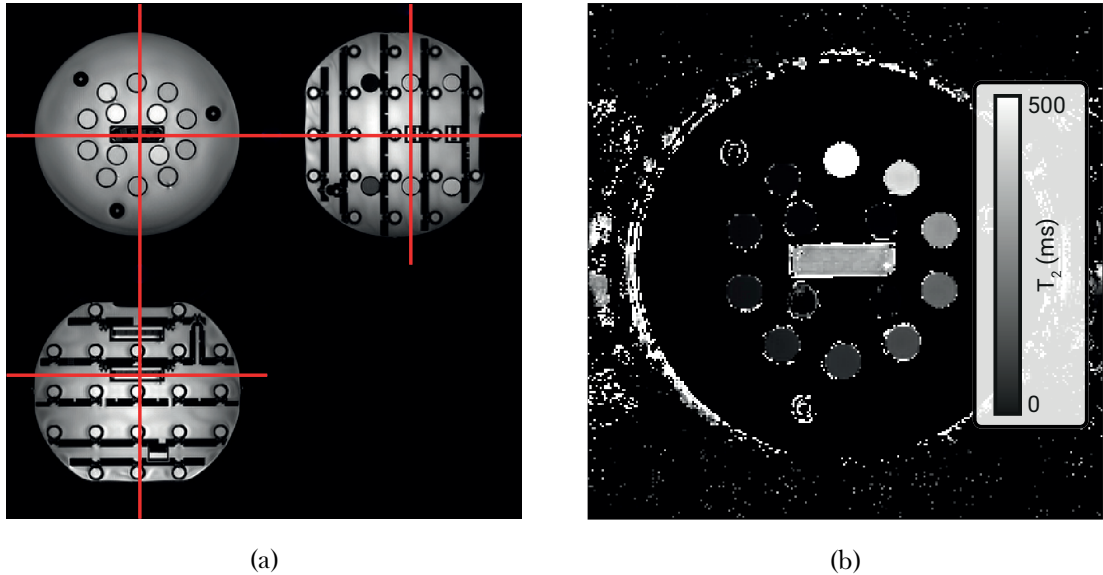


Figure 2.8: (a) The T_2 spheres inside the phantom. (b) An example T_2 map, in this case generated using the GraSE method.

The spin echo method produced vastly over-estimated readings for the spheres of T_2 less than 20 ms (Figures 2.9b) due to the longer minimum TE compared to the other methods. This can be seen in Figure 2.9a where the signal from the shortest T_2 spheres has already mostly decayed. This method did however deliver accurate measurements for the remaining spheres.

More accurate results were generated for shorter T_2 spheres using the ME-TSE method. The raw data (Figure 2.9c) is more noisy, with a sawtooth pattern visible, this additional noise manifests itself as inaccuracies in the longer T_2 measurements where the dynamic range over the TE sampled is smaller.

The GraSE method produced the most accurate measurements although still struggled to measure the sphere with a T_2 of 5.35 ms, Figure 2.9f. The large range of TE and number of volumes collected means this method produced the most accurate results. It also has the benefit of being able to be performed at high resolutions with voxel sizes of 0.9 x 0.9 mm unlike the SE-EPI and T_2 prep methods; this makes it well suited to both in-vivo and ex-vivo measurements.

The data collected using the T_2 prep method (Figures 2.9g and 2.9h) did not fit well due to its small number of data points and large degradation in image quality.

2.3. Results

2.3. Results

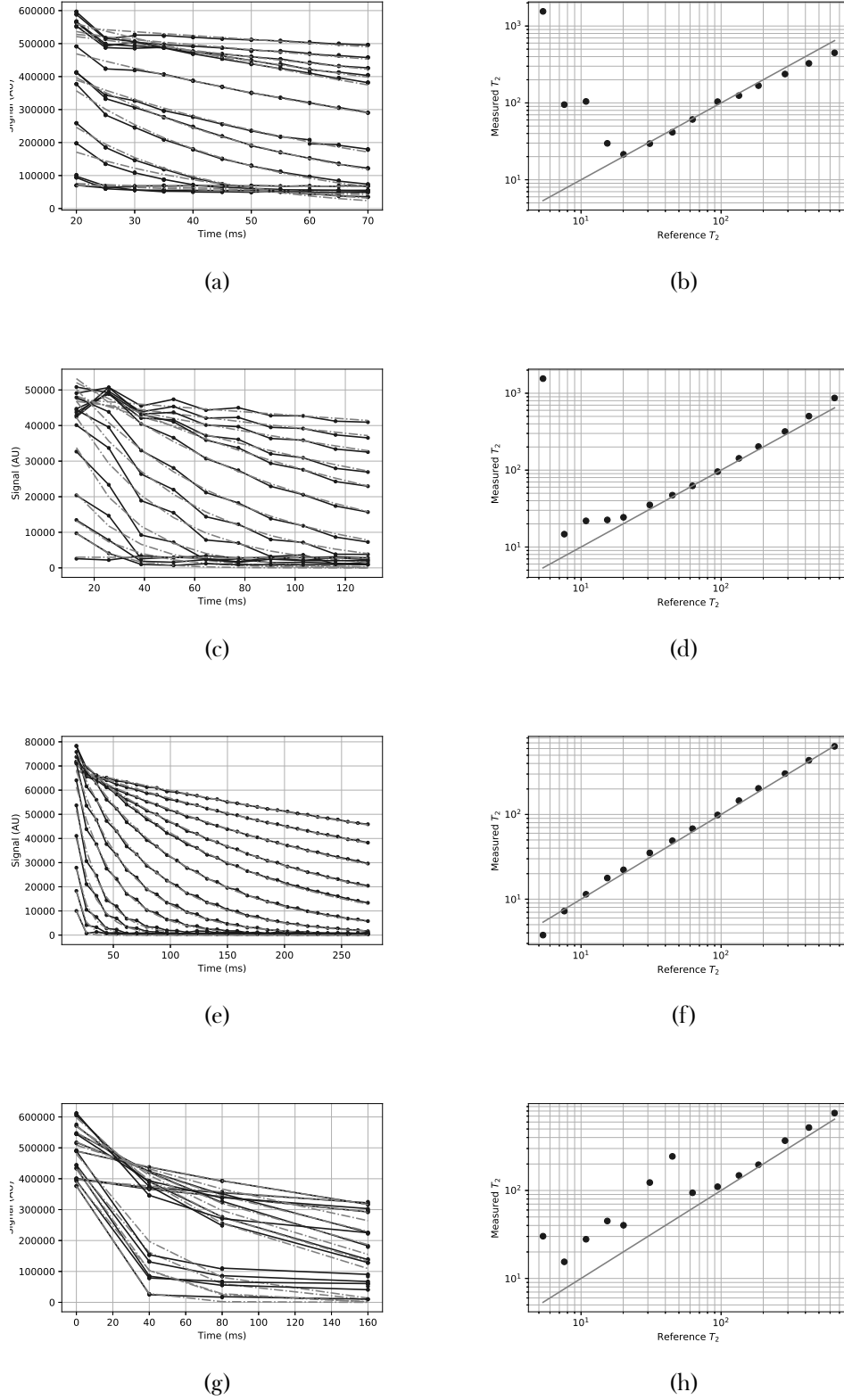


Figure 2.9: Figures (a), (c), (e) and (g) show the raw signal decay for each of the fourteen spheres and the fit decay. Figures (b), (d), (f) and (h) show how the fit T_2 compares to the literature value. Figures (a) and (b) show the results from the SE-EPI method, (c) and (d) show the results form the ME-TSE method, (e) and (f) show the results form the GraSE method and (g) and (h) show the results from the T_2 prep method.

2.3. Results

2.3.2 Image Quality

2.3.3 In-Vivo

T_2 maps using all four methods were collected on the same subject in the same scanning session to allow for a direct comparison of the in-vivo data.

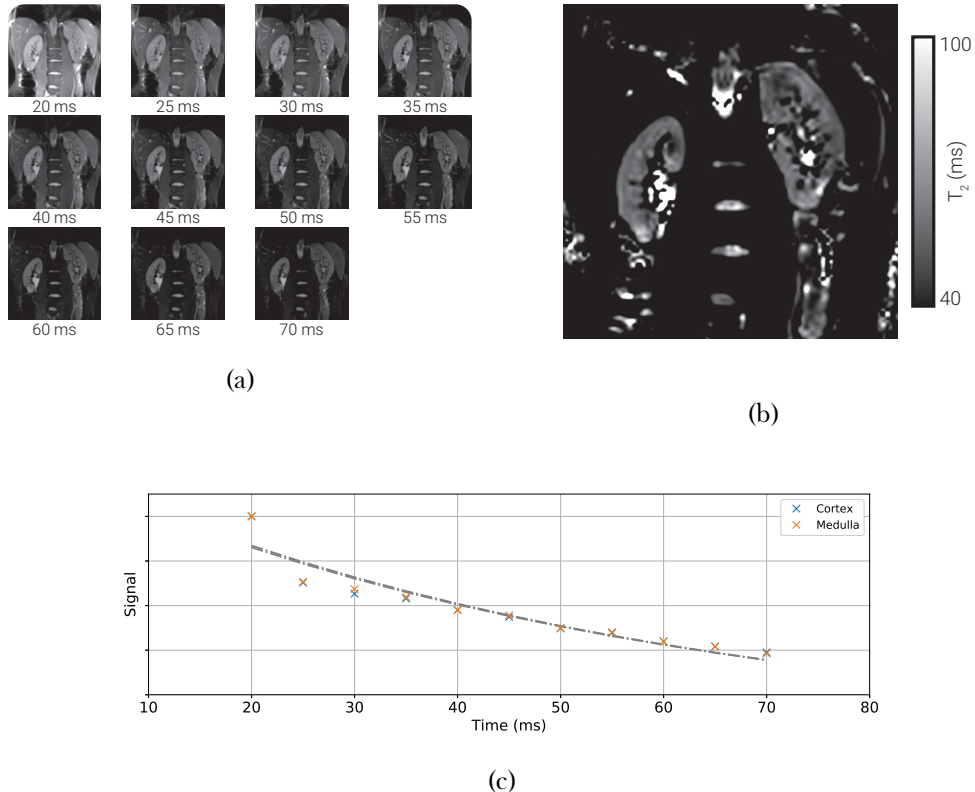


Figure 2.10: (a) The raw data used to generate the SE-EPI T_2 map. (b) An example slice from the SE-EPI T_2 map. (c) The signal decay for the renal cortex and medulla.

The SE-EPI method (Figure 2.10) generated maps with little blurring however there is also a lack of differentiation in T_2 between the renal cortex and medulla. The data collected at TE of 20 ms appears to be artificially high and leads to a reduction in fit T_2 . This sequence is the most susceptible of the methods to patient motion due to the acquisition method of a series per TE, this increase in motion is clear when scrolling through TE.

2.3. Results

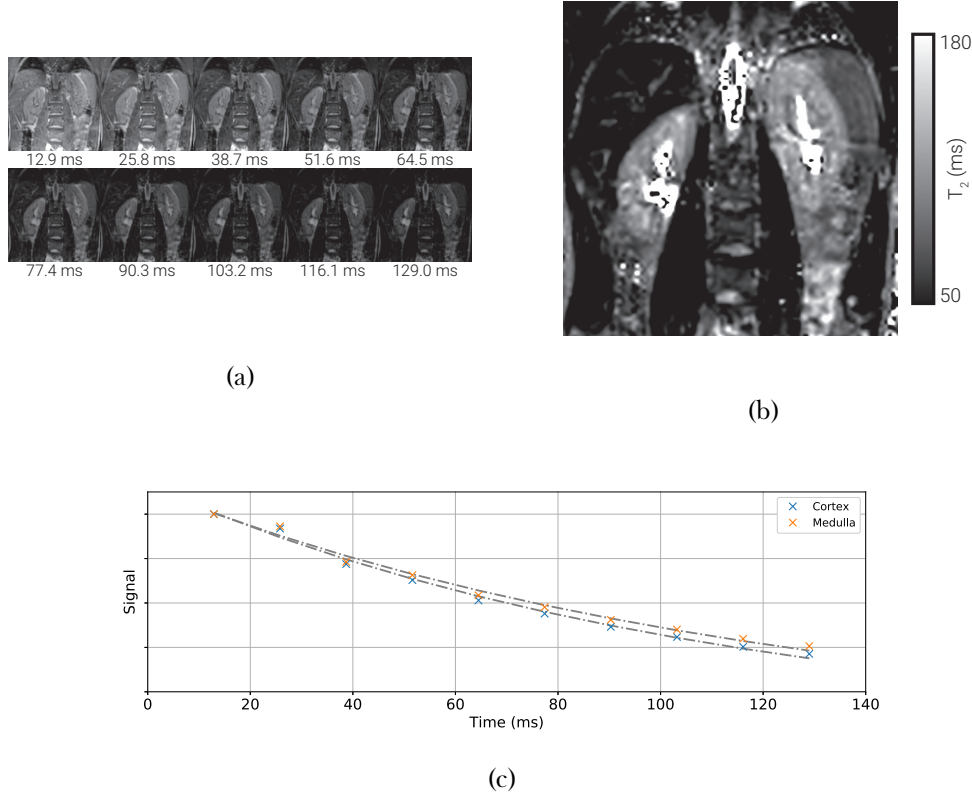


Figure 2.11: (a) The raw data used to generate the ME-TSE T_2 map. (b) An example slice from the ME-TSE T_2 map. (c) The signal decay for the renal cortex and medulla.

The map generated by the ME-TSE method (Figure 2.11) suffers from a large amount of blurring due to the relatively long echo train length. The number of echoes acquired is limited to the TSE factor therefore to acquire ten echoes, a TSE factor of ten needs to be used. This blurring leads to structures being obscured in the map and only a very small differentiation between cortex and medulla.

2.3. Results

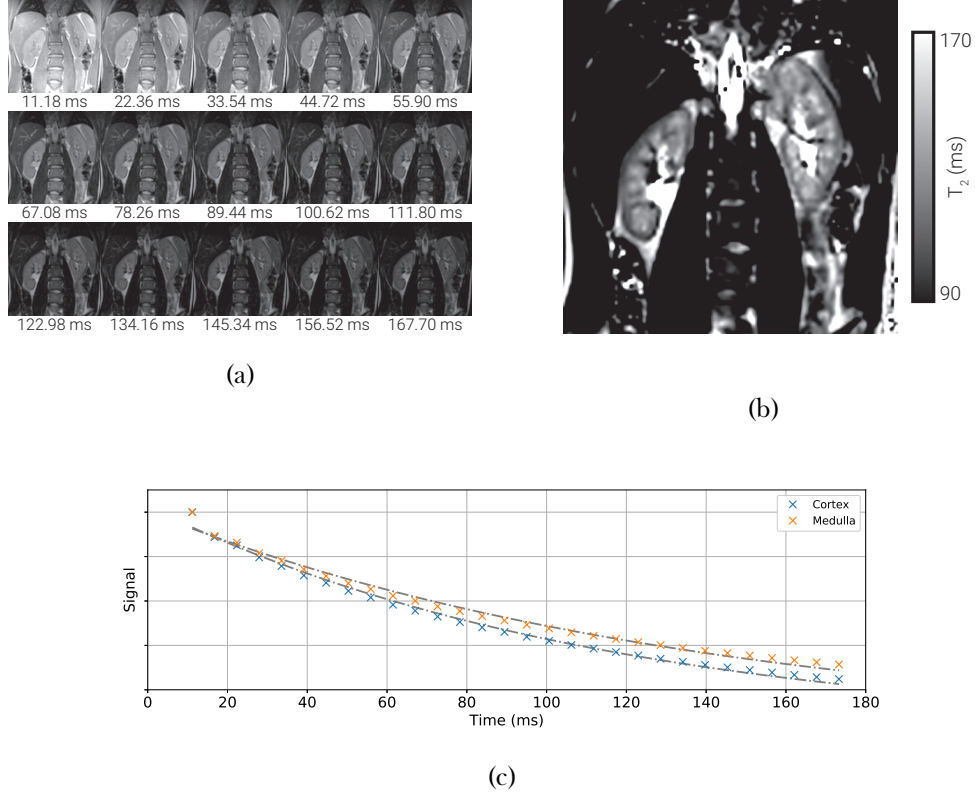


Figure 2.12: (a) The raw data used to generate the GraSE T_2 map. (b) An example slice from the GraSE T_2 map. (c) The signal decay for the renal cortex and medulla.

Using the GraSE method the data in Figure 2.12 was collected. There is a clear difference between cortical and medullary T_2 and the data fits well to a T_2 decay (Figure 2.12c). The signal from the first echo in Figure 2.12c is too intense, this effect was even more pronounced when no startup echoes were used. For tissues with a longer T_2 using two startup echoes would be preferable however this makes measurements of tissues with a short T_2 more inaccurate, as such a compromise of a single startup echo was used. The short echo-spacing made possible by GraSE means more TE can be sampled and therefore leads to a more accurate fit.

2.3. Results

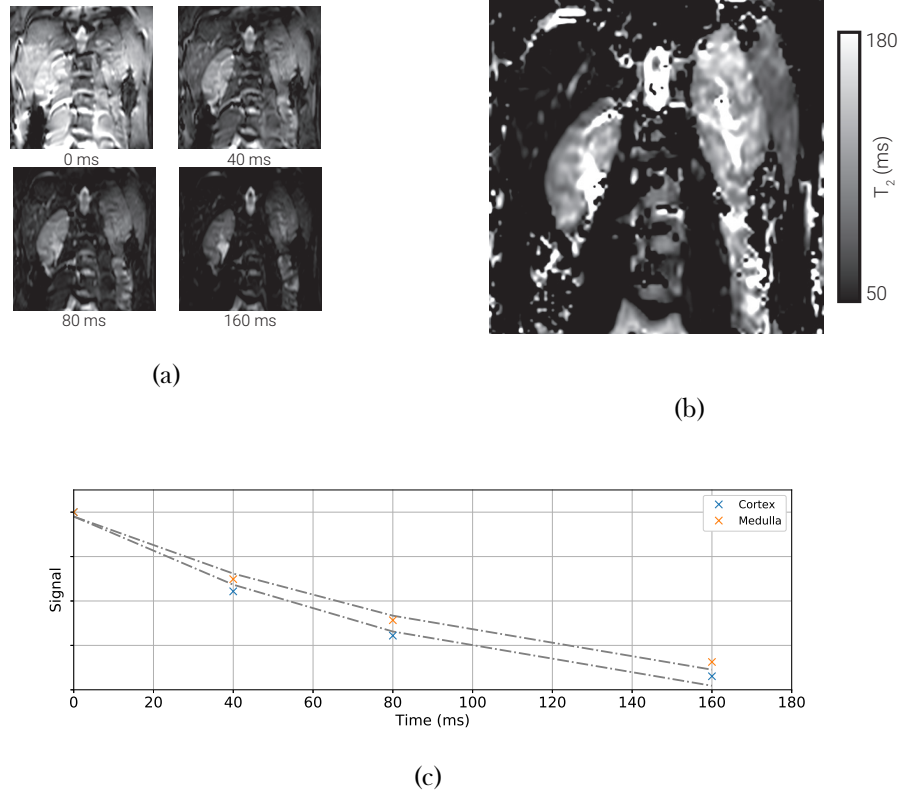


Figure 2.13: (a) The mean data at each eTE used to generate the T_2 preparation T_2 map. (b) An example slice from the T_2 preparation T_2 map. (c) The signal decay for the renal cortex and medulla.

The map made using the T_2 preparation method (Figure 2.13) suffers from noise in the raw data, this is despite there being three acquisitions at each eTE. When comparing Figure 2.13b to Figure 2.12b it's possible to see that some of the areas of greater T_2 do match with the medulla, however the degree of noise in 2.13b means it is un-useable on its own. The small number of eTE collected means the uncertainty in the fit T_2 is higher for this method.

The two methods that have delivered the highest image quality, SE-EPI and GraSE, produce substantially different values of T_2 in-vivo. Even when the data from the 20 ms volume is omitted from the SE-EPI fit, the T_2 is far lower. This is surprising given that when deployed on the phantom, this protocol delivered accurate results over the range of T_2 we see in the kidneys. This disparity is due to the additional confounding factors of diffusion and flow that are present in the body. These factors do not affect the GraSE sequence to the same degree as the SE-EPI sequence.

2.4 Discussion

Of the methods explored, the GraSE sequence produced the most accurate results on the phantom and superior image quality in-vivo, we will use this sequence in T_2 mapping going forward.

2.5 Conclusion

2.6 Acknowledgements

We are grateful for access to the University of Nottingham's Augusta high performance computing service.

2.7 References

1. Daniel, A., Cox, E., Buchanan, C. & Francis, S. *A Comparison of T2 Mapping Methods in the Kidneys* in *Proc. Intl. Soc. Mag. Reson. Med.* 28 International Society of Magnetic Resonance in Medicine Annual Meeting (Online, Aug. 2020).
2. *System Phantom for Diagnostic Quantitative MRI* QalibreMD. <https://www.qalibre-md.com/system-phantom/> (2019).
3. Branch, M., Coleman, T. & Li, Y. A Subspace, Interior, and Conjugate Gradient Method for Large-Scale Bound-Constrained Minimization Problems. *SIAM Journal on Scientific Computing* **21**, 1–23. ISSN: 1064-8275 (1st Jan. 1999).

Chapter 3

Applying T_2 Relaxation Under Spin Tagging (TRUST) To Assess Renal Oxygenation

Abstract

This work was presented as an aural presentation at the ISMRM 26th Annual Meeting (2018) [1].

Lorem ipsum dolor sit amet, consectetuer adipiscing elit. Ut purus elit, vestibulum ut, placerat ac, adipiscing vitae, felis. Curabitur dictum gravida mauris. Nam arcu libero, nonummy eget, consectetuer id, vulputate a, magna. Donec vehicula augue eu neque. Pellentesque habitant morbi tristique senectus et netus et malesuada fames ac turpis egestas. Mauris ut leo. Cras viverra metus rhoncus sem. Nulla et lectus vestibulum urna fringilla ultrices. Phasellus eu tellus sit amet tortor gravida placerat. Integer sapien est, iaculis in, pretium quis, viverra ac, nunc. Praesent eget sem vel leo ultrices bibendum. Aenean faucibus. Morbi dolor nulla, malesuada eu, pulvinar at, mollis ac, nulla. Curabitur auctor semper nulla. Donec varius orci eget risus. Duis nibh mi, congue eu, accumsan eleifend, sagittis quis, diam. Duis eget orci sit amet orci dignissim rutrum.

3.1 Introduction

Sufferers of Chronic Kidney Disease (CKD) can have abnormalities in kidney structure or reduced urine function. More quantitatively CKD can be assessed clinically by Glomerular Filtration Rate (GFR), the rate at which fluid is filtered through the kidneys, with a value below 60 ml/min/1.73m² of body surface area being diagnostic or the presence of albumin, the main protein in blood plasma, in the patients urine [2–4]. An estimated 5–11% of the global population suffer from CKD [5–9] making it a significant public health concern. Late referral of renal disorders results in an increase in mortality rate and treatment costs [10–12]. Given that in 2013/2014 renal services cost the United Kingdom’s National Health Service £586 million [13] there are clear health and economic advantages to an early diagnosis of CKD.

The current methods available to study CKD are not ideal for a variety of reasons. Histological samples are the gold standard for studying renal tissue however collecting them is an invasive process and as such they are not suitable for monitoring the progress of a patient’s condition on a regular basis. This coupled with the fact that a small sample is not representative of the entirety of both kidneys means that this method has large drawbacks. Ultrasound can be used to gather structural information about the kidneys non-invasively, however, it suffers from low spatial resolution and the images being difficult to interpret. The most common method of diagnosis is to estimate GFR from the creatinine content in a blood sample however this measure does not allow for the individual assessment of each kidney and is an indirect measure of kidney tissue damage.

MRI is a flexible non-invasive tool that can be used to collect a wealth of information about the kidneys. A current research interest at the Sir Peter Mansfield Imaging Centre (SPMIC) is to use multi-parametric renal MRI to assess and predict CKD. This protocol assesses haemodynamics, oxygenation and microstructure in a single 45 minute scanning session and shows significant changes in certain combinations of parameters in subjects with CKD as opposed to healthy volunteers [14]. Currently oxygenation is assessed using Blood Oxygen Level Dependent (BOLD) T_2^* maps to measure oxygenation of different tissues within the kidney, predominately the separation in mean T_2^* between the renal cortex and medulla, an example of which is shown in Figure 3.1. These BOLD T_2^* maps are, however, affected by other factors such as susceptibility effects, shimming and baseline blood flow and thus may be limited in their ability to draw quantitative conclusions despite their widespread

use [4, 15].



Figure 3.1: An example T_2^* map. A clear difference can be seen between the renal medulla and cortex.

A welcome addition to this multi-parametric model would be the assessment of Renal Metabolic Rate of Oxygen (RMRO_2); a measure analogous to the Cerebral Metabolic Rate of Oxygen (CMRO_2) [16]. This measure can be calculated via Equation (3.1)

$$\text{RMRO}_2 = (Y_a - Y_v) \times \text{RBF} \times [\text{Hct}] \quad (3.1)$$

where Y_a and Y_v are arterial and venous oxygen saturation respectively, RBF is renal blood flow (in ml/min) and Hct is the ratio of the volume of erythrocytes to the volume of the rest of the blood, known as haematocrit. Renal Blood Flow (RBF) can be measured relatively easily using Phase Contrast (PC)-MRI [17] and Hct is usually taken to be 0.41 for healthy adults but can be measured from a simple blood test [18, 19] or using the correlation between T_1 of blood and its haematocrit [20]. This means that only a measurement of blood oxygen saturation via a non-invasive protocol is required to generate a quantitative value of RMRO_2 .

Blood oxygen saturation can be measured precisely via the insertion of catheters into the patient, however this is clearly an invasive process [21]. There are currently two well established methods of measuring blood oxygenation via MRI however these have only been used in the brain thus far. These methods are T_2 Relaxation Under Spin Tagging (TRUST) [22–25] and susceptibility-based oximetry [26–29]. TRUST builds on the ideas of an Arterial Spin Labelling (ASL) sequence in the fact that by subtracting control images from labelled images only blood is imaged. However, instead of labelling a slab of tissue in the

3.1. Introduction

neck and imaging a superior slice, when implementing TRUST the imaging plane is inferior to the labelled slab. By collecting a series of pairs of labelled and control images with different T_2 weightings it is possible to fit the data from the sagittal sinus to a T_2 relaxation and use a calibration curve to convert the value of T_2 to venous oxygenation [30]. Susceptibility-based oximetry is based upon the differences in magnetic susceptibility between the blood and the surrounding tissue. Using a phase map it is possible to model this difference in susceptibility and using the known difference in susceptibility between fully oxygenated blood and fully deoxygenated blood, venous oxygenation can be calculated.

Here both of the above techniques are applied to study oxygenation in the renal vein in young healthy individuals to assess the technicalities of transferring these protocols from the brain to the body. Given that these techniques have already been used in the brain with a number of studies in the literature, the sequences are first implemented on the brain to assess oxygenation in the superior sagittal sinus, then adapted to work within the more challenging environment of below the neck applications. These adapted sequences are compared to the results gained using the established techniques in the brain before testing on the renal vein. An oxygen challenge is carried out to verify that changes in oxygenation can be measured in the renal vein. If proved successful these sequences will be incorporated into the multi-parametric renal MRI protocol.

3.2 Methods

Imaging was performed on a whole body 3 Tesla MRI scanner (Ingenia, Philips Medical Systems, The Netherlands) using a 32 channel head or body coil. Studies were carried out according to the principles of the Declaration of Helsinki and approved by either the Local Ethics Committee or the East Midlands Research Ethics Committee. Written informed consent was obtained from all subjects.

3.2.1 Susceptibility-Based Oximetry

MRI Protocol

The principle behind susceptibility-based oximetry is based on the fact that there is a difference in magnetic susceptibility between the blood within a vessel and the tissue surrounding it [31]. As outlined by Jain, if a blood vessel is modelled as a long paramagnetic cylinder, it is possible to calculate the oxygenation of the blood by knowing the phase difference between blood in the vessel and the surrounding tissue, the angle of the vessel to the B_0 field, the echo time of the scan and the subject's haematocrit [26]. This relationship is shown in Equation (3.2).

$$Y_v = \left[1 - \frac{2|\Delta\phi|}{\gamma TE \Delta \chi_{do} B_0 (\cos^2 \theta - 1/3) Hct} \right] \times 100 \quad (3.2)$$

where $\Delta\phi$ is the average phase difference between the blood in the vessel and the surrounding tissue, γ is the gyromagnetic ratio of a proton, TE is the echo time, $\Delta\chi_{do}$ is the susceptibility difference between fully deoxygenated and fully oxygenated blood ($4\pi \times 0.27$ p.p.m) [32, 33], B_0 is the static field strength, θ is the angle of the vessel to the B_0 field and Hct is the subjects haematocrit. Given haematocrit can be assumed or is measured with a blood test or by measuring the T_1 of the blood, this means that from a simple phase map it is possible to calculate Y_v . The optimum phase map for this purpose was produced using a 2D T_1 weighted FFE sequence with a flip angle of 25° , flow compensation, coil homogeneity correction and flyback. The FOV was $230 \times 184 \times 29$ mm, matrix size of 400×300 , TR of 12 ms, TE of 7.5 ms and three signal averages. This led to a total acquisition time of 9 seconds and as such could be completed in a single breath hold if required.

3.2. Methods

Analysis

Once the phase map has been acquired, a ROI containing the superior sagittal sinus was defined. This mask was then dilated with concentric shells to generate the two ROI shown in Figure 3.2, note that the outer ROI has been constrained to within the brain during its dilation. There were no occurrences of phase wrapping in or immediately surrounding the superior sagittal sinus observed due to its small size and the high field homogeneity within the head and of the 3T scanner used. Any occurrences of phase wrapping could easily be corrected using Phase Region Expanding Labeller for Unwrapping Discrete Estimates (PRELUDE), a tool within fMRIB Software Library (FSL) (fMRIB, The University of Oxford) [84]. The average values of phase within these two ROI along with the angle of the vessel to the B_0 field, as calculated from the localisation scans can then be used with Equation (3.2) to calculate Y_v .

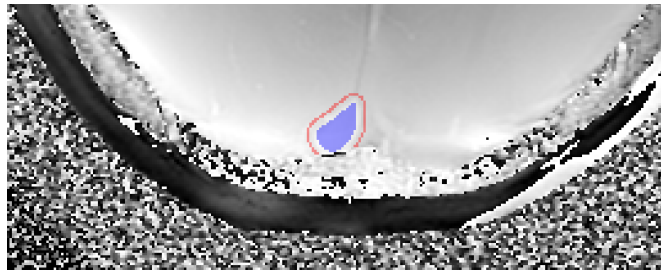


Figure 3.2: The region of interest averaged to find the intra-vascular phase (blue) and the region of interest used to find the phase of the surrounding tissue (red).

3.2.2 T_2 Relaxation Under Spin Tagging

MRI Protocol

The protocol for the TRUST MRI sequence in the brain involves the acquisition of a series of paired images using the pulse sequence shown in Figure 3.3a. A series of presaturation pulses using the Water suppression Enhanced through T_1 effects (WET) scheme are applied to the imaging slice, shown in Figure 3.3b, to reduce the signal from static tissue and reduce contamination of the magnetisation in the imaging slice by an imperfect labelling slab profile [35, 36]. In the first of each image pair, a labelling pulse is applied consisting of two successive slice-selective 90° RF pulses to generate a 180° label. The next image in the sequence has a control pulse applied to it instead of a labelling pulse, in this image the second of the 90° pulses is applied 180° out of phase to give zero net effect. As such any effects of magnetisation transfer related signal in the stationary tissue can be cancelled out

3.2. Methods

because the net RF effect on the macromolecular spin magnetization is identical for both the labelling pulse and control pulse. This method of labelling is known as Transfer Insensitive Labelling Technique (TILT) and is widely used in literature for labelling in TRUST in the brain [37]. A series of non-selective T_2 preparation pulses are then applied to minimise the blood outflow effect and modulate the T_2 weighting of the image, the time between the application of the labelling pulse and the T_2 preparation is known as the Post Label Delay (PLD). Finally a 90° excitation pulse is applied followed by a standard EPI readout at time TE later [23]. If the control image is subtracted from the labelled image then only the venous blood that flowed from the labelled slab to the imaging slice will be visible, as shown in Figure 3.4.

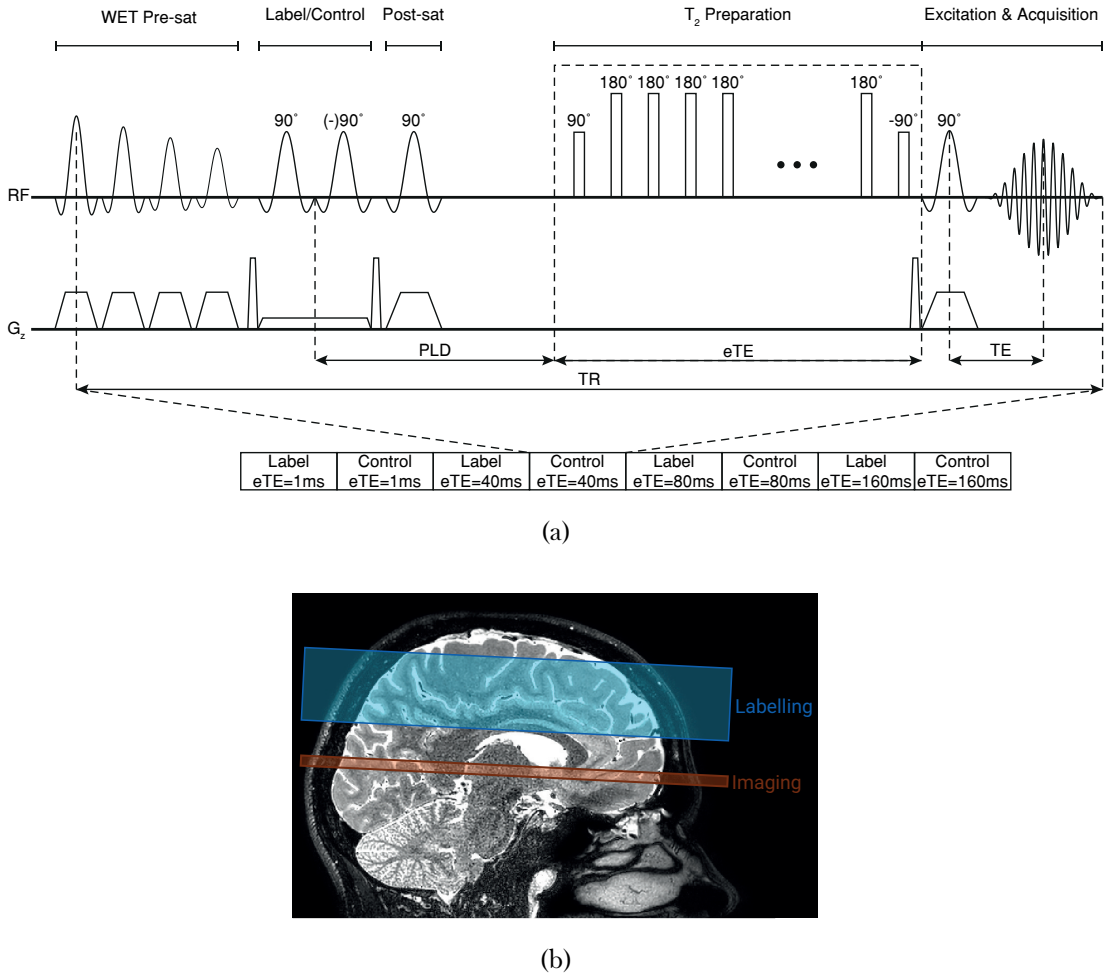


Figure 3.3: (a) The pulse sequence for TRUST MRI using the TILT labelling sequence. (b) The labelling and imaging volumes used for TILT tagging within the brain.

3.2. Methods

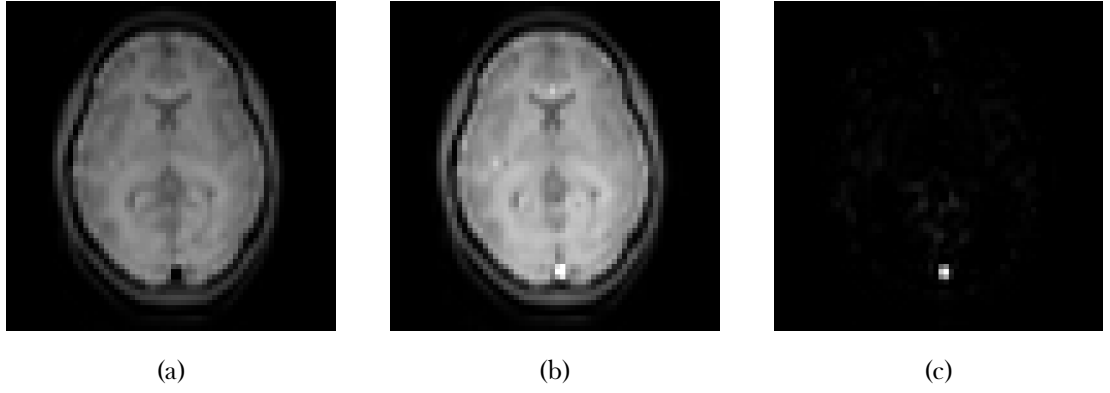


Figure 3.4: The control image, (a), is subtracted from the labelled image, (b), to generate a difference image, (c), of only the tagged blood.

This process is then repeated for another pair of images, however, this time the duration of the T_2 preparation is increased to a larger eTE, this applies a T_2 weighting to the image in addition to the constant weighting caused by the regular TE. Three label/control image pairs were acquired with each eTE of 1 ms, 40 ms, 80 ms and 160 ms.

The resulting signal in the superior sagittal sinus of the difference between the labelled image and control image, ΔS , is defined by Equation (3.3)

$$\begin{aligned}
 \Delta S &= S_{\text{label}} - S_{\text{control}} \\
 &= S_{\text{blood label}} - S_{\text{blood control}} \\
 &= S_0 e^{eTE(1/T_1 - 1/T_2)} \tag{3.3}
 \end{aligned}$$

where $S_0 = 2e^{-T_1/T_1 - TE/T_2^*}$ and; T_1 , T_2 and T_2^* are the relaxation constants of blood. If it is assumed that T_1 of blood is approximately 1624 ms [38] then it is possible to fit the collected data to a mono-exponential function and find an estimate of T_2 . It is deemed acceptable to use a mean value of T_1 as it will always be much greater than the value of T_2 and thus the possible small changes in T_1 due to blood oxygenation and haematocrit become negligible when fitting the T_2 curve.

The final step in this procedure is to convert the value of T_2 into one of Y_v . The relationship between T_2 and Y_v is relatively well known and as such a simple empirically derived calibration curve can be used for this conversion, Figure 3.5 [19, 39, 40].

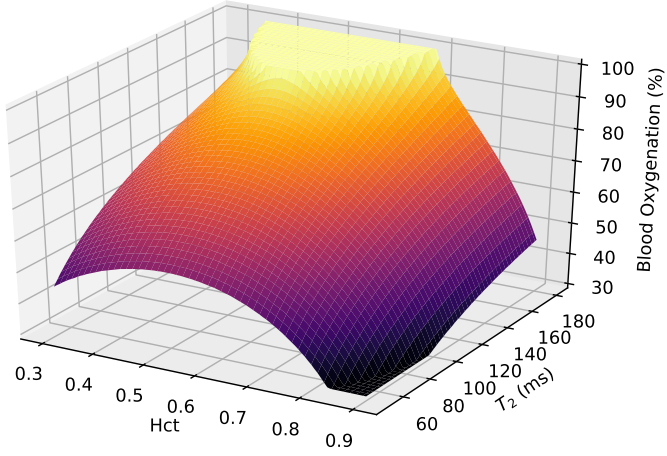


Figure 3.5: The calibration curve used to convert between T_2 and Y_v for a given haematocrit [41].

The parameters used in the brain TILT TRUST sequence were as follows: label slab thickness = 100 mm, imaging slice thickness = 5 mm, distance between centre of imaging slice and centre of labelling slice = 75 mm, FOV = $220 \times 220 \times 5$ mm, matrix size = 64×64 , voxel size = 3.44×3.44 mm, SENSE = 3, EPI factor = 15, T_1 = 1624 ms, PLD = 1022 ms, the choice of this value will be explored later, TR = 3000 ms, TE = 2.9 ms, eTE = 1 ms, 40 ms, 80 ms and 160 ms with three pairs of images acquired at each. This led to a total scan duration of approximately 84 seconds.

3.2. Methods

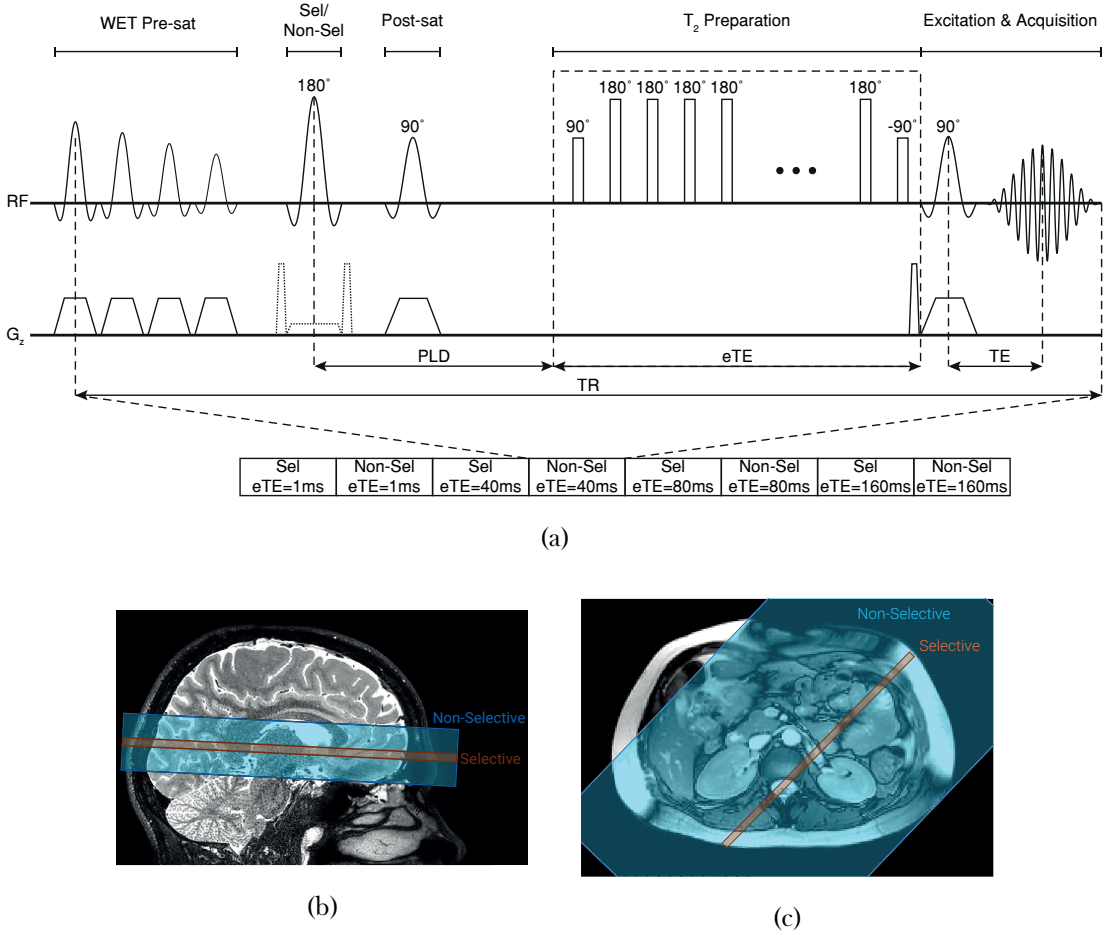


Figure 3.6: (a) The pulse sequence for TRUST MRI using the FAIR labelling sequence. (b) The selective and non-selective volumes used for tagging via FAIR in the brain. (c) The selective and non-selective volumes used for tagging via FAIR in the kidneys.

The main hurdle to be overcome when moving TRUST to the body is the inhomogeneity in the magnetic field caused by the far less homogeneous tissue susceptibilities within the body compared to the brain. These inhomogeneities mean that it is not possible to use TILT as the labelling method, instead the Flow-sensitive Alternating Inversion Recovery (FAIR) labelling scheme will be used [42], a diagram of this pulse sequence is shown in Figure 3.6a. In the FAIR labelling scheme a selective inversion pulse is applied with slice selective gradients turned on followed by T_2 preparation and acquisition to generate the first image in the pair, a non-selective inversion pulse is then applied with a lower slice selective gradient followed by T_2 preparation and then acquisition to generate the second image. An example of the raw images produced is shown in Figure 3.7. A schematic of the selective and non-selective slices in the brain and the renal vein are shown in Figures 3.6b and 3.6c respectively. This sequence also has the advantage of being far easier to plan, in the brain having a separate labelling and imaging slice is relatively trivial however the flow of blood

3.2. Methods

in the body is far less ordered and as such, the use of a selective slab within a non-selective slab yields far better results. Movement is a much greater problem in the body. Given the long acquisition time of TRUST it is impossible to carry out the scan in a breath hold, as such the sequence is respiratory triggered via a respiratory belt applied around the subjects chest. The total scan time is therefore dependent upon respiratory rate. Depending on the subject, a delay can be applied between the respiratory trigger and the labelling pulse to acquire images while the subject has fully exhaled.

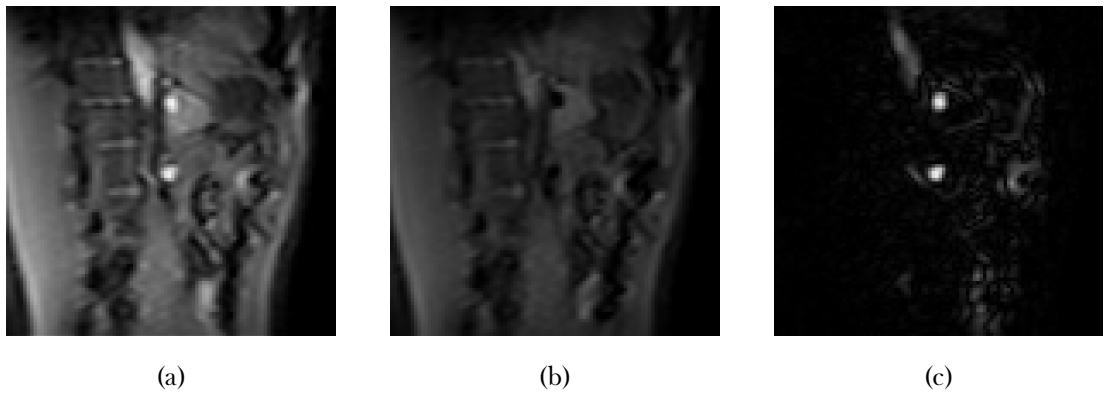


Figure 3.7: The raw images generated when using the FAIR labelling sequence on the kidneys. The non-selective image, (a), is subtracted from the selective image, (b), and generates (c), an image of only the untagged blood. The raw FAIR images from the brain are omitted as they are very similar to those seen in Figure 3.4.

When using the FAIR labelling sequence on the brain the following parameters were used: selective slab thickness = 25 mm, non-selective slab thickness = 400 mm, FOV = $220 \times 220 \times 5$ mm, matrix size = 64×64 , voxel size = $3.44 \times 3.44 \times 5$ mm, SENSE = 3, EPI factor = 15, T_1 = 1624 ms, PLD = 800 ms, TR = 7276 ms, TE = 2.9 ms, eTE = 1 ms, 40 ms, 80 ms and 160 ms with three pairs of images acquired at each. When used on the body, the parameters were as follows: selective slab thickness = 25 mm, non-selective slab thickness = 400 mm, FOV = $244 \times 244 \times 5$ mm, matrix size = 96×96 , voxel size = $3.44 \times 3.44 \times 5$ mm, SENSE = 3, EPI factor = 15, T_1 = 1624 ms, PLD = 1000 ms, the choice of this value will be explored later, TR = 8076 ms, TE = 2.9 ms, eTE = 1 ms, 40 ms, 80 ms and 160 ms with three pairs of images acquired at each.

Analysis

The analysis of the data collected using the above protocol was carried out using custom MATLAB (MathWorks, Natick, MA) software based upon code written by Liu and modified to work with data collected using the FAIR labelling method by Cox [43]. This software loads the data and carries out the subtraction of each image pair then presents a difference image to the user so the vessel can be drawn around. At this point the voxels with the greatest intensity within the vessel, four voxels when calculating Y_v for the superior sagittal sinus and nine voxels when working on the renal vein, are averaged, as are the intensities of each repeat eTE. These mean signals are then fit to Equation (3.3) to compute a value of T_2 with confidence bounds. The value of Y_v can then be found using the aforementioned calibration curve. Once the software has finished, it saves all outputs and intermediary variables to a file on the computer for later analysis.

3.2.3 Inducing Changes in Oxygenation of Blood in the Renal Vein

In order to assess the ability of these methods to measure a change in renal oxygenation, a method of inducing such a change in the kidneys needed to be devised. Looking at literature that has carried out similar studies, it is suggested that changes in renal oxygenation can be induced by either varying the subjects sodium intake, water intake or inspired oxygen level [44, 45].

Due to the challenges associated with controlling subjects diet for two weeks as was performed in Prijim [46], the use of sodium intake was discounted. From previous work we know that applying a large water load to subjects during the scanning session, as in Tumkur and Prasad [47, 48], can cause undesired effects on the resultant shim as assessed by B_0 maps due to the large susceptibility change adding such a large quantity of water to the abdomen can cause, as such, this method was also discounted leaving us to pursue an oxygen challenge.

This method consisted of localisers and anatomical images being collected followed by alternating BOLD T_2^* and TRUST scans while the subject was breathing room air to record a baseline. Pure oxygen was then delivered to the subject at 15 ℓ/min via a gas mask and, after a two minute wash in period, the BOLD T_2^* and TRUST scans were repeated. A visual representation of this protocol can be seen in Figure 3.8. The BOLD T_2^* scans had a slice thickness of 5 mm, 12 echoes with an initial TE of 5 ms and subsequent echo spacing of 3

3.2. Methods

ms, the flip angle was 30° . The total scan time was approximately 17 seconds and was acquired during a single breath hold. The TRUST scans were conducted as per Section 3.2.2.

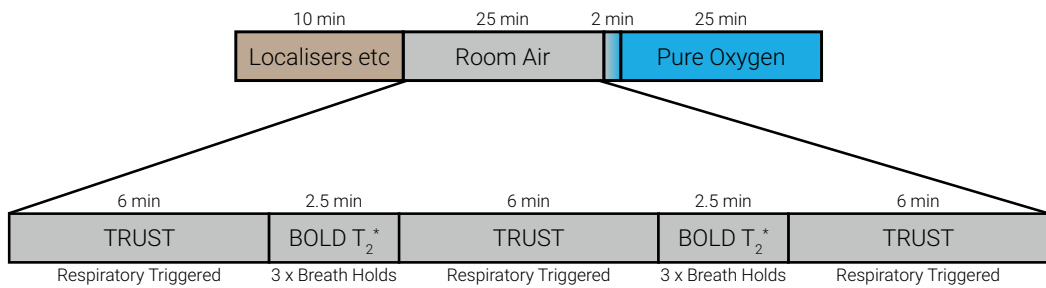


Figure 3.8: The protocol used to induce changes in renal oxygenation.

3.3 Results and Discussion

3.3.1 Susceptibility-Based Oximetry

Susceptibility-Based Oximetry in the Brain

Having collected data using the method outlined in 3.2.1 it was possible to use Equation (3.2) to estimate Y_v in the superior sagittal sinus to be $63 \pm 2.1\%$. This is consistent with the value reported by Liu of $61.1 \pm 1.4\%$ found in a multi centre TRUST trial with 250 participants over a wide range of ages and ethnicity distribution [25].

Susceptibility-Based Oximetry in the Renal Vein

Having calculated an acceptable result in the brain that agreed with literature it was possible to move onto applying techniques to assess oxygenation in the renal vein. A set of three phase maps were collected along with three localisers, one along each plane. If $\Delta\phi$ is plotted against θ for a typical Y_v of 85%, Figure 3.9 is produced. It can be seen that, for an expected Y_v , the phase difference is greatest if the vessel runs parallel to the B_0 field. No part of the renal vein is located parallel to the B_0 field, typically the angle is in the region of 75° (there is a large degree of variability in vasculature geometry between subjects) and as such delivers a very small phase difference. This coupled with the fact that the gradient of this function at these angles is large, meaning that the uncertainty in angle corresponds to a larger uncertainty in Y_v means it will unfortunately not be possible to use susceptibility-based oximetry to accurately measure Y_v within the renal vein.

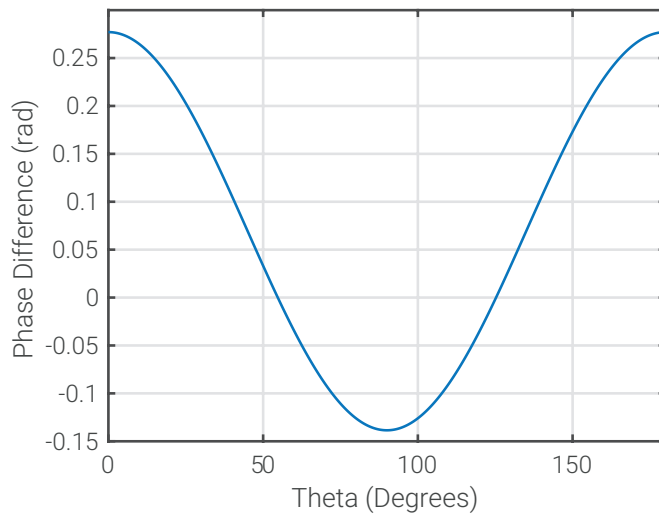


Figure 3.9: For a typical Y_v of 85% the phase difference produced by a vessel at a range of angles to B_0 .

3.3. Results and Discussion

This technique would perhaps be better suited to use in the liver to assess oxygenation in the portal vein. This vessel runs at a much smaller angle to the B_0 field and as such the model will still be valid with reasonable errors, Figure 3.10. This would potentially work much better than TRUST here as the sequence is much quicker and therefore will be less susceptible to movement.

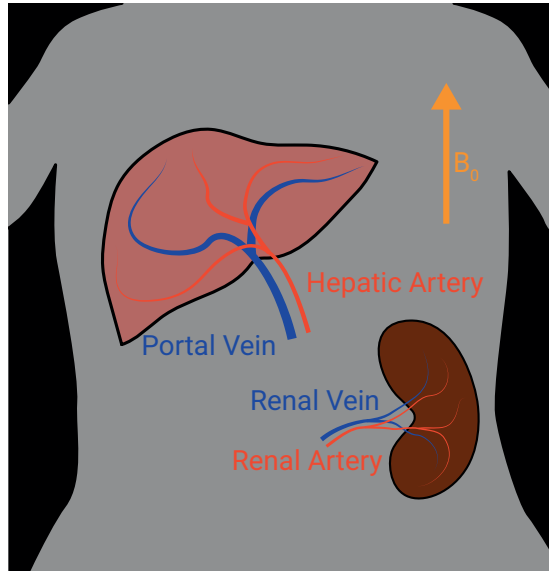


Figure 3.10: A schematic of the portal and renal veins entering the liver and left kidney respectively in relation to the B_0 field.

3.3.2 T_2 Relaxation Under Spin Tagging

TRUST in the Brain

To test if the FAIR labelling sequence delivered the same signal decay as the TILT sequence both labelling schemes were performed sequentially on the superior sagittal sinus with a PLD of 800 ms. The resulting normalised signals are shown in Figure 3.11.

3.3. Results and Discussion

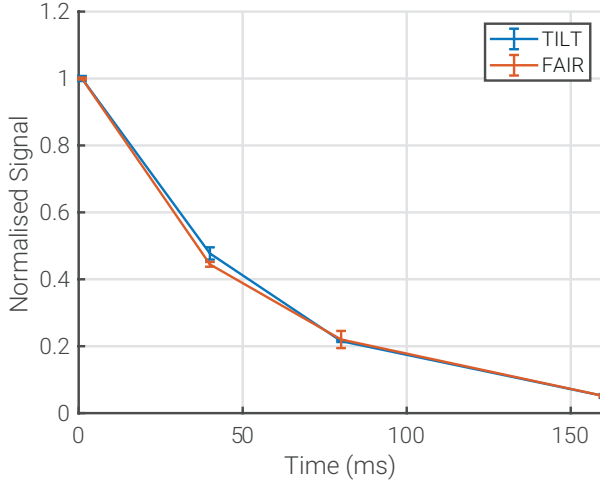


Figure 3.11: The signal decay within the superior sagittal sinus found using TRUST with both TILT and FAIR labelling sequences scaled by their initial signal intensities at eTE = 1 ms.

As can be seen these signals are in excellent agreement with the TILT sequence producing a T_2 of 52 ± 1 ms and the FAIR sequence producing a T_2 of 50 ± 2 ms, therefore in agreement within the bounds of error. This means that FAIR can be directly substituted for TILT in the TRUST sequence to measure Y_v in the superior sagittal sinus and can subsequently be used for the renal TRUST measurements.

To find the dependence PLD has upon the signal measured, scans were carried out at a range of delays from 400 ms to 1400 ms while using the FAIR labelling sequence. The signal from eTE=1 ms was then plot against label delay. Figure 3.12 shows the signal from the difference images. The maximum signal is observed with a PLD of 800 ms. This value is reached due to the balance between T_1 relaxation of the non-selective blood and inflow of unlabelled blood. This maximum in signal agrees with literature using the TILT labelling scheme [22]. By carrying out scans with this PLD the maximum SNR will be achieved.

3.3. Results and Discussion

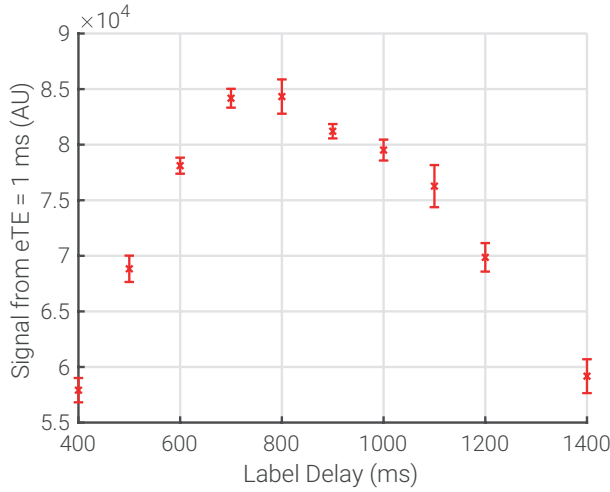


Figure 3.12: The mean signal from the first echo of each difference image over a range of PLD times.

T_2 should have no dependence upon PLD given the signal from the difference image will have the same decay in time, it will just be a lower intensity for non-optimal PLD thus leading to a larger confidence interval. To confirm this the fit values of T_2 were plotted against PLD, Figure 3.13.

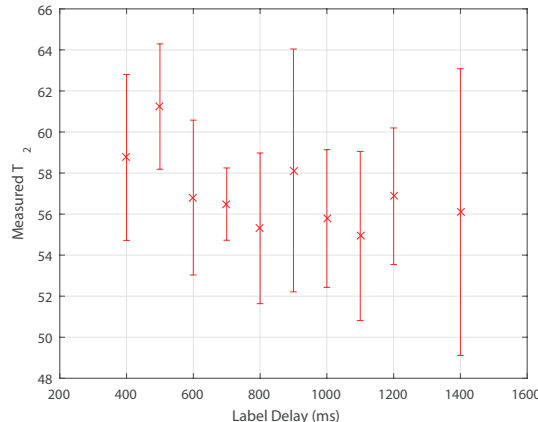


Figure 3.13: The dependence of T_2 upon PLD.

It can be seen that, as predicted, there is no relationship between T_2 and PLD. An increase in error with label delay was not observed, this effect may only show itself at larger values of PLD however for our purposes, simply confirming there is no large increase in error around our chosen PLD is sufficient. This means that if there is a variation in the optimum PLD between subjects due to the larger range in RBF compared to Cerebral Blood Flow (CBF) then this will not have an affect upon the value of T_2 and thus Y_v .

3.3. Results and Discussion

When the analysis is carried out on the images, the four brightest voxels of the difference image are averaged before the fitting occurs. This number of voxels is chosen due to the average size of the superior sagittal sinus however, for some subjects more voxels could be included, potentially yielding better results. To assess the variability in T_2 measurements with the number of voxels averaged, the analysis was run multiple times with one to twelve voxels included in the calculation. Multiple TRUST scans were performed on the same subject and averaged generating Figure 3.14a.

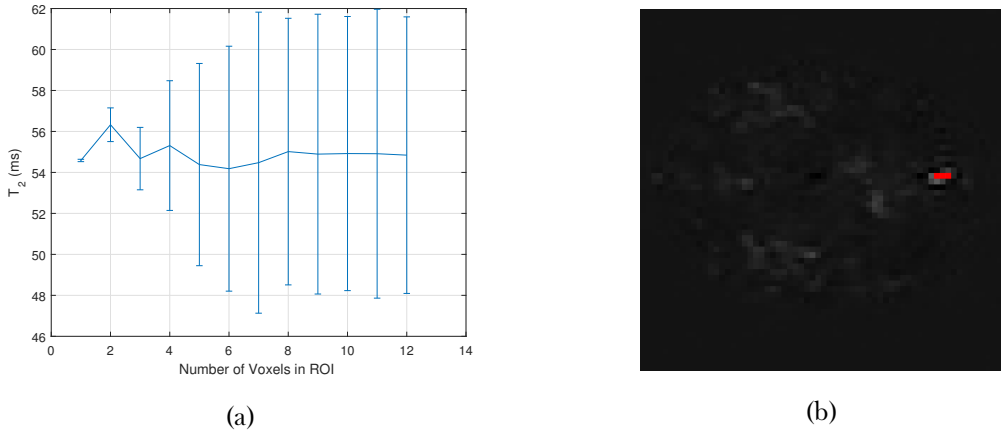


Figure 3.14: (a) The value of T_2 computed for the superior sagittal sinus with different numbers of voxels included in the calculation. (b) The difference image of the superior sagittal sinus with a three voxel ROI shown. This is already covering most of the vessel, hence the noise going up as more voxels are added to the calculation.

Although from Figure 3.14a it would appear that it would be best to only use the brightest voxel in the calculation due to its very small error and that it has the same value of T_2 as the results with far more voxels; this would not be a very robust method. It is fairly easy to conceive a greater than average level of noise being recorded on a single pixel in the relaxation and as such skewing the output of the calculation. The confidence interval is so large above six voxels because by this point the calculations are simply including the noise around the vessel rather than the signal from the blood within the sagittal sinus. Given these results, using four voxels in the calculation seems to be a reasonable balance between uncertainty and robustness.

To assess the repeatability of this measure, the optimised scan was repeated ten times on a single subject during one scanning session. This yielded a Y_v of $69.5 \pm 0.6\%$, a value consistent with literature [21, 25]. Given the success of the modified sequence on the su-

3.3. Results and Discussion

terior sagittal sinus, it was possible to attempt to measure Y_v in the renal vein.

TRUST in the Body

Ideal vessels to test the TRUST sequence within the body are the portal vein and hepatic artery as these vessels are large, have different oxygen saturations and can easily be imaged at the same time. Using the modified TRUST sequence the T_2 and oxygen saturation of the portal vein was found to be 109 ± 5 ms and 79.9 ± 0.8 % respectively; the T_2 and oxygen saturation of the hepatic artery was found to be 157 ± 10 ms and 100 ± 1 % respectively. This means that, as expected, the oxygen saturation in the hepatic artery is measured as greater than that of the portal vein and therefore the TRUST protocol is working as expected. Although normally the analysis would simply be based upon the mean of the brightest voxels in the difference image as outlined in Section 3.2.2, in Figure 3.15 a voxel by voxel analysis has been carried out for illustrative purposes.

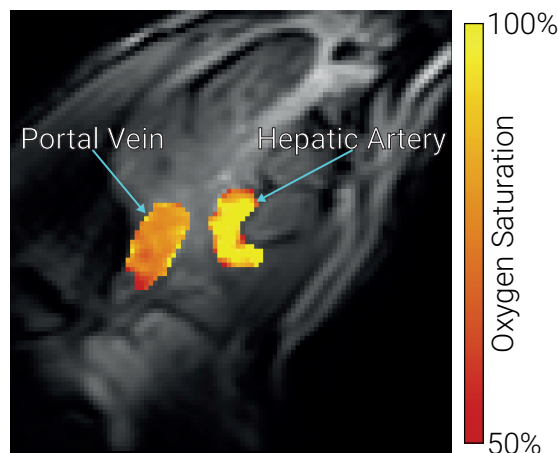


Figure 3.15: The oxygen saturation of the portal vein and hepatic artery measured using TRUST.

To assess if the PLD that generates the greatest signal is the same in the renal vein as in the superior sagittal sinus, a series of scans were collected with PLD ranging from 400 ms to 1400 ms and the signal from $eTE = 1$ ms recorded.

3.3. Results and Discussion

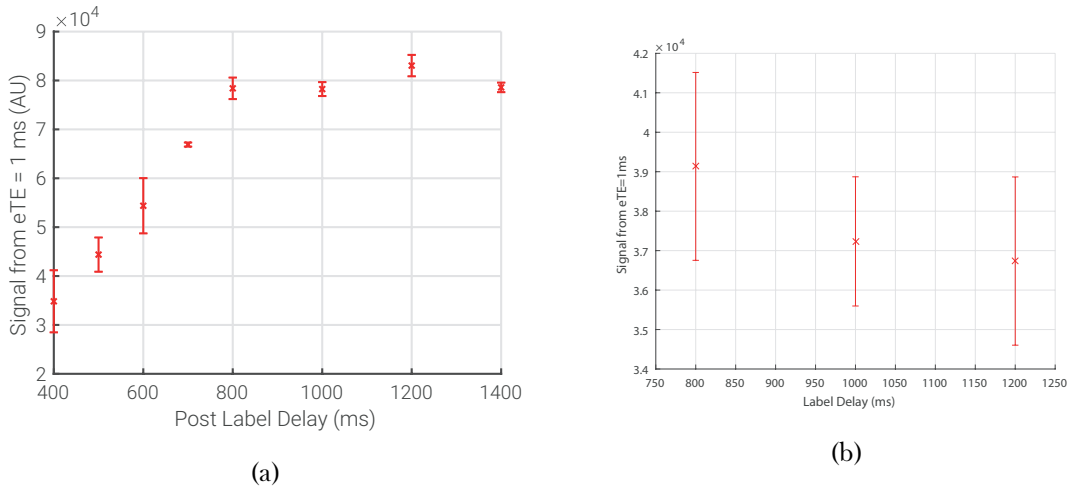


Figure 3.16: (a) The mean signal from the first echo of each difference image of the renal vein over a range of PLD. (b) Mean signal from the first echo versus PLD from a different subject.

As seen in Figure 3.16a the PLD producing the largest signal in the difference image of the renal vein is indeed different to that of the superior sagittal sinus. This is most likely due to differences in blood flow through each of these vessels, 413 ± 136 ml/min in the renal vein [14] and 285 ± 19 ml/min in the superior sagittal sinus [17]. Given the much larger uncertainty in blood flow in the renal vein, a different subject was scanned over a smaller range of PLD to ascertain if the PLD delivering the maximum signal varies much between subjects, Figure 3.16b.

The maximum signal for the first subject was achieved at a PLD of 1200 ms whereas for the second subject the maximum is at a PLD of 800 ms. Given that these subjects had a RBF either side of the mean and that there is little dependence of T_2 upon PLD it seems appropriate to use a PLD of 1000 ms for optimum signal in most subjects.

Given the larger size of the renal vein compared to the superior sagittal sinus, it would be better to include more voxels in the calculations when fitting to find a value of T_2 . Multiple scans were completed on a single subject and the value of T_2 found for each using one to twelve voxels in the fitting process. The results were averaged and plot in Figure 3.17a.

3.3. Results and Discussion

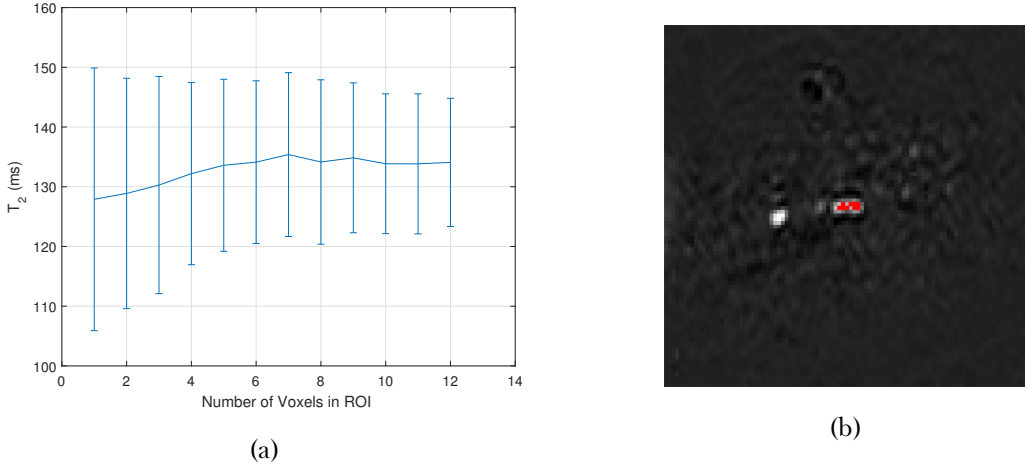


Figure 3.17: (a) The value of T_2 calculated for the renal vein with different numbers of voxels included in the calculation. (b) The difference image of the renal vein with a nine voxel ROI shown.

Unlike the results when this process was carried out on the superior sagittal sinus in Figure 3.14a, here the error decreases as more voxels are added to the calculation. This uncertainty comes from the large variation in T_2 for one voxel rather than a large error on the fit i.e. the error is coming from the differences between scans rather than the robustness of each scans results, this is precisely the concern that was raised with using a single voxel when discussing the superior sagittal sinus. As more voxels are added the error decreases until approximately six voxels are included, at this point the value of T_2 stops increasing and stays approximately constant. Once again, given the large variation in renal veins, it would be advisable to include slightly more than six voxels but not so many that in the cases of small vessels the algorithm is sampling surrounding tissue. Nine voxels seems to be a suitable middle ground as to work effectively with both small and large vessels.

To assess the repeatability of the measurements within the kidney, the same scan was repeated ten times in a single session with the optimised renal parameters. This yielded a T_2 of 135 ± 5 ms corresponding to a Y_v of $89 \pm 2\%$. The variation in measurements of Y_v in the renal vein are relatively substantial and show no dependence upon time so are therefore not likely due to physiological changes. The value of Y_v in the renal vein is much higher than in the sagittal sinus however is within the range found by Nielsen [49].

3.3. Results and Discussion

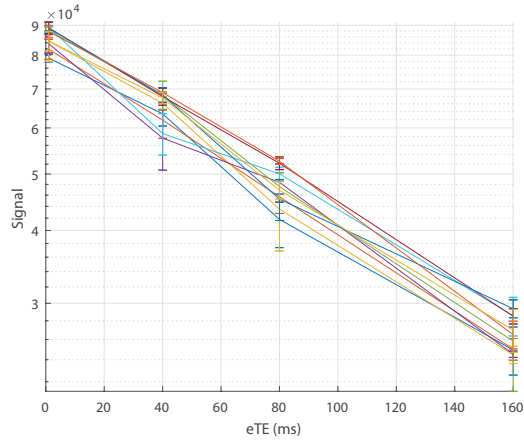


Figure 3.18: The T_2 relaxation curves of ten scans repeated on a single subject.

To compare the abilities of BOLD T_2^* maps and TRUST to measure changes in oxygenation in the kidneys, a hyperoxia challenge was conducted. In Figure 3.19a, no systematic, bulk change in T_2^* can be seen indicating that the change in T_2^* caused by the introduction of pure oxygen is dominated by other confounding factors. This is confirmed when ROI are defined for the renal cortex and renal medulla with the mean change in T_2^* found to be -2 ± 8 ms and -1 ± 6 ms respectively. When TRUST is used to measure the oxygen saturation in the renal vein an increase of 16 ± 3 % is observed, Figure 3.19b. This shows that it is possible to measure changes in renal oxygenation using TRUST that would be undetectable using the current standard, BOLD T_2^* mapping.

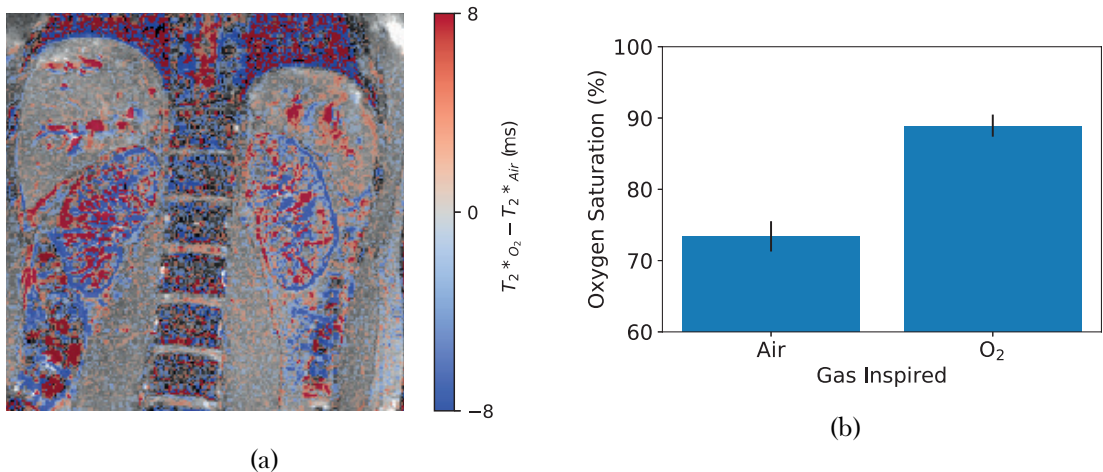


Figure 3.19: (a), The difference in T_2^* measured between baseline and the hyperoxia state. (b) The difference in Y_v measured using TRUST.

3.4 Conclusions and Future Work

This work shows promising results for the use of a modified TRUST sequence to measure oxygenation of blood within the body. The existing TRUST sequence was modified to be respiratory triggered and use the FAIR labelling scheme making it suitable for use in the body. Once these modifications had been carried out, parameters such as PLD and the number of voxels used in the ROI were optimised. The ability of TRUST to measure a change in renal oxygenation was successfully verified via a hyperoxia challenge which was able to measure an increase of $16 \pm 3\%$ where the current standard measurement of renal oxygenation, BOLD T_2^* maps, recorded no significant change.

Looking forward this work could be expanded by carrying out the hyperoxia challenge on more subjects. Although a small number of measurements were gathered on the hepatic vessels, further work could be undertaken to compare the use of susceptibility based oximetry and TRUST to measure oxygenation in the portal vein in response to a hyperoxia challenge as conducted for the kidneys here. In the current protocol, haematocrit is assumed to be an average value of 0.41 unless a blood test has recently been undertaken. As stated above, there is a correlation between T_1 of blood and its haematocrit, this means that a measurement of the subjects haematocrit could be taken while they are in the scanner, thus leading to a more accurate measurement of oxygenation with only a small increase in scan time.

3.5 Acknowledgements

We thank Hanzhang Lu for sharing the TRUST methodology.

3.6 References

1. Daniel, A., Cox, E., Buchanan, C., Bradley, C. & Francis, S. *Applying T2 Relaxation Under Spin Tagging (TRUST) to Assess Renal Oxygenation in the Kidney* in *Proc. Intl. Soc. Mag. Reson. Med.* 26 International Society of Magnetic Resonance in Medicine Annual Meeting (Paris, 21st July 2018).
2. Stevens, L. A., Coresh, J., Greene, T. & Levey, A. S. Assessing Kidney Function — Measured and Estimated Glomerular Filtration Rate. *New England Journal of Medicine* **354**, 2473–2483. issn: 0028-4793 (8th June 2006).
3. Farrugia, A. Albumin Usage in Clinical Medicine: Tradition or Therapeutic? *Transfusion Medicine Reviews* **24**, 53–63. issn: 0887-7963, 1532-9496 (1st Jan. 2010).
4. Pruijm, M., Milani, B. & Burnier, M. Blood Oxygenation Level-Dependent MRI to Assess Renal Oxygenation in Renal Diseases: Progresses and Challenges. *Frontiers in Physiology* **7**. issn: 1664-042X. pmid: 28105019 (5th Jan. 2017).
5. Coresh, J., Astor, B. C., Greene, T., Eknayan, G. & Levey, A. S. Prevalence of Chronic Kidney Disease and Decreased Kidney Function in the Adult US Population: Third National Health and Nutrition Examination Survey. *American Journal of Kidney Diseases: The Official Journal of the National Kidney Foundation* **41**, 1–12. issn: 1523-6838 (Jan. 2003).
6. De Lusignan, S. *et al.* Identifying Patients with Chronic Kidney Disease from General Practice Computer Records. *Family Practice* **22**, 234–241. issn: 0263-2136 (1st June 2005).
7. Drey, N., Roderick, P., Mullee, M. & Rogerson, M. A Population-Based Study of the Incidence and Outcomes of Diagnosed Chronic Kidney Disease. *American Journal of Kidney Diseases* **42**, 677–684. issn: 0272-6386 (1st Oct. 2003).
8. Amato, D. *et al.* Prevalence of Chronic Kidney Disease in an Urban Mexican Population. *Kidney International* **68**, S11–S17. issn: 0085-2538 (1st Aug. 2005).
9. Chadban, S. J. *et al.* Prevalence of Kidney Damage in Australian Adults: The Aus-Diab Kidney Study. *Journal of the American Society of Nephrology* **14**, S131–S138. issn: 1046-6673, 1533-8450 (suppl 2 1st July 2003).
10. Jungers, P. *et al.* Late Referral to Maintenance Dialysis: Detrimental Consequences. *Nephrology Dialysis Transplantation* **8**, 1089–1093. issn: 0931-0509 (1st Jan. 1993).

3.6. References

11. Sesso, R. & Belasco, A. G. Late Diagnosis of Chronic Renal Failure and Mortality on Maintenance Dialysis. *Nephrology Dialysis Transplantation* **11**, 2417–2420. ISSN: 0931-0509 (1st Dec. 1996).
12. Klebe, B. *et al.* The Cost of Implementing UK Guidelines for the Management of Chronic Kidney Disease. *Nephrology Dialysis Transplantation* **22**, 2504–2512. ISSN: 0931-0509 (1st Sept. 2007).
13. Precious, K. NHS England » Programme Budgeting <https://www.england.nhs.uk/resources/resources-for-ccgs/prog-budgeting/> (2017).
14. Cox, E. F. *et al.* Multiparametric Renal Magnetic Resonance Imaging: Validation, Interventions, and Alterations in Chronic Kidney Disease. *Frontiers in Physiology* **8**. ISSN: 1664-042X (2017).
15. Niendorf, T. *et al.* How Bold Is Blood Oxygenation Level-Dependent (BOLD) Magnetic Resonance Imaging of the Kidney? Opportunities, Challenges and Future Directions. *Acta Physiologica* **213**, 19–38. ISSN: 1748-1716.
16. Chong, S. P., Merkle, C. W., Leahy, C. & Srinivasan, V. J. Cerebral Metabolic Rate of Oxygen (CMRO₂) Assessed by Combined Doppler and Spectroscopic OCT. *Bio-medical Optics Express* **6**, 3941–3951. ISSN: 2156-7085 (11th Sept. 2015).
17. Jordan, J. E., Pelc, N. J. & Enzmann, D. R. Velocity and Flow Quantitation in the Superior Sagittal Sinus with Ungated and Cine (Gated) Phase-Contrast MR Imaging. *Journal of Magnetic Resonance Imaging* **4**, 25–28. ISSN: 1522-2586 (1st Jan. 1994).
18. Miao, G. *et al.* Reference Value of Presenile Human Hematocrit and Geographical Factors. *Journal of Clinical Laboratory Analysis* **16**, 26–29. ISSN: 1098-2825 (1st Jan. 2002).
19. Gardener, A. G., Francis, S. T., Prior, M., Peters, A. & Gowland, P. A. Dependence of Blood R₂ Relaxivity on CPMG Echo-Spacing at 2.35 and 7 T. *Magnetic Resonance in Medicine* **64**, 967–974. ISSN: 1522-2594 (1st Oct. 2010).
20. Shimada, K., Nagasaka, T., Shidahara, M., Machida, Y. & Tamura, H. In Vivo Measurement of Longitudinal Relaxation Time of Human Blood by Inversion-Recovery Fast Gradient-Echo MR Imaging at 3T. *Magnetic resonance in medical sciences: MRMS: an official journal of Japan Society of Magnetic Resonance in Medicine* **11**, 265–271. ISSN: 1880-2206 (2012).

3.6. References

21. Nagdyman, N. *et al.* Comparison between Cerebral Tissue Oxygenation Index Measured by Near-Infrared Spectroscopy and Venous Jugular Bulb Saturation in Children. *Intensive Care Medicine* **31**, 846–850. ISSN: 0342-4642, 1432-1238 (1st June 2005).
22. Lu, H. & Ge, Y. Quantitative Evaluation of Oxygenation in Venous Vessels Using T2-Relaxation-Under-Spin-Tagging MRI. *Magnetic Resonance in Medicine* **60**, 357–363. ISSN: 1522-2594 (1st Aug. 2008).
23. Xu, F., Uh, J., Liu, P. & Lu, H. On Improving the Speed and Reliability of T2-Relaxation-Under-Spin-Tagging (TRUST) MRI. *Magnetic Resonance in Medicine* **68**, 198–204. ISSN: 0740-3194 (July 2012).
24. Liu, P., Xu, F. & Lu, H. Test–Retest Reproducibility of a Rapid Method to Measure Brain Oxygen Metabolism. *Magnetic Resonance in Medicine* **69**, 675–681. ISSN: 1522-2594 (1st Mar. 2013).
25. Liu, P. *et al.* Multi-Site Evaluations of a T2-Relaxation-Under-Spin-Tagging (TRUST) MRI Technique to Measure Brain Oxygenation. *Magnetic resonance in medicine* **75**, 680–687. ISSN: 0740-3194 (Feb. 2016).
26. Jain, V., Langham, M. C. & Wehrli, F. W. MRI Estimation of Global Brain Oxygen Consumption Rate. *Journal of Cerebral Blood Flow & Metabolism* **30**, 1598–1607. ISSN: 0271-678X (1st Sept. 2010).
27. Jain, V. *et al.* Cerebral Oxygen Metabolism in Neonates with Congenital Heart Disease Quantified by MRI and Optics. *Journal of Cerebral Blood Flow & Metabolism* **34**, 380–388. ISSN: 0271-678X (1st Mar. 2014).
28. Driver, I. D. *et al.* Global Intravascular and Local Hyperoxia Contrast Phase-Based Blood Oxygenation Measurements. *NeuroImage* **101**, 458–465. ISSN: 1053-8119 (1st Nov. 2014).
29. Lee, H., Langham, M. C., Rodriguez-Soto, A. E. & Wehrli, F. W. Multiplexed MRI Methods for Rapid Estimation of Global Cerebral Metabolic Rate of Oxygen Consumption. *NeuroImage* **149**, 398–403. ISSN: 1053-8119 (1st Apr. 2017).
30. Wright, G. A., Hu, B. S. & Macovski, A. Estimating Oxygen Saturation of Blood in Vivo with MR Imaging at 1.5 T. *Journal of Magnetic Resonance Imaging* **1**, 275–283. ISSN: 1522-2586 (1st May 1991).

3.6. References

31. Haacke, E. M. *et al.* In Vivo Measurement of Blood Oxygen Saturation Using Magnetic Resonance Imaging: A Direct Validation of the Blood Oxygen Level-Dependent Concept in Functional Brain Imaging. *Human Brain Mapping* **5**, 341–346. issn: 1097-0193 (1st Jan. 1997).
32. Spees, W. M., Yablonskiy, D. A., Oswood, M. C. & Ackerman, J. J. Water Proton MR Properties of Human Blood at 1.5 Tesla: Magnetic Susceptibility, T1, T2, T*2, and Non-Lorentzian Signal Behavior. *Magnetic Resonance in Medicine* **45**, 533–542. issn: 1522-2594 (1st Apr. 2001).
33. Jain, V., Abdulmalik, O., Propert, K. J. & Wehrli, F. W. Investigating the Magnetic Susceptibility Properties of Fresh Human Blood for Noninvasive Oxygen Saturation Quantification. *Magnetic Resonance in Medicine* **68**, 863–867. issn: 1522-2594 (1st Sept. 2012).
34. Jenkinson, M. Fast, Automated, N-Dimensional Phase-Unwrapping Algorithm. *Magnetic Resonance in Medicine* **49**, 193–197. issn: 1522-2594 (1st Jan. 2003).
35. Hendrikse, J., Lu, H., van der Grond, J., van Zijl, P. C. & Golay, X. Measurements of Cerebral Perfusion and Arterial Hemodynamics during Visual Stimulation Using TURBO-TILT. *Magnetic Resonance in Medicine* **50**, 429–433. issn: 1522-2594 (1st Aug. 2003).
36. Golay, X., Petersen, E. T. & Hui, F. Pulsed Star Labeling of Arterial Regions (PULSAR): A Robust Regional Perfusion Technique for High Field Imaging. *Magnetic Resonance in Medicine* **53**, 15–21. issn: 1522-2594 (1st Jan. 2005).
37. Golay, X., Stuber, M., Pruessmann, K. P., Meier, D. & Boesiger, P. Transfer Insensitive Labeling Technique (TILT): Application to Multislice Functional Perfusion Imaging. *Journal of Magnetic Resonance Imaging* **9**, 454–461. issn: 1522-2586 (1st Mar. 1999).
38. Lu, H., Clingman, C., Golay, X. & van Zijl, P. C. Determining the Longitudinal Relaxation Time (T1) of Blood at 3.0 Tesla. *Magnetic Resonance in Medicine* **52**, 679–682. issn: 1522-2594 (1st Sept. 2004).
39. Silvennoinen, M., Clingman, C., Golay, X., Kauppinen, R. & van Zijl, P. Comparison of the Dependence of Blood R2 and R2* on Oxygen Saturation at 1.5 and 4.7 Tesla. *Magnetic Resonance in Medicine* **49**, 47–60. issn: 1522-2594 (1st Jan. 2003).

3.6. References

40. Liu, P. *et al.* T1 and T2 Values of Human Neonatal Blood at 3 Tesla: Dependence on Hematocrit, Oxygenation, and Temperature. *Magnetic Resonance in Medicine* **75**, 1730–1735. issn: 1522-2594 (Apr. 2016).
41. Lu, H. *et al.* Calibration and Validation of TRUST MRI for the Estimation of Cerebral Blood Oxygenation. *Magnetic Resonance in Medicine* **67**, 42–49. issn: 1522-2594 (1st Jan. 2012).
42. Martirosian, P., Klose, U., Mader, I. & Schick, F. FAIR True-FISP Perfusion Imaging of the Kidneys. *Magnetic Resonance in Medicine* **51**, 358–361. issn: 1522-2594 (1st Feb. 2004).
43. Liu, P., Cox, E. & Daniel, A. *Pro TRUST* version V2018.5. 23rd Aug. 2011.
44. O'Connor, J. P. *et al.* Comparison of Normal Tissue R1 and R*2 Modulation by Oxygen and Carbogen. *Magnetic Resonance in Medicine* **61**, 75–83. issn: 1522-2594 (1st Jan. 2009).
45. Donati, O. F., Nanz, D., Serra, A. L. & Boss, A. Quantitative BOLD Response of the Renal Medulla to Hyperoxic Challenge at 1.5 T and 3.0 T. *NMR in Biomedicine* **25**, 1133–1138. issn: 1099-1492 (1st Oct. 2012).
46. Pruijm, M. *et al.* Effect of Sodium Loading/Depletion on Renal Oxygenation in Young Normotensive and Hypertensive Men. *Hypertension* **55**, 1116–1122. issn: 0194-911X, 1524-4563 (1st May 2010).
47. Tumkur, S. M., Vu, A. T., Li, L. P., Pierchala, L. & Prasad, P. V. Evaluation of Intra-Renal Oxygenation during Water Diuresis: A Time-Resolved Study Using BOLD MRI. *Kidney International* **70**, 139–143. issn: 0085-2538 (1st July 2006).
48. Prasad, P. V. & Epstein, F. H. Changes in Renal Medullary pO₂ during Water Diuresis as Evaluated by Blood Oxygenation Level-Dependent Magnetic Resonance Imaging: Effects of Aging and Cyclooxygenase Inhibition. *Kidney International* **55**, 294–298. issn: 0085-2538 (1st Jan. 1999).
49. Nielsen, K., Rehling, M. & Henriksen, J. H. Renal Vein Oxygen Saturation in Renal Artery Stenosis. *Clinical Physiology* **12**, 179–184. issn: 1365-2281 (1st Mar. 1992).

Chapter 4

Automated Segmentation of Kidneys using Machine Learning

Abstract

This work was presented as an aural presentation at the ISMRM 28th Annual Meeting (2020) [1].

Lorem ipsum dolor sit amet, consectetuer adipiscing elit. Ut purus elit, vestibulum ut, placerat ac, adipiscing vitae, felis. Curabitur dictum gravida mauris. Nam arcu libero, nonummy eget, consectetuer id, vulputate a, magna. Donec vehicula augue eu neque. Pellentesque habitant morbi tristique senectus et netus et malesuada fames ac turpis egestas. Mauris ut leo. Cras viverra metus rhoncus sem. Nulla et lectus vestibulum urna fringilla ultrices. Phasellus eu tellus sit amet tortor gravida placerat. Integer sapien est, iaculis in, pretium quis, viverra ac, nunc. Praesent eget sem vel leo ultrices bibendum. Aenean faucibus. Morbi dolor nulla, malesuada eu, pulvinar at, mollis ac, nulla. Curabitur auctor semper nulla. Donec varius orci eget risus. Duis nibh mi, congue eu, accumsan eleifend, sagittis quis, diam. Duis eget orci sit amet orci dignissim rutrum.

4.1 Introduction

Segmentation of the kidneys in MRI images is a vital, yet time consuming, aspect of many renal studies [2–4]. Total Kidney Volume (TKV) is used as a biomarker for a variety of renal pathologies; autosomal dominant polycystic disease is characterised by an increase in TKV [5, 6], while a decrease in TKV is associated with a decrease in renal function [7]. In addition to TKV measurements, renal segmentation is an important first step for many other processing pipelines, be that to increase accuracy of automated cortical-medullary segmentations or reduce computation times by only carrying out calculations for a relevant ROI. The gold standard of segmentation is manual ROI definition by an experienced and skilled professional, this manual process is highly time consuming and difficult due to similar signal intensities between the kidneys and other organs, anatomical differences between subjects and imaging artefacts. These factors mean that developing a fully automated method of renal segmentation is highly desirable. Such methods have been proposed with varied successes [8, 9] however the techniques used differ between diseases. The fact that each technique is highly optimised for a specific dataset means that it needs to be re-written to be applied to different a pathology, another time consuming and highly skilled process.

Machine learning allows for a single method to be written and then trained on different datasets. This means that as more data becomes available the algorithm can become more accurate and generalised, without a need to rewrite the methods, thus making it a better choice for long term development. Such methods have already been applied to segmentation in other areas of medical imaging, especially successful have been U-Nets. An example of a FCN! (FCN!), these algorithms convolve the image with a series of filters to extract features from the input data and thus generate a voxel by voxel classification. The weights of each pixel in these convolution kernels is honed through an optimisation process where the filters are applied to the training data and their performance is evaluated against the manually segmented data using a loss function such as mean square error or dice overlap score. Changes to each filter are then back propagated through the network and the process starts again. After many iterations, the filters become tuned to detecting the feature labelled in the manually segmented data.

To avoid the network becoming too specific and, for example, just learning to detect the specific kidneys in the data the network has been trained on rather than all kidneys, the data

4.1. Introduction

is divided into three categories, training, testing and validation. The training data is used for adjusting the filter weights over a short time scale, usually after a few tens of images. Once all the training data has been processed by the network and filter weights adjusted, all the test data is run through the network without any further weight adjustments and the performance evaluated using the loss function, this train, test cycle is known as an epoch. If the network has become too specialised and finely adjusted to the training data then it will not perform well on the test data. To stop this over specialisation, or over-fitting, the weights used at the start of each epoch are those that delivered the best performance on the test data. The validation data is never used to influence the filter weights and is used to validate the performance of the network on unseen data.

Similar methods have been applied to segment other areas of anatomy [10, 11], however this has not been successfully applied to segment the kidneys. Here we propose a FCN! to segment the kidneys from a standardised MRI protocol.

4.2 Methods

4.2.1 Data Acquisition

All data is acquired on a 3T Philips Ingenia system using a T_2 -weighted HASTE sequence (TE = 60, TR = 1800 or 1300 ms, FOV = $350 \times 350 \text{ mm}^2$, voxel size = $1.46 \times 1.46 \times 5 \text{ mm}^3$ with enough slices to cover the entire kidney, usually 12-14, SENSE = 2.5), the sequence is carried out in a single breath hold. Parameters have been optimised to deliver the maximum contrast between the kidneys and surrounding tissue. Training and test data is a single volume per subject; validation datasets are composed of five volumes acquired on the same subject in the same scanning session with the subject being removed from the scanner, asked to move, then positioned back in the scanner between each acquisition. The scanner operator attempted to vary the acquisition geometry between repeats while still acquiring the full kidney volume. These validation datasets allow the consistency of the networks ability to measure TKV to be assessed. Manual binary masks are generated for every volume to allow the network to train and its accuracy to be investigated. A summary of the data collected can be seen in Table 4.1, to make the algorithm as generalisable as possible, healthy volunteers and patients with CKD are scanned.

Dataset	Number of Subjects	Number of Volumes
Healthy kidneys	26	26
CKD kidneys	23	23
Validation healthy kidneys	5	25
Validation CKD kidneys	3	15

Table 4.1: Number of subjects and volumes in each dataset type.

The accuracy of the network will increase as it is trained on a greater volume of data. As such, this protocol is still being run on as many subjects as possible to further increase the accuracy of the algorithm.

4.2.2 Data Pre-Processing

All training and test data is loaded and the order of the volumes randomised i.e. healthy volunteers and patients are mixed. Each slice is resampled to a matrix size of 256×256 and voxel intensities scaled between 0 and 1 where black is set to the mean voxel value minus 0.5 times the standard deviation of that slice and white is set to the mean voxel value plus 4 times the standard deviation of the slice; values outside this range are clipped to 0 or

4.2. Methods

1. This windowing leads to a clear contrast between kidneys and surrounding tissue while negating the effects of bulk signal changes between subjects.

This resampling and windowing is also applied to the validation data before it is processed by the network. Once a prediction of the renal mask has been generated by the algorithm, the mask is resampled back to the original image volume dimensions.

The ratio of training data to test data is eighty to twenty. No data augmentation is performed in this architecture.

4.2.3 Network Architecture

A summary of the network architecture is shown in Figure 4.1. Each volume is split into two-dimensional slices before being processed by the network. Convolution and deconvolution layers use a 3×3 kernel. Activation layers use a Rectified Linear Unit (ReLU). Max pooling with a stride 2 is used on the encoding half of the network.

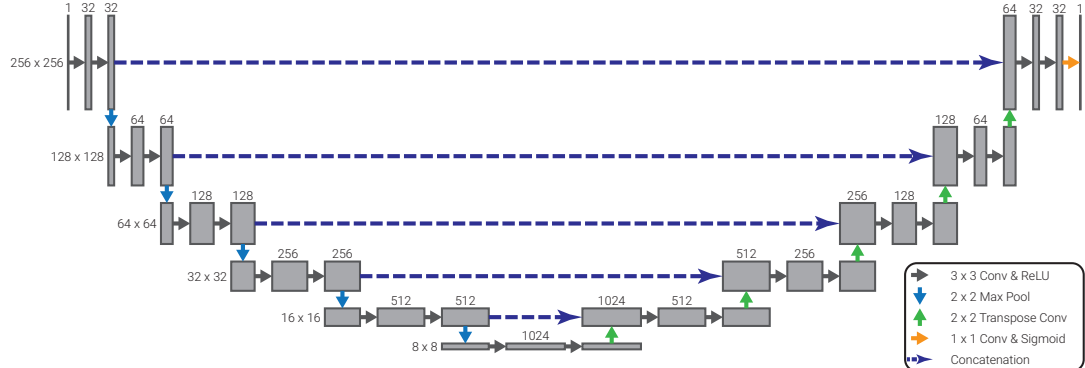


Figure 4.1: The architecture of the network used.

The network uses a dice score, defined by Equation (4.1), as its loss function; this function is ideal for renal segmentation as it doesn't weight true negatives which represent the majority of voxels input to the network. Training is carried out over 150 epochs using stochastic gradient decent with a learning rate of 0.01 to optimise the networks approximately thirty million trainable parameters.

$$D(A, B) = \frac{2|A \cap B|}{|A| + |B|} \quad (4.1)$$

The network is implemented using Keras [12] with a TensorFlow [13, 14] back-end and is trained on an NVIDIA Titan Xp Graphical Processing Unit (GPU). Training takes approx-

4.2. Methods

imately forty minutes for the 150 epochs and predicting a renal mask from a thirteen slice volume takes approximately 9 seconds when executed on a computer with no GPU (as it would be in most end user cases).

4.3 Results and Discussion

Initial data was collected with a TR of 1800 ms leading to a breath hold of approximately 23 seconds. Some subjects struggled to hold their breath for this long on expiration, therefore the effects of reducing the TR of the sequence were investigated. As can be seen in Figure 4.2, there is no degradation in image quality from the image with TR or 1800 ms to that with at TR of 1300 ms, the differences between these images are mainly due to the small movements between volumes, as can be seen in the difference data where the largest differences are seen around the periphery of the kidneys and in the gut. Moving forward, the TR was reduced to 1300 ms leading to a sequence with a breath hold of approximately 17 seconds.

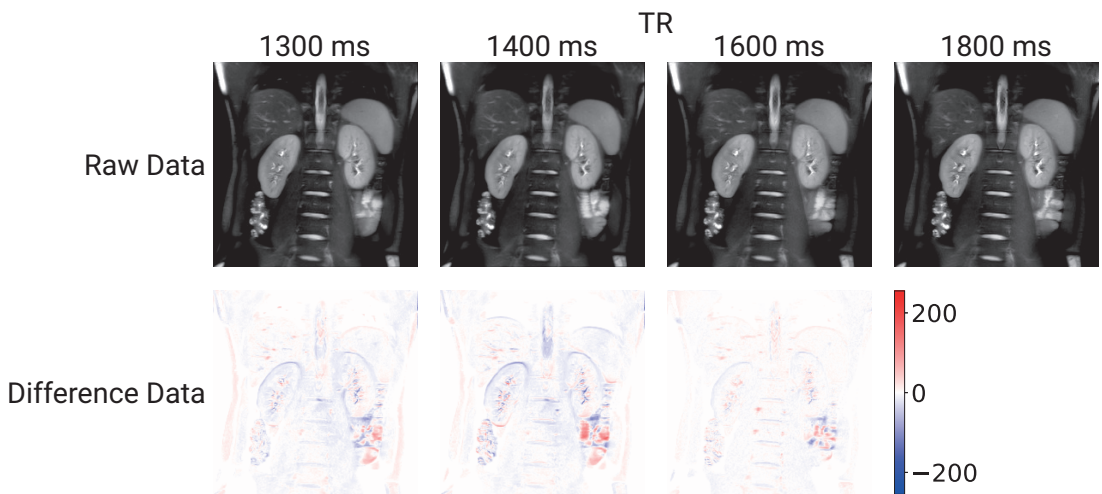


Figure 4.2: The effects of changing the TR of the sequence.

To verify that the trained network is behaving as expected saliency maps were produced, Figure 4.3, this is especially important given the black box nature of machine learning methods. This map shows the areas the network is using most in its classification [15]. It verifies that the networks is using the outside areas of the kidney to make its prediction with areas of a similar intensity receiving some attention to distinguish them from the kidney. While this is precisely what is expected of the algorithm, it is important to check this as it is possible for such a method to have learnt a slightly different mechanism for the segmentation, one that is more prone to errors if new data is presented to it.

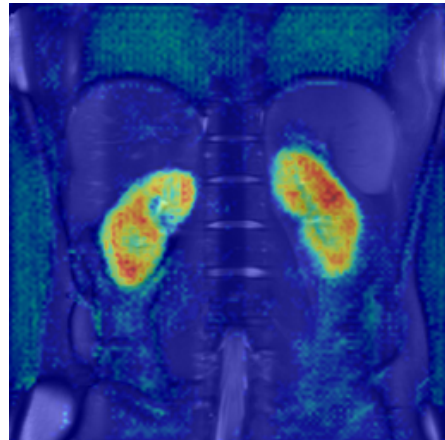


Figure 4.8: An example saliency map of the areas the network uses most when segmenting the kidney.

To assess the accuracy of the network, each of the five volumes per validation subject was segmented by the trained network, in theory the TKV predicted for each volume should have been the same. Figure 4.4a shows the predicted TKV against the manually segmented “true” TKV with each subject plot in a different colour. While there is a spread in the predicted values, there is also a reasonable variation in manual TKV. For three out of the seven repeatability subjects, the predicted TKV has a smaller standard deviation than the manually segmented data, this indicates that the algorithm may actually be more consistent than the humans. To identify if a systematic error is present, a Bland-Altman plot was generated (Figure 4.4b). From this figure it is possible to see that the algorithm is slightly over estimating the TKV by 0.69% (1.6 mm^3) but there is no correlation between difference in TKV and true TKV over all subjects. There is a more subtle trend between each repeat on the same subject though, the volumes with a smaller true TKV are consistently over estimated more than those volumes with a larger true TKV. This again points to an issue with the manual segmentation rather than the algorithm.

4.3. Results and Discussion

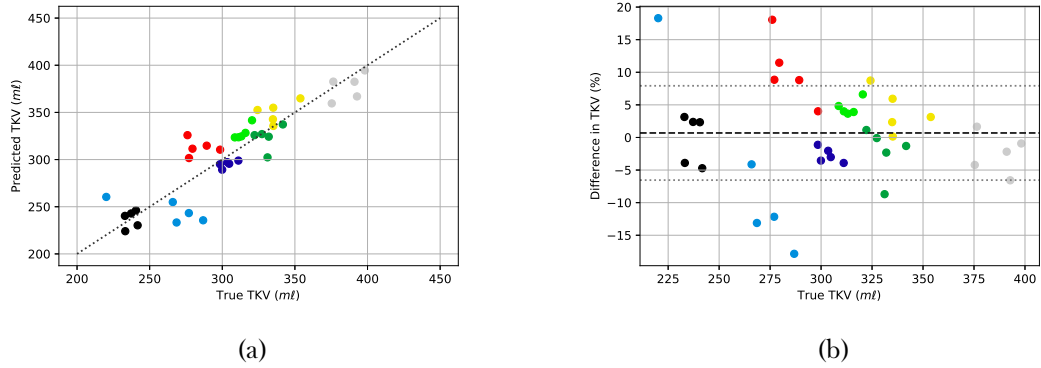


Figure 4.4: (a) The predicted TKV plot against the manually segmented “true” TKV. Each subject is plotted in a different colour. (b) A Bland-Altman plot to identify and systematic error in the networks performance. Each subject is plotted in a different colour.

While assessing the ability of the algorithm to predict TKV is important, it is also necessary to assess the raw segmentation as, for example, the algorithm may be over-estimating the size of central slices but under-estimating the size of edge slices. This type of inaccuracy could be masked in the TKV however will be visible in the dice scores. These are shown in Figure 4.5.

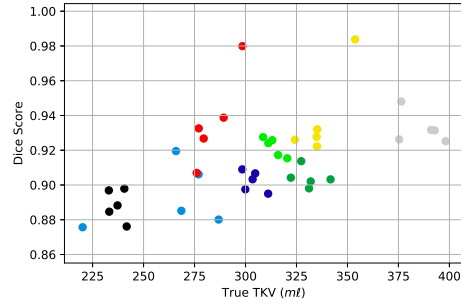


Figure 4.5: The dice scores for all volumes in the validation data. Each subject is plotted in a different colour.

The mean dice score over all forty volumes is 0.91 ± 0.02 . Here we see a slight trend towards more accurate predictions for larger kidneys. The reason for this becomes clear when we look at the ROI the algorithm is outputting, Figure 4.6.

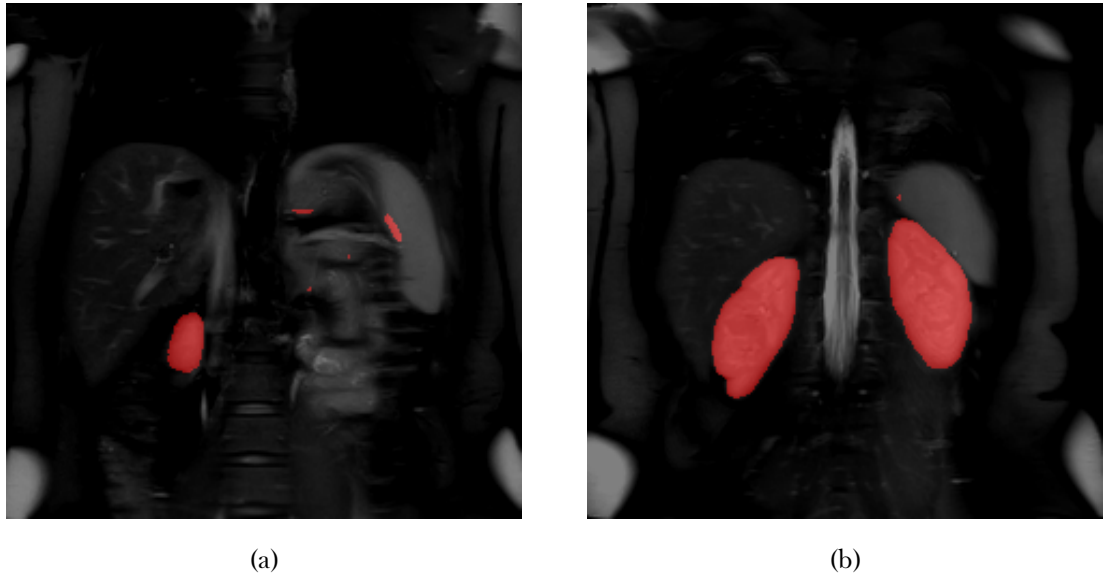


Figure 4.6: (a) A slice from the posterior of the volume. (b) A slice from the centre of the kidneys.

In Figure 4.6a the algorithm is assigning false positives on the right hand side of the image in the area a kidney would be expected further into the body. The amount of false positives decrease as the slices move in an anterior direction as kidney comes into the slice, 4.6b. The algorithm works on each slice individually as a two-dimensional image rather than as a three-dimensional volume. This means that, as the majority of slices in the training data have two kidneys in them, the algorithm is more likely to generate false positives if there is no kidney in the slice. For smaller kidneys, there are more slices with no kidney in them and therefore the overall dice score is lower, hence the trend observed in Figure 4.5.

There are multiple methods of reducing this tendency in the algorithm. The false positives tend to be spatially independent through slices, this means that it would be relatively simple to remove them in post-processing by reconstructing the two-dimensional slices back into a three-dimensional volume and removing masked areas with a small volume or areas that are very thin in the anterior-posterior direction. Another method would be to modify the architecture to a Recursive Neural Network (RNN) with Long Short-Term Memory (LSTM). This would also keep the large advantage of working with two-dimensional images, that the algorithm generalises to n slices, but means that the algorithm also has some memory of what is in the surrounding slices [16, 17]. Finally the algorithm could be re-written as a three-dimensional FCN!, this would give the greatest degree of accuracy between slices however comes at the expense of simple generalisation with regards

4.3. Results and Discussion

to number of slices or the slice thickness and would require much more data collection as amount of training/test data would be reduced by a factor of approximately thirteen.

To establish how the network is performing with the relatively small amount of training data, predictions were made on the training and testing data and the dice score plot, Figure 4.7.

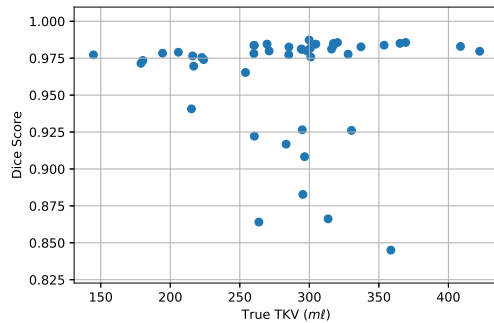


Figure 4.7: The dice score of predictions made on the training data.

The algorithm is performing better on most of the training data than it did on the validation data although with 80% of the volumes segmented more accurately than the validation data. This indicates that a certain degree of over fitting is occurring as the 20% of volumes that are not segmented as well are most likely the testing data. Earlier in the development of this network it was established that augmentation did not improve the performance of the trained network however this should be explored again in light of this result as some basic augmentation would lead to a smaller disparity between the training data and test data and thus allow for better performance when segmenting the validation data.

An indication that some degree of data augmentation would be beneficial is also seen when investigating if there is any difference in performance of the network between healthy and CKD kidneys. The manually segmented mean TKV of the healthy subjects is 330 ± 35 ml and for subjects with CKD is 268 ± 32 ml therefore it would be expected that the algorithm would perform better on the healthy subjects given their larger kidney volume. This is not the case though, the mean dice score of the validation images for healthy kidneys is 0.89 ± 0.02 and for kidneys with CKD this increases to 0.93 ± 0.02 . As there are more healthy subjects in the training data (26 versus 23) it would be expected that the network would perform better for these subjects however the greater degree of variability in geometry and size of the CKD kidneys means they essentially have some degree of

4.3. Results and Discussion

augmentation built into them. If this were replicated via data augmentation in the whole training dataset then an increase in accuracy across the board may be observed.

4.4 Conclusions and Future Work

This method has been shown to produce promising results delivering an mean dice score of 0.91 ± 0.02 over eight unseen scans with a mixture of healthy and CKD subjects resulting in a mean TKV difference of 0.69% when compared to the manually segmented TKV. This is especially promising as the algorithm will improve in accuracy as more training data is collected, something which the renal group at SPMIC are actively pursuing by adding this scan to almost every subject that goes in the scanner. Efforts have been made to avoid the quintessential machine learning mistakes such as imbalanced training data making the algorithm too specific and un-generalisable and the network only working for healthy subjects. We have also peaked inside the black box of the algorithm to check that it is behaving in a sensible and expected manner.

There is still work to be done on this segmentation method, as explained above, there are signs that data augmentation may improve both the accuracy and generalisability of the algorithm, this should be implemented and evaluated. By implementing data augmentation, the false positives observed on fringe slices may decrease however, if this is not the case then there are multiple solutions to reduce the prevalence of these errors such as basic binary filtering or modifying the networks architecture. There seems to be a reasonable degree of variability in the manually segmented data, to investigate this, the manual masking process should be repeated by a second observer at assess if this variability in the data is due to acquisition or human interpretation.

Another common segmentation task in renal imaging is to generate ROI for the renal cortex and medulla. There are some automated methods of achieving this once an overall renal mask has been produced [4], however there has been no work on the application of machine learning to this task. During the acquisition of the T_2 weighted data in Section 4.2.1, a sequence designed to optimise the contrast between cortex and medulla was also collected on each subject, an example of which is shown in Figure 4.8. Using this data it may be possible to develop the algorithm further so it can segment each tissue type within the kidneys.



Figure 4.8: An example of the data collected to enable segmentation of the renal cortex and medulla.

Ultimately the goal of this work is to produce an easy to use segmentation tool that can be utilised by clinicians and scientists alike. As such, time should be spent making the software easy to use with a simple front end/Graphical User Interface (GUI).

4.5 Acknowledgements

We gratefully acknowledge the support of NVIDIA Corporation with the donation of the Titan Xp GPU used for this research.

4.6 References

1. Daniel, A. *et al.* Automated Renal Segmentation in Healthy and Chronic Kidney Disease Subjects Using A Convolutional Neural Network in Proc. Intl. Soc. Mag. Reson. Med. 28 International Society of Magnetic Resonance in Medicine Annual Meeting (Online, Aug. 2020).
2. Cohen, E. I., Kelly, S. A., Edye, M., Mitty, H. A. & Bromberg, J. S. MRI Estimation of Total Renal Volume Demonstrates Significant Association with Healthy Donor Weight. *European Journal of Radiology. Rheumatoid Disease and Imaging* **71**, 283–287. issn: 0720-048X (1st Aug. 2009).
3. Van den Dool, S. W., Wasser, M. N., de Fijter, J. W., Hoekstra, J. & van der Geest, R. J. Functional Renal Volume: Quantitative Analysis at Gadolinium-Enhanced MR Angiography—Feasibility Study in Healthy Potential Kidney Donors. *Radiology* **236**, 189–195. issn: 0033-8419 (1st July 2005).
4. Cox, E. F. *et al.* Multiparametric Renal Magnetic Resonance Imaging: Validation, Interventions, and Alterations in Chronic Kidney Disease. *Frontiers in Physiology* **8**. issn: 1664-042X (2017).
5. Chapman, A. B. *et al.* Kidney Volume and Functional Outcomes in Autosomal Dominant Polycystic Kidney Disease. *Clinical Journal of the American Society of Nephrology* **7**, 479–486. issn: 1555-9041, 1555-905X (1st Mar. 2012).
6. Tangri, N. *et al.* Total Kidney Volume as a Biomarker of Disease Progression in Autosomal Dominant Polycystic Kidney Disease. *Canadian Journal of Kidney Health and Disease* **4**, 2054358117693355. issn: 2054-3581 (1st Jan. 2017).
7. Gong, I. H. *et al.* Relationship Among Total Kidney Volume, Renal Function and Age. *The Journal of Urology* **187**, 344–349. issn: 0022-5347 (Jan. 2012).
8. Zöllner, F. G. *et al.* Assessment of Kidney Volumes From MRI: Acquisition and Segmentation Techniques. *American Journal of Roentgenology* **199**, 1060–1069. issn: 0361-808X (1st Nov. 2012).
9. Seuss, H. *et al.* Development and Evaluation of a Semi-Automated Segmentation Tool and a Modified Ellipsoid Formula for Volumetric Analysis of the Kidney in Non-Contrast T2-Weighted MR Images. *Journal of Digital Imaging* **30**, 244–254. issn: 1618-727X (1st Apr. 2017).

4.6. References

10. Wachinger, C., Reuter, M. & Klein, T. DeepNAT: Deep Convolutional Neural Network for Segmenting Neuroanatomy. *NeuroImage. Segmenting the Brain* **170**, 434–445. issn: 1053-8119 (15th Apr. 2018).
11. Lu, F., Wu, F., Hu, P., Peng, Z. & Kong, D. Automatic 3D Liver Location and Segmentation via Convolutional Neural Network and Graph Cut. *International Journal of Computer Assisted Radiology and Surgery* **12**, 171–182. issn: 1861-6429 (1st Feb. 2017).
12. Chollet, F. *Keras* version 2.2.4. Keras, 2015.
13. Abadi, M. *et al.* TensorFlow: Large-Scale Machine Learning on Heterogeneous Distributed Systems, 19 (9th Nov. 2015).
14. Martín Abad *et al.* *TensorFlow* version 1.13.1. Tensorflow, 7th Aug. 2019.
15. Mahapatra, D. & Buhmann, J. M. Visual Saliency-Based Active Learning for Prostate Magnetic Resonance Imaging Segmentation. *Journal of Medical Imaging* **3**, 014003. issn: 2329-4302, 2329-4310 (Feb. 2016).
16. Chen, J., Yang, L., Zhang, Y., Alber, M. & Chen, D. Z. in *Advances in Neural Information Processing Systems* 29 (eds Lee, D. D., Sugiyama, M., Luxburg, U. V., Guyon, I. & Garnett, R.) 3036–3044 (Curran Associates, Inc., 2016).
17. Stollenga, M. F., Byeon, W., Liwicki, M. & Schmidhuber, J. in *Advances in Neural Information Processing Systems* 28 (eds Cortes, C., Lawrence, N. D., Lee, D. D., Sugiyama, M. & Garnett, R.) 2998–3006 (Curran Associates, Inc., 2015).

Chapter 5

Ex-Vivo Renal MRI

Abstract

This work was presented as a digital poster at the ISMRM 27th Annual Meeting 2019 [1] and as a poster at United Kingdom Kidney Week (UKKW) 2019 [2].

Lorem ipsum dolor sit amet, consectetuer adipiscing elit. Ut purus elit, vestibulum ut, placerat ac, adipiscing vitae, felis. Curabitur dictum gravida mauris. Nam arcu libero, nonummy eget, consectetuer id, vulputate a, magna. Donec vehicula augue eu neque. Pellentesque habitant morbi tristique senectus et netus et malesuada fames ac turpis egestas. Mauris ut leo. Cras viverra metus rhoncus sem. Nulla et lectus vestibulum urna fringilla ultrices. Phasellus eu tellus sit amet tortor gravida placerat. Integer sapien est, iaculis in, pretium quis, viverra ac, nunc. Praesent eget sem vel leo ultrices bibendum. Aenean faucibus. Morbi dolor nulla, malesuada eu, pulvinar at, mollis ac, nulla. Curabitur auctor semper nulla. Donec varius orci eget risus. Duis nibh mi, congue eu, accumsan eleifend, sagittis quis, diam. Duis eget orci sit amet orci dignissim rutrum.

5.1 Introduction

In the clinic, renal pathologies are currently assessed via blood tests, urine tests or biopsy followed by histological analysis. Given that both blood tests and urine tests are indirect measures of the health of the kidneys this means that biopsy is the most accurate diagnostic method routinely used however it is not without its shortcomings. From a patient experience point of view, collecting the tissue sample is an unpleasant and invasive process; from a diagnostic point of view, the results ascertained are not representative of the entirety of the kidney biopsied (typically the left), let alone the other kidney. Additionally, due to the invasive and destructive nature of the procedure, it is not ideal for longitudinal monitoring of renal health. Given these drawbacks in the current methodology, there has been a recent drive to enable the use of MRI for renal diagnosis as it has the potential to be better for both patients and clinicians. A key aspect in the widespread adoption of MRI in renal clinical practice, is a full understanding of the interplay between the current histological pipeline and the newly developed MRI measurements.

The best way to gain this insight is by analysing the same kidney in multiple ways. By taking samples from patients who are undergoing a nephrectomy as part of their standard treatment, it is possible to scan the kidneys in-vivo, remove the kidney, carry out histology and scan the sample ex-vivo. These three complimentary streams of data allow for the comparison of histology and in-vivo MRI with the ex-vivo scans acting as an intermediary, providing high-quality, high-resolution MR data.

Looking in the literature, there are two works that resemble this paradigm, the first, by Friedli et al, correlated T_1 and Apparent Diffusion Coefficient (ADC) with renal interstitial fibrosis and inflammation in a rat model [3]. Establishing a MRI predictor of interstitial fibrosis is especially important as it is present in the majority of renal pathologies and has been established as an excellent indicator of functional recovery [4]. Friedli was able to establish these correlations by scanning the organ in-vivo, ex-vivo and then carrying out histology. It is this sort of methodology we intend to apply to human samples. Another work by Uribe et al carried out a similar process investigating the diagnostic capabilities of ADC and fractional anisotropy in prostate cancer using human samples [5]. Although there has not been much work correlating human kidney MRI with histology, there has been interesting work on ex-vivo MRI samples using similar methods to those we wish to undertake. A very comprehensive paper by Sengupta et al details their ability to image an

80 mm³ sample of human occipital lobe generating 60 μm isotropic T_2^* weighted data and 200 μm isotropic quantitative T_2^* maps [6]. This was achieved on a 9.4T human scanner using a custom made 16 channel phased array and shows the benefits that custom hardware can bring to ex-vivo imaging on human scanners.

As the purpose of this study is to compare pre-existing histological analysis with newly developed, but previously documented, renal MRI protocols, the largest area in need of development is the ex-vivo scanning of samples, as such this is a large focus of this chapter. Here, the aim is to collect ADC, T_1 , T_2 and T_2^* data both ex-vivo and in-vivo for comparison. Established protocols exist within the group for ADC, T_1 and T_2^* collection but there are multiple methods of renal T_2 mapping which have not been optimised [7–10]. Here T_2 mapping methods are compared before choosing one to include in the scan card to perform on nephrectomy patients. As well as the MRI acquisition, attention needs to be paid to the fixing process. It will not be possible to scan unfixed organs therefore, a knowledge of the effects fixation has upon the kidneys needs to be gained. No literature on this topic exists and thus, this is an area we need to explore ourselves.

5.2 Methods

5.2.1 Sample Acquisition and Fixation

Initial samples were acquired from a local slaughterhouse, placed into Phosphate-buffered Saline (PBS) for transport to the laboratory before being transferred to ten times the samples volume of 10% Neutral Buffered Formalin (NBF) for twenty four hours. The time between slaughter and transferring the samples to NBF was reduced as much as possible to minimise the effects of ischemic injury. Once the samples had been fixed they were washed in fresh PBS and remained in this solution while being scanned to avoid susceptibility artefacts that would be induced by either scanning the samples immersed in NBF or in air. Where possible, both kidneys were collected from the animal, with one being used for MRI and the other being used to biopsy for histological staining. While the samples acquired from the slaughterhouse were useful for early development work there were consistency issues that will be explained in detail in Section 5.3, for this reason a collaboration between SPMIC and The University of Nottingham School of Veterinary Medicine and Science has begun. This allows the procurement of much higher quality samples with a greater degree of control.

5.2.2 T_1 Mapping

Acquisition

Ex-vivo T_1 maps can be acquired at field strengths of 3T and 7T. If the time at which the sample is scanned does not need to be precisely controlled or matched with the time of biopsy then the sample can be scanned at both field strengths successively however if scanning and biopsy needed to be time matched then the sample is only scanned at 3T.

T_1 maps are produced using an ultrafast gradient echo scheme. By carrying out multiple scans with different TI it is possible to sample the inversion recovery of the tissue and as such, estimate T_1 . An example of the acquisitions at each inversion time is shown in Figure 5.1

5.2. Methods

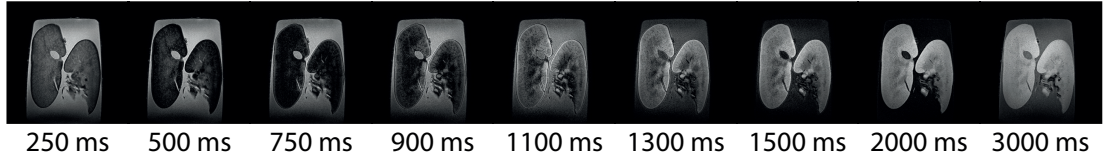


Figure 5.1: Acquisitions at each of the TI at 7T.

The acquisition parameters at 3T are $\text{FOV} = 160 \times 160 \times 50 \text{ mm}$, voxel size = $0.7 \times 0.7 \times 1.0 \text{ mm}^3$, $\text{TR/TE} = 11 \text{ ms}/5 \text{ ms}$, $\text{FA} = 8^\circ$, Bandwidth = 41.6 Hz/pixel, TFE Factor = 64, SENSE Factor = 2.5, Acquisition Time $\approx 270 \text{ sec}$ per TI collected. The acquisition parameters at 7T are $\text{FOV} = 192 \times 170 \times 24 \text{ mm}$, voxel size = $0.6 \times 0.6 \times 0.6 \text{ mm}^3$, $\text{TR/TE} = 7.2 \text{ ms}/3.3 \text{ ms}$, $\text{FA} = 8^\circ$, Bandwidth = 56.8 Hz/pixel, TFE Factor = 240, SENSE Factor (P/S) = 2.0/1.5, Acquisition Time $\approx 270 \text{ sec}$ per TI collected. Initially inversion times of 400 ms, 500 ms, 750 ms, 900 ms, 1100 ms, 1300 ms and 1500 ms were collected at 3T and inversion times of 250 ms, 500 ms, 750 ms, 900 ms, 1100 ms, 1300 ms, 1500 ms, 2000 ms and 3000 ms at 7T however to reduce the scan time of the 3T protocol, this was reduced to inversion times of 400 ms, 500 ms, 750 ms, 900 ms, 1100 ms and 2600 ms. The choice of these inversion times will be elaborated upon later.

Analysis

The signal recorded at each inversion time is proportional to the modulus of the true longitudinal magnetisation, Figure 5.2. To combat this we can apply polarity correction to the data by saving the phase information and applying the methods of Szumowski et al [11]. This results in a greater dynamic range and thus smaller confidence intervals than using the none polarity corrected data.

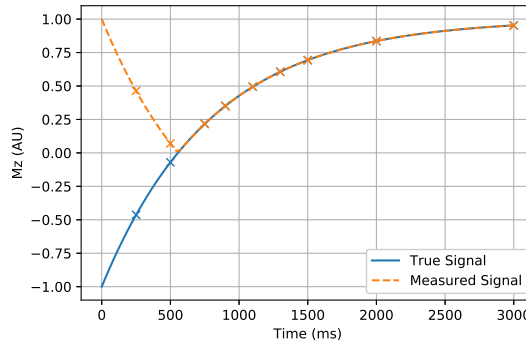


Figure 5.2: A simulation of the true and measured magnetisation for a T_1 of 800 ms. The crosses represent the inversion times at which the inversion recovery is sampled.

5.2. Methods

Once the data has been polarity corrected a voxel by voxel least squares trust region reflective method is used to fit the data to Equation (5.1) and estimate the T_1 and M_0 of the tissue in that voxel along with an uncertainty in the fit [12]. This data processing is carried out using an in-house Python package. Once the T_1 maps are generated, ROI are defined for the renal medulla and renal cortex and the mean T_1 in these ROI recorded.

$$M_z = M_0 \left(1 - 2 \cdot e^{-TI/T_1} \right) \quad (5.1)$$

5.2.3 T_2 Mapping

Compared to other quantitative renal measurements, T_2 mapping is still relatively un-explore in-vivo or ex-vivo with little consensus in the community about which methods are best suited to each situation [13]. This lack of consensus and existing literature meant that more work was required to establish the optimum protocol for our use case. Due to this works interest to the wider community out of the context of the nephrectomy paradigm, the development and comparison of T_2 mapping protocols is explored in Chapter 2.

5.2.4 T_2^* Mapping

Acquisition

Ex-vivo T_2^* maps can be acquired at both 3T and 7T using a multi-slice FFE sequence with scans being performed at a range of different echo times. An example of the acquisition at each echo time is shown in Figure 5.3

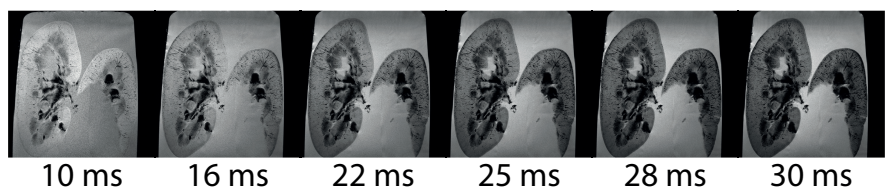


Figure 5.3: Acquisitions at each of the TE at 7T.

The acquisition parameters at 3T are $\text{FOV} = 145 \times 145 \times 15 \text{ mm}$, voxel size = $0.6 \times 0.6 \times 1.5 \text{ mm}^3$, $\text{TR} = 697 \text{ ms}$, $\text{FA} = 38^\circ$, SENSE Factor = 2.0, Acquisition Time $\approx 180 \text{ sec}$ per TE collected. The acquisition parameters at 7T are $\text{FOV} = 145 \times 145 \times 10 \text{ mm}$, voxel size = $0.5 \times 0.5 \times 1.0 \text{ mm}^3$, $\text{FA} = 38^\circ$, SENSE Factor = 2.0, Acquisition Time $\approx 180 \text{ sec}$ per TE collected. Initially echo times were 15 ms, 20 ms, 25 ms, 30 ms, 35 ms, 40 ms and 50 ms at 3T and 10 ms, 16 ms, 22 ms, 25 ms, 28 ms and 30 ms at 7T however to reduce

5.2. Methods

acquisition times, the 3T echo times were reduced to 15 ms, 20 ms, 25 ms, 40 ms and 50 ms.

Analysis

The data is fit voxel by voxel using a weighted echo time fit from the log of the exponential signal decay (Equation (5.2)) to generate the T_2^* maps [14]. This data processing is carried out using an in-house Python package. The ROI were defined using the T_1 weighted data if available as it has a greater cortical medullary contrast at shorter times from fixation. The mean T_2^* in these ROI is recorded.

$$S(t) = S_0 \cdot e^{-TE/T_2^*} \quad (5.2)$$

5.2.5 Apparent Diffusion Coefficient

Acquisition

Optimisation of b values

Post-Processing and Analysis

5.2.6 Diffusion Tensor Imaging

As part of the nephrectomy protocol, Chapter 5, we want to be able to assess the microstructure of the kidneys, one avenue to pursue for this is the use of Diffusion Tensor Imaging (DTI). FA has been shown to correlate with GFR [15] and mean tract length is an indicator of ureteropelvic junction obstruction [16] showing that tractography can be used to assess renal structure.

One of the major hurdles to overcome in developing a renal DTI protocol for this study was correction of both EPI readout distortions and eddy current induced distortions. This was achieved using a pipeline based around FSL's topup [17, 18] and eddy [19] routines. Key acquisition parameters for the sequence are 64 directions arranged over a whole spherical shell to assist with eddy current correction, this whole acquisition is then repeated with the opposite phase-encode direction to enable EPI distortion correction. A b-value of 600 s/mm² is used. FA maps are generated using FSL and tractography is processed using an in-house pipeline developed using the Dipy Python library [20].

5.2. Methods

Using this pipeline, images such as those in figures 5.4 and 5.5 could be produced. This protocol is now ready to be used on patients undergoing a nephrectomy.

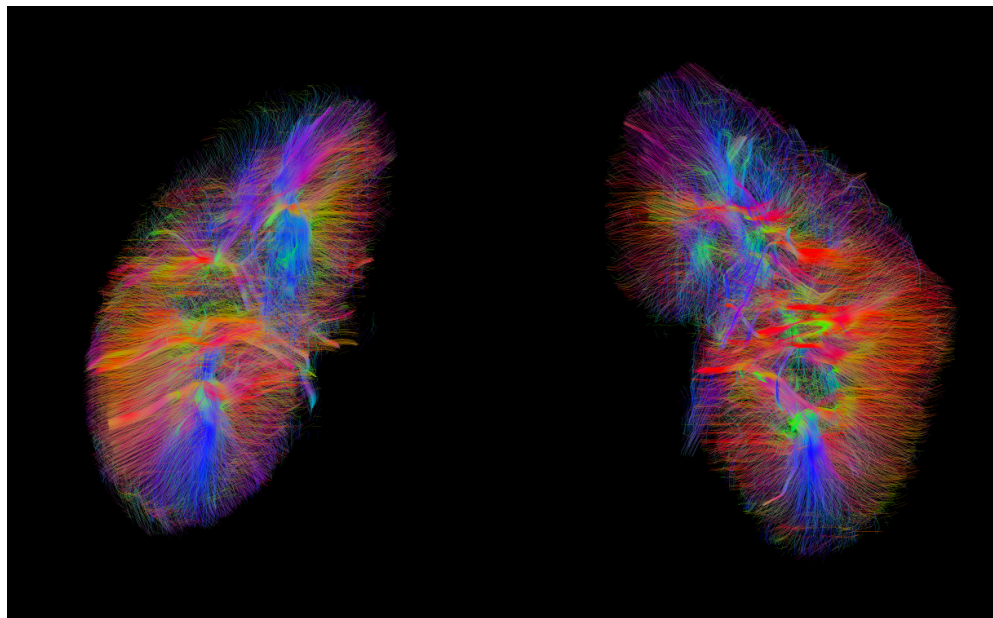


Figure 5.4: Example tractography generated using the above protocol.

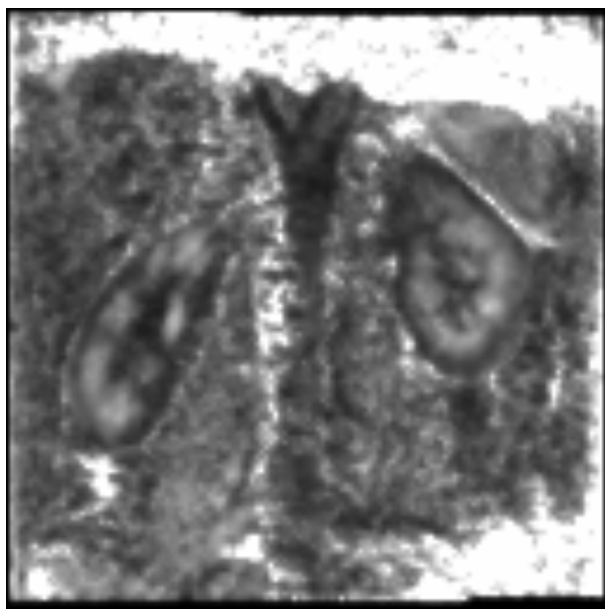


Figure 5.5: An example FA map generated using the protocol above.

Acquisition

Post-Processing and Analysis

Distortion Correction

5.2. Methods

Fractional Anisotropy

Tractography

5.2.7 Layer Based Analysis

The vast majority of analysis of renal MRI data is based around defining ROI within the kidneys. While this method has provided excellent results, it is by no means perfect as these ROI need to be manually defined, leading to human bias, or defined by an automated method which, as outlined in Chapter 4, can be difficult to generalise.

Taking inspiration from the analysis pipelines used by neuroimagers [21–23], a method of dividing the kidneys into layers of equal thickness was developed. This method uses a three-dimensional FreeSurfer mesh on the surface of the kidney [24] and levelsets to produce a map of how far each voxel is from the surface. From this map it is possible to place voxels into layers of any thickness. An example of this method being applied to both the brain and an ex-vivo kidney sample can be seen, figures 5.6a and 5.6b respectively.

One of the main challenges in transferring this technique is coping with the reduced FOV that comes with body imaging. Given that the method essentially asks how far is each voxel from the closes vertex on the mesh, if the mesh has a large hole in it where the slices stop covering the kidney, then the quantitative nature of this depth map is compromised.

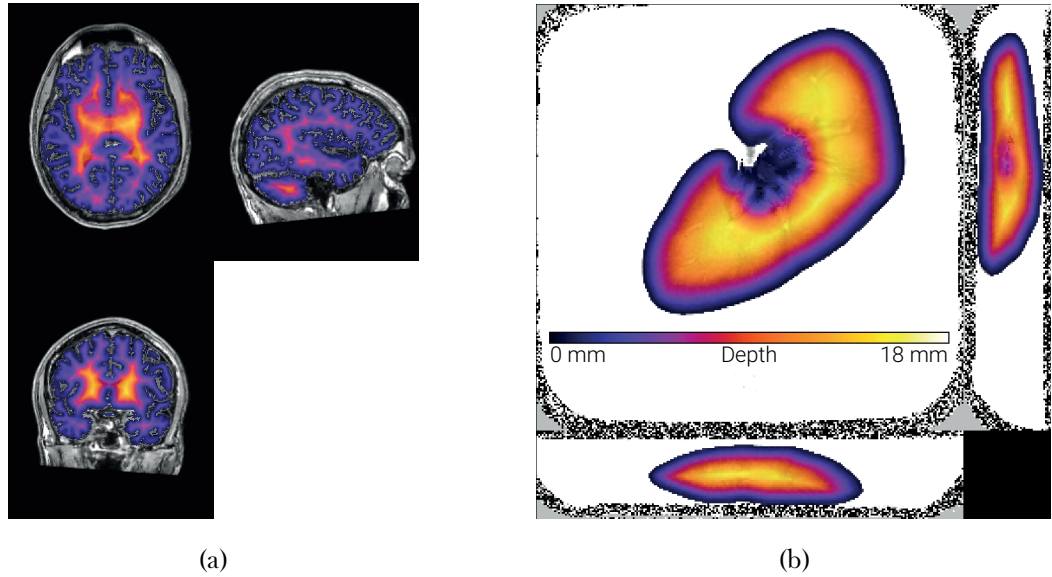


Figure 5.6: (a) A depth mask of the brain. Lighter areas are deeper inside the brain. (b) A depth mask applied to a quantitative T_1 map.

This levelset method was compared to two other methods of producing layers in the kidneys, a two-dimensional and a three-dimensional version of the Twelve Layer Concentric Objects (TLCO) method [25, 26]. Each method was tested with a volume that included the entire kidney, and a cropped volume that only included the central section of the kidney, simulating the reduced FOV that is common in body imaging. The layers generated were applied to a T_1 map with the mean and standard deviation of T_1 in each layer being plotted, Figure 5.7.

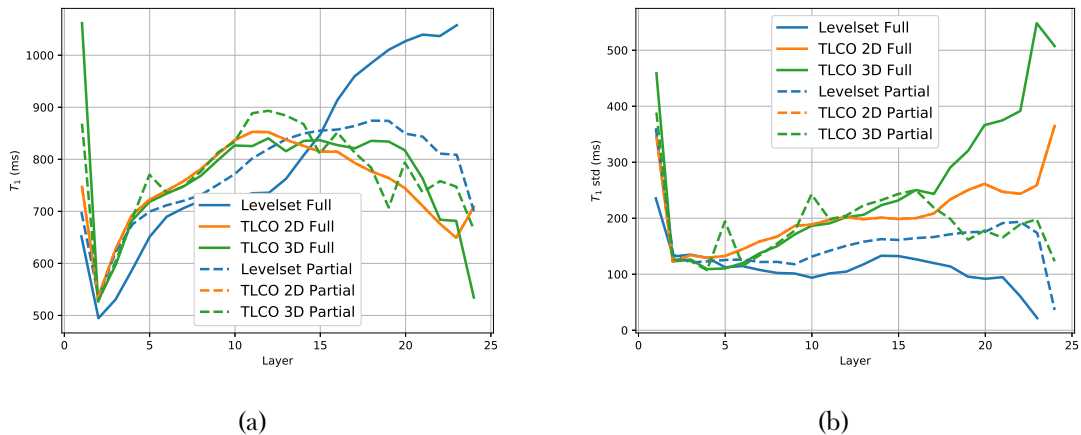


Figure 5.7: (a) The mean T_1 within each layers produced by each of the three methods when processing either the full volume of the kidney or only the central slices. (b) The standard deviation of the T_1 within the layers produced by each method.

5.2. Methods

In Figure 5.7b we can see that the layers output by the levelset method when applied to a full volume dataset produce the minimum standard deviation, this means the layers are the most anatomically sensible as a smooth transition of T_1 is expected with depth in the kidney and therefore the variance in each layer should be relatively small. Given this method produces the most realistic layers, other methods will be compared to it.

Neither of the TLCO methods manage to capture the increase in T_1 that can be seen deeper in the kidney. They also have a much larger standard deviation per layer for deeper layers than the levelset method implying that the layers produced are a mixture of cortex and medulla. When comparing the performance of each method with only a partial volume of kidney, the levelset method produces the results that are closer to that of the full volume levelset.

Given this method can be used both in-vivo and on ex-vivo samples, they will make for an interesting additional analysis pipeline for the work in Chapter 5.

5.3 Results and Discussion

5.3.1 Fixation and Protocol Development

As was alluded to in Section 5.2.1, there was significant variability in the quality of the samples collected from the slaughterhouse. This was largely due to the legislation surrounding animals slaughtered to enter the human food chain. If any part of the animal is destined for human consumption then the carcase must be thoroughly inspected before any tissue can be released. This can cause two issues. As part of the inspection, the kidneys need to be examined for parasites, this is done by making an incision in the organ, however, the quality of this incision can vary massively with some samples having a 20 mm slice cut into them while others are roughly cut in half. The second issue is caused by the variable time between slaughter and the tissue being released after inspection. For these reasons kidneys began to be procured from Veterinary Science collaborating with Prof David Gardner. The animals slaughtered there are not destined for human consumption and as such the kidneys can be placed into PBS and subsequently NBF far quicker and the kidneys do not need to be sliced open for inspection. The difference in the samples from these two sources can clearly be seen in Figure 5.8. This collaboration also enables the procurement of kidneys from a greater range of animals including different ages of pigs and therefore different degrees of fibrosis and inducing Acute Kidney Injury (AKI) in the animals prior to scanning and histology. Veterinary Science can also carry out the histology in house, thus streamlining the protocol by avoiding transporting one kidney to Derby for histology and the other to SPMIC for scanning.

5.3. Results and Discussion

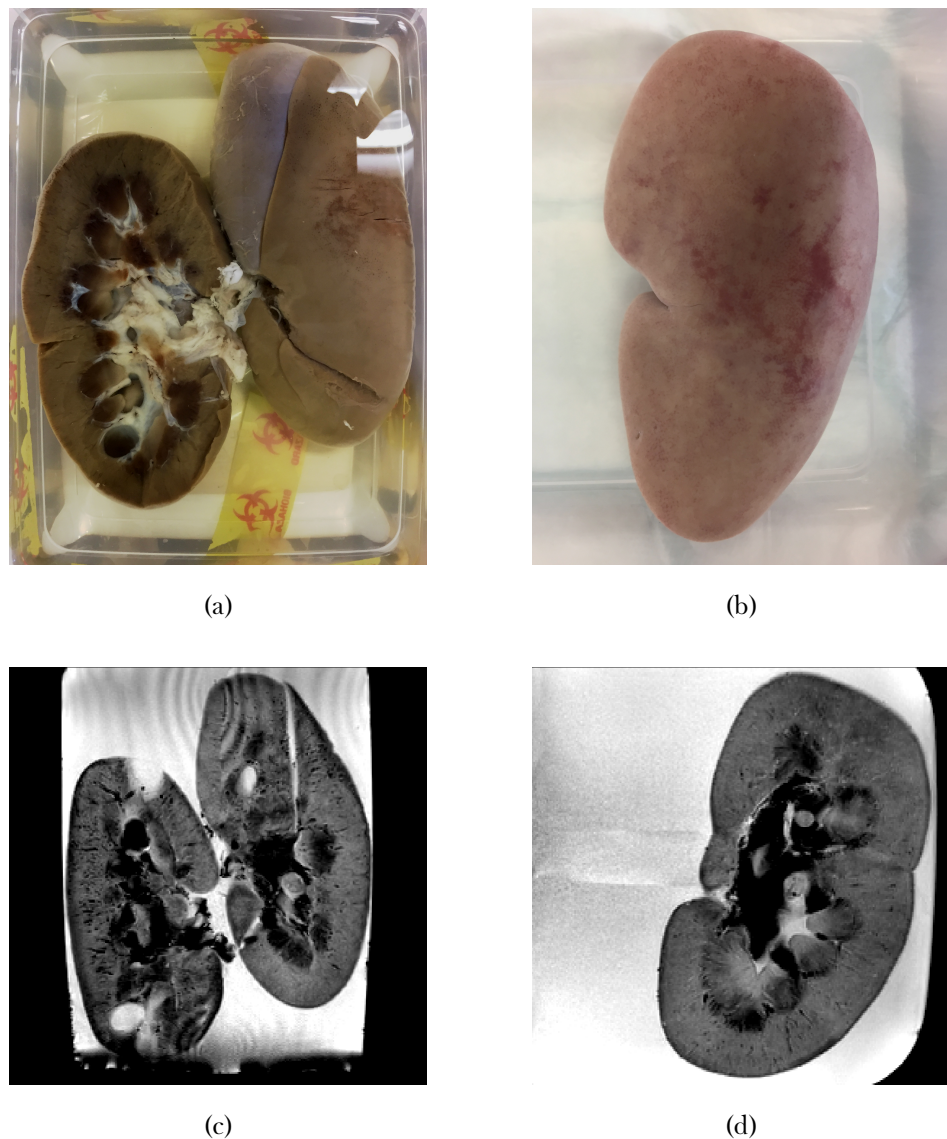


Figure 5.8: (a) An example of a sample procured from the slaughterhouse after it has been fixed. The left hand kidney has been sliced in half; the right hand kidney has the incisions from the meat inspector clearly visible. (b) An example of a sample procured from Veterinary Science post fixing. (c) An example of a T_2 weighted FFE with TE = 40 ms of a kidney procured from the slaughterhouse. (d) An example of a T_2 weighted FFE with TE = 40 ms of a kidney procured from Veterinary Science.

Once samples had been fixed and transferred to PBS they could be placed into the scanner. Using the protocols outlined above it was possible to generate maps as shown in Figure 5.9.

5.3. Results and Discussion

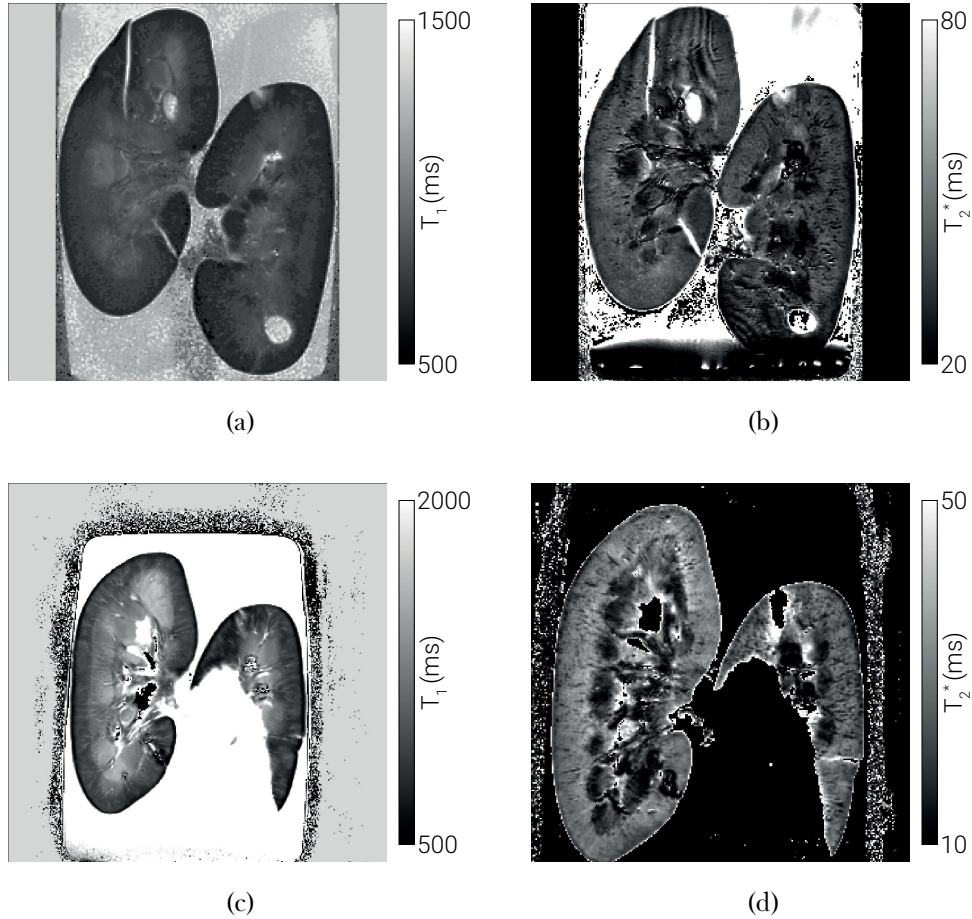


Figure 5.9: (a) T_1 map of a kidney twenty four hours after fixation at 3T (b) T_2^* map twenty four hours after fixation at 3T (c) T_1 map twenty four hours after fixation at 7T (d) T_2^* map twenty four hours after fixation at 7T. The sample shown in the 3T and 7T figures is different.

5.3.2 Monitoring Changes in MR Parameters Post Fixation

To study the effects of the fixation process upon MR measurements, a kidney was fixed as per the method in Section 5.2.1 and scanned at both field strengths of 3T and 7T. Collecting a T_1 and T_2^* map took approximately 90 minutes per field strength. Once the maps had been generated, ROI were defined and the mean T_1 and T_2^* for the cortex and the medulla were calculated. The sample was monitored for ten weeks. The variation in T_1 and T_2^* over time can be seen in Figure 5.10.

5.3. Results and Discussion

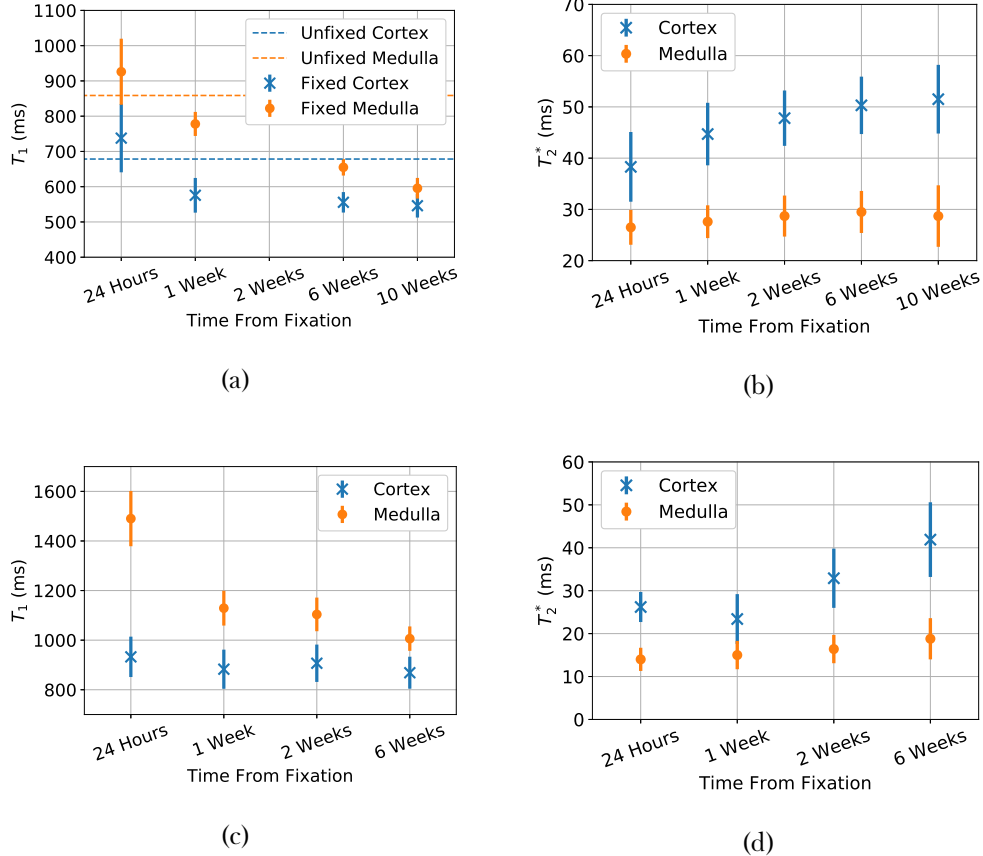


Figure 5.10: (a) Variation in T_1 as a function of time after fixation measured at 3T (b) Variation in T_2^* as a function of time after fixation measured at 3T (c) Variation in T_1 as a function of time after fixation measured at 7T (d) Variation in T_2^* as a function of time after fixation measured at 7T.

Unfortunately due to technical scanner issues, we were not able to scan the sample at 7T at ten weeks and the quality of the 3T T_1 acquisition at two weeks was significantly inferior; as such these data points have been omitted. It can be seen that the largest changes in T_1 and T_2^* occur between twenty four hours and one week after fixation, after that there is a general trend that the T_1 of the cortex and medulla converge while the T_2^* of each tissue type diverges, one could argue that the T_2^* of the cortex measured at 3T is plateauing. This means that, although the samples will reach a steady state, in the first few weeks after fixation, their T_1 and T_2^* will have a dependence on time. This necessitates the need to standardise the protocol, specifically the time at which the samples are scanned. It would have been useful to know the T_1 and T_2^* of unfixed porcine kidneys and as such, a fresh, unfixed kidney was scanned using the same protocol. Unfortunately, due to the difference in stiffness between fixed and unfixed kidneys, the same protocol did not deliver usable T_2^* data as the unfixed kidney vibrated too much while floating in the PBS. This problem could potentially be

5.3. Results and Discussion

reduced by either vibration insulation between the sample and the scanner as per Dawe et al [27] or by embedding the sample in an agarose medium rather than allowing it to float in PBS as per Kolk et al[28]. The T_1 of the unfixed kidney was seen to be between that of the fixed kidney between 24-hours and one week.

To investigate this time dependence over a shorter time scale, a pair of kidneys were acquired and fixed as before. It will be possible to scan most human samples within 24 hours of fixation, as such it is desirable to see how much T_1 , T_2^* and histology change over this period. Scanning was only carried out at 3T as more frequent measurements were preferable to measurements at different field strengths. For this reason the number of inversion times and echo times used to generate the T_1 and T_2^* maps was reduced to TI = 400 ms, 500 ms, 750 ms, 900 ms, 1100 ms, 2600 ms and TE = 15 ms, 20 ms, 25 ms, 40 ms, 50 ms respectively. The choice of these inversion/echo times was arrived at empirically by carrying out the analysis pipeline on a single slice of data using each combination of six and five of the previously used TIs and TEs respectively. The results from each combination of TI/TE were compared to those generated when using the full complement of inversion/echo times and the combination delivering the minimum difference chosen. This reduction in the number of inversion times resulted in a mean error per voxel in the kidney of 20.9 ± 12.3 ms if the full complement of inversion times was taken as the ground truth, the reduction in echo times resulted in a mean error of 0.3 ± 1.2 ms.

Scanning sessions started at 1.5 hours, 2.5 hours, 4 hours, 5.5 hours, 19 hours and 22 hours after the sample was removed from the NBF. Due to the potential for the properties to change relatively quickly, especially T_1 , it was decided to randomise the order in which the inversion/echo times were collected, this way any change in T_1/T_2^* over the 30/20 minute acquisition period would manifest itself as non-systematic noise and thus will increase the uncertainty in the fit rather than affecting the predicted value. At the start of each scanning session, a biopsy was performed on the kidney not being scanned. Masson's trichrome and Haematoxylin and Eosin (H and E) staining was performed on these samples.

5.3. Results and Discussion

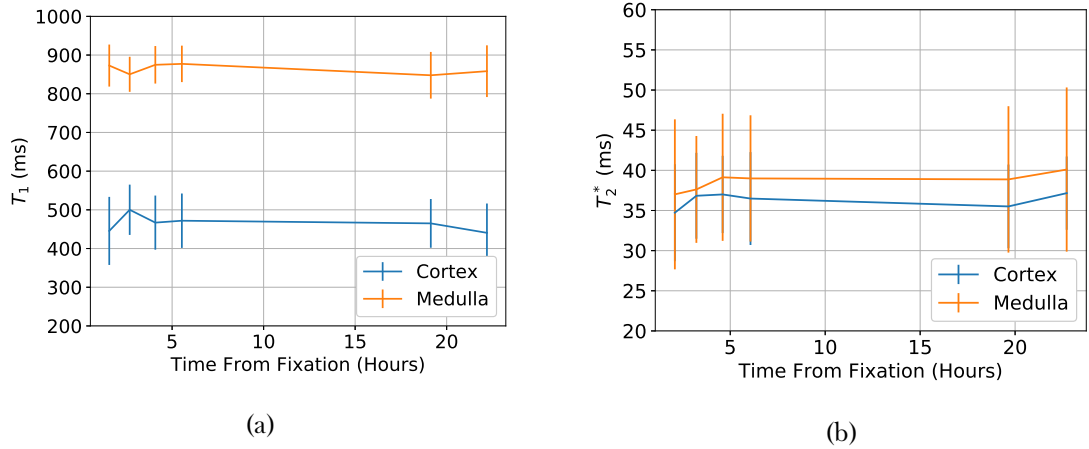


Figure 5.11: (a) Variation in T_1 as a function of time after fixation measured at 3T (b) Variation in T_2^* as a function of time after fixation measured at 3T.

No significant change in T_1 or T_2^* was observed over the period the sample was monitored. This is promising as it means that when this protocol is applied to human samples, there will be a relatively large time window in which the ex-vivo scan can be carried out, making the experimental procedure simpler. The corresponding histology results showed no change in the cortex over this period however there was a noticeable inflammatory response in the medulla.

It was noted that the sample used for this experiment was not of especially high quality, the kidney has two slices in it, one that almost bifurcated the sample along the coronal plane, another cut down one half of the sample along the sagittal plane, visible in Figure 5.12a. These cuts meant that air became trapped within the sample causing it to float in the PBS. If not corrected this would cause large susceptibility artefacts where the sample came into contact with the air at the top of the PBS; to remedy this the sample was entirely bifurcated. Despite the best efforts of investigators, air bubbles remained in the sagittal slice, causing the aforementioned artefacts, especially visible in Figure 5.12b. Given these concerns over sample quality, it was decided to scan the sample again one week after fixation, to match the time period in the previous experiment (Figure 5.10).

5.3. Results and Discussion

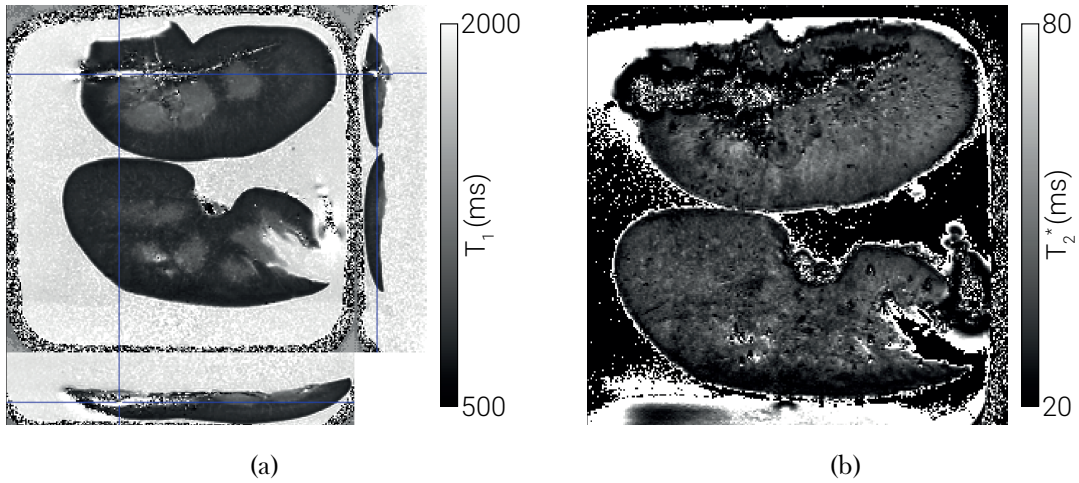


Figure 5.12: (a) An example of the T_1 map collected from the short time scale kidney (b) An example of the T_2^* map collected from the short time scale kidney.

It was expected that upon repeating the measurements one week later, the T_1 of both cortex and medulla would decrease and the T_2^* of the cortex would increase. This was not the case, there was a slight decrease in the T_1 of the medulla but otherwise, no change was observed, Figure 5.13. This lead us to conclude that the large cuts in the sample had lead to a different level of fixation. Subsequent to this, samples were to be procured from Veterinary Science as they are more consistent and therefore more akin to the human samples that will be used.

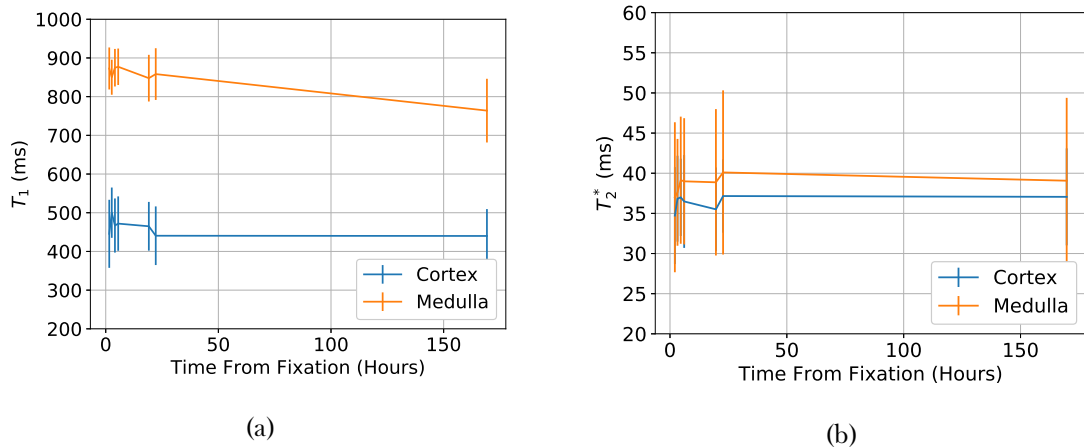


Figure 5.13: (a) Variation in T_1 as a function of time after fixation measured at 3T (b) Variation in T_2^* as a function of time after fixation measured at 3T.

5.3.3 Comparing MR and Histological Measures in Aged Kidneys

To verify the correlation of MR measurements with histology, kidneys were collected from a 0.5 year old and 2.5 year old pig. These different ages were expected to have differing levels of renal inflammation and fibrosis. Figure 5.14 shows example MRI data collected from these samples, Figure 5.15 shows the quantitative differences in T_1 and T_2^* between the two samples.

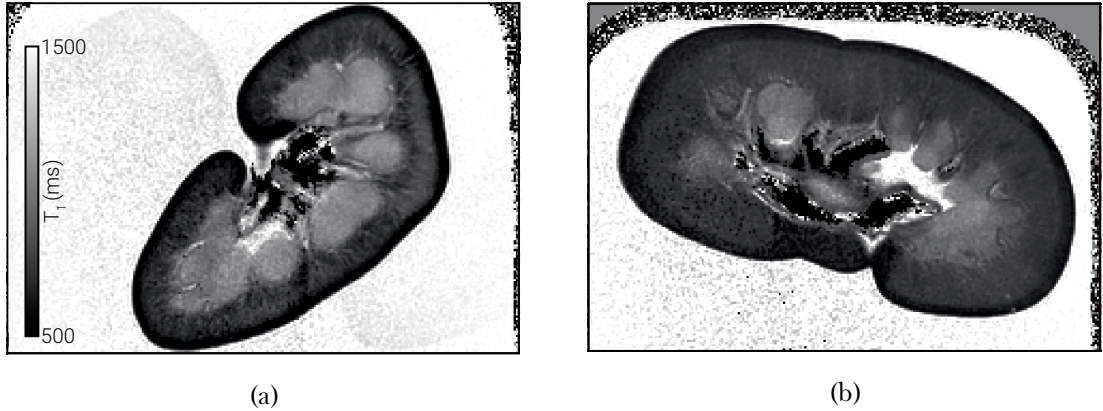


Figure 5.14: (a) T_1 map of a 0.5 year old pig kidney. (b) T_1 map of a 2.5 year old pg kidney.

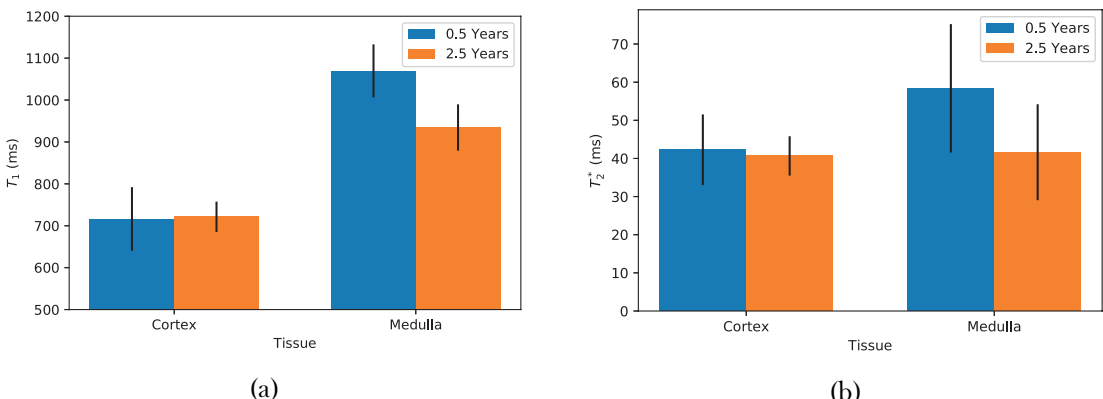


Figure 5.15: (a) The T_1 of the renal cortex and medulla of the two samples. (b) The T_2^* of the renal cortex and medulla of the two samples.

No significant change is observed in the T_1 or T_2^* of cortex the two kidneys. There is however a decrease in T_1 seen in the medulla of the older kidney. Cortical samples were removed from the same animals for histological analysis. These samples were stained using H and E and Masson's trichrome to enable the evaluation of levels of fibrosis, these micrographs are shown in Figure 5.16.

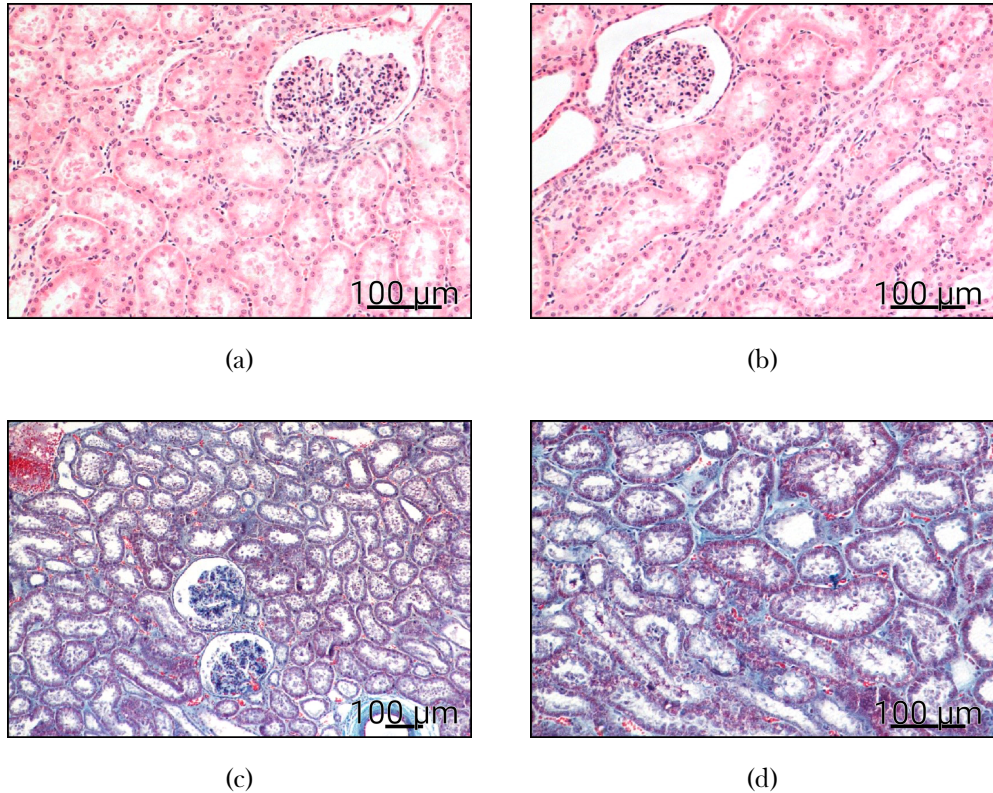


Figure 5.16: (a) A sample of renal cortex from a 0.5 year old pig stained with H and E. (b) A sample of renal cortex from a 2.5 year old pig stained with H and E. (c) A sample of renal cortex from a 0.5 year old pig stained with Masson's trichrome. (d) A sample of renal cortex from a 2.5 year old pig stained with Masson's trichrome.

No significant difference is seen between the histology of these cortical samples. This means that MRI and histology are in agreement. Unfortunately no samples were taken from the renal medulla, the area which showed a change in MR measurements. In future samples with a larger difference in age should be used as these will have a greater difference in fibrosis and samples should be taken from the medulla for histological analysis.

5.4 Conclusions and Future Work

This chapter shows progress towards correlating renal MRI measurements with histology. We are able to acquire high resolution T_1 , T_2 , T_2^* maps. We have also developed protocols to carry out simultaneous biopsy for histology and MRI acquisition. These protocols have shown that the T_1 and T_2^* of the kidneys are not constant after fixation however there is a window of 24-hours after fixation in which scanning is optimum. We have also shown that these measures agree with histology. Below are listed some of the directions in which future work could explore.

5.4.1 Protocol Validation on a Single Sample

As each protocol, including those in Section ??, has been developed separately, they have not been carried out on the same sample, as the intention is to use all the protocols outlined in Section 5.2 on each nephrectomy sample, it would be useful to collect all protocols on a single sample. This could be coupled with a repeat investigation into the effects of ageing by collecting data from kidneys with a larger difference in ages.

5.4.2 Ex-Vivo Sample Coil

Sengupta demonstrated the benefits of using custom made ex-vivo sample coils in human scanners [6]. Currently scanning uses the standard head coils however this results in a relatively large distance between sample and coils as seen in Figure 5.17. There would certainly be improvements in data quality if a coil specifically designed for small sample imaging at 7T were fabricated.



Figure 5.17: A sample sat within the 32 channel 3T head coil. A bespoke ex-vivo sample coil would have less space between the coil and the sample.

5.4.3 Human Organs

All work thus far has been using porcine kidneys. While these provide an excellent model for protocol development due to their similarities to human kidneys, the utility of this investigation will be enhanced massively when human organs are studied. To this end, once the development work has been completed and protocols finalised, samples will begin to be procured from subjects undergoing a nephrectomy as part of their standard clinical care.

Another source of human organs are those rejected for transplant. Due to the relatively small time window in which a transplant centre has between an organ donation being made and the organ losing its transplant viability, a large number of human kidneys are unable to be successfully donated. While not suitable for transplant any more, these organs would still be useful in providing ex-vivo MRI data and histology in the healthy population. There are pre-existing agreements enabling failed transplant tissue to be used in scientific research, as such, this would be an interesting avenue to explore.

5.5 Acknowledgements

We are grateful for access to the University of Nottingham's Augusta high performance computing service.

5.6 References

1. Daniel, A. *et al.* *The Effects of Fixation and Age on Relaxometry Measurements of Ex-Vivo Kidneys* in *Proc. Intl. Soc. Mag. Reson. Med.* 27 International Society of Magnetic Resonance in Medicine Annual Meeting (Montreal, 13th May 2019).
2. Kazmi, I. *et al.* *Determining Optimal Technique for Tissue Fixation for Ex-Vivo MRI Imaging of Porcine Kidneys* in. United Kingdom Kidney Week (Brighton, 6th May 2019).
3. Friedli, I. *et al.* New Magnetic Resonance Imaging Index for Renal Fibrosis Assessment: A Comparison between Diffusion-Weighted Imaging and T1 Mapping with Histological Validation. *Scientific Reports* **6**. issn: 2045-2322. pmid: 27439482 (21st July 2016).
4. Risdon, R. A., Sloper, J. C. & De Wardener, H. E. Relationship Between Renal Function and Histological Changes Found In Renal-Biopsy Specimens From Patients With Persistent Glomerular Nephritis. *The Lancet. Originally Published as Volume 2, Issue 7564* **292**, 363–366. issn: 0140-6736 (17th Aug. 1968).
5. Uribe, C. F. *et al.* In Vivo 3 T and Ex Vivo 7 T Diffusion Tensor Imaging of Prostate Cancer: Correlation with Histology. *Magnetic Resonance Imaging* **33**, 577–583. issn: 0730-725X, 1873-5894 (1st June 2015).
6. Sengupta, S. *et al.* High Resolution Anatomical and Quantitative MRI of the Entire Human Occipital Lobe Ex Vivo at 9.4T. *NeuroImage*. issn: 1053-8119 (20th Mar. 2017).
7. Wolf, M. *et al.* Magnetic Resonance Imaging T1- and T2-Mapping to Assess Renal Structure and Function: A Systematic Review and Statement Paper. *Nephrology Dialysis Transplantation* **33**, ii41–ii50. issn: 0931-0509 (suppl_2 1st Sept. 2018).
8. Franke, M. *et al.* Magnetic Resonance T2 Mapping and Diffusion-Weighted Imaging for Early Detection of Cystogenesis and Response to Therapy in a Mouse Model of Polycystic Kidney Disease. *Kidney International* **92**, 1544–1554. issn: 0085-2538 (1st Dec. 2017).
9. Li, X., Bolan, P. J., Ugurbil, K. & Metzger, G. J. Measuring Renal Tissue Relaxation Times at 7 T. *NMR in Biomedicine* **28**, 63–69. issn: 1099-1492 (2015).
10. Zhang, J. L. *et al.* *Reproducibility of R2* and R2 Measurements in Human Kidneys* in *Proc. Intl. Soc. Mag. Reson. Med.* 19 ISMRM. **19** (2011), 2954.

5.6. References

11. Szumowski, J. *et al.* Signal Polarity Restoration in a 3D Inversion Recovery Sequence Used with Delayed Gadolinium-Enhanced Magnetic Resonance Imaging of Cartilage (dGEMRIC). *Journal of Magnetic Resonance Imaging* **36**, 1248–1255. ISSN: 1522-2586 (1st Nov. 2012).
12. Branch, M., Coleman, T. & Li, Y. A Subspace, Interior, and Conjugate Gradient Method for Large-Scale Bound-Constrained Minimization Problems. *SIAM Journal on Scientific Computing* **21**, 1–23. ISSN: 1064-8275 (1st Jan. 1999).
13. Dekkers, I. A. *et al.* Consensus-Based Technical Recommendations for Clinical Translation of Renal T1 and T2 Mapping MRI. *Magnetic Resonance Materials in Physics, Biology and Medicine*. ISSN: 1352-8661 (22nd Nov. 2019).
14. Cox, E. F. *et al.* Multiparametric Renal Magnetic Resonance Imaging: Validation, Interventions, and Alterations in Chronic Kidney Disease. *Frontiers in Physiology* **8**. ISSN: 1664-042X (2017).
15. Liu, Z. *et al.* Chronic Kidney Disease: Pathological and Functional Assessment with Diffusion Tensor Imaging at 3T MR. *European Radiology* **25**, 652–660. ISSN: 0938-7994, 1432-1084 (1st Mar. 2015).
16. Delgado, J. *et al.* Pilot Study on Renal Magnetic Resonance Diffusion Tensor Imaging: Are Quantitative Diffusion Tensor Imaging Values Useful in the Evaluation of Children with Ureteropelvic Junction Obstruction? *Pediatric Radiology* **49**, 175–186. ISSN: 1432-1998 (1st Feb. 2019).
17. Andersson, J. L. R., Skare, S. & Ashburner, J. How to Correct Susceptibility Distortions in Spin-Echo Echo-Planar Images: Application to Diffusion Tensor Imaging. *NeuroImage* **20**, 870–888. ISSN: 1053-8119 (1st Oct. 2003).
18. Smith, S. M. *et al.* Advances in Functional and Structural MR Image Analysis and Implementation as FSL. *NeuroImage. Mathematics in Brain Imaging* **23**, S208–S219. ISSN: 1053-8119 (1st Jan. 2004).
19. Andersson, J. L. R. & Sotiroopoulos, S. N. An Integrated Approach to Correction for Off-Resonance Effects and Subject Movement in Diffusion MR Imaging. *NeuroImage* **125**, 1063–1078. ISSN: 1053-8119 (15th Jan. 2016).
20. Garyfallidis, E. *et al.* Dipy, a Library for the Analysis of Diffusion MRI Data. *Frontiers in Neuroinformatics* **8**. ISSN: 1662-5196 (2014).

5.6. References

21. Self, M. W., van Kerkoerle, T., Goebel, R. & Roelfsema, P. R. Benchmarking Laminar fMRI: Neuronal Spiking and Synaptic Activity during Top-down and Bottom-up Processing in the Different Layers of Cortex. *NeuroImage* **197**, 806–817. issn: 1053-8119 (15th Aug. 2019).
22. Muckli, L. *et al.* Contextual Feedback to Superficial Layers of V1. *Current Biology* **25**, 2690–2695. issn: 0960-9822 (19th Oct. 2015).
23. Waehnert, M. D. *et al.* Anatomically Motivated Modeling of Cortical Laminae. *NeuroImage. In-Vivo Brodmann Mapping of the Human Brain* **93**, 210–220. issn: 1053-8119 (1st June 2014).
24. Dale, A. M., Fischl, B. & Sereno, M. I. Cortical Surface-Based Analysis: I. Segmentation and Surface Reconstruction. *NeuroImage* **9**, 179–194. issn: 1053-8119 (1st Feb. 1999).
25. Piskunowicz, M. *et al.* A New Technique with High Reproducibility to Estimate Renal Oxygenation Using BOLD-MRI in Chronic Kidney Disease. *Magnetic Resonance Imaging* **33**, 253–261. issn: 0780-725X (1st Apr. 2015).
26. Milani, B. *et al.* Reduction of Cortical Oxygenation in Chronic Kidney Disease: Evidence Obtained with a New Analysis Method of Blood Oxygenation Level-Dependent Magnetic Resonance Imaging. *Nephrology Dialysis Transplantation* **32**, 2097–2105. issn: 0981-0509 (1st Dec. 2017).
27. Dawe, R. J., Bennett, D. A., Schneider, J. A., Vasireddi, S. K. & Arfanakis, K. Post-mortem MRI of Human Brain Hemispheres: T2 Relaxation Times during Formaldehyde Fixation. *Magnetic Resonance in Medicine* **61**, 810–818. issn: 1522-2594.
28. Van der Kolk, A. G. *et al.* Imaging the Intracranial Atherosclerotic Vessel Wall Using 7T MRI: Initial Comparison with Histopathology. *American Journal of Neuroradiology*. issn: 0195-6108, 1936-959X. pmid: 25477359 (4th Dec. 2014).

Chapter 6

Conclusion

Science happened